Electron-Electron and Electron-Phonon Interactions in Strongly Correlated Systems

By

CHUNHAN FENG

DISSERTATION

Submitted in partial satisfaction of the requirements for the degree of

DOCTOR OF PHILOSOPHY

in

Physics

in the

OFFICE OF GRADUATE STUDIES

of the

UNIVERSITY OF CALIFORNIA

DAVIS

Approved:

Richard Scalettar, Chair

Rajiv Singh

Gergely Zimanyi

Committee in Charge

2022

To My Family

Contents

List of Figures vi

Abstract xv

Acknowledgements xvi

Chapter 1. Introduction 1

Chapter 2. Models describe electron-electron and electron-phonon interactions 6

2.1. The Hubbard Model 7

2.2. The Holstein Model 12

2.3. The Su-Schrieffer-Heeger Model 17

2.4. Summary 18

Chapter 3. A Review of Mean Field Theory and Quantum Monte Carlo Algorithms . 19

3.1. Mean Field Theory 20

3.2. Markov chain Monte Carlo 23

3.3. Classical Monte Carlo 26

3.3.1. The master equation 26

3.3.2. Detailed Balance Algorithms 27

3.4. Determinant Quantum Monte Carlo 28

3.4.1. DQMC for the Hubbard model: Hubbard-Stratonovich Transformation 29

3.4.2. DQMC for the Holstein model: Feynman path integral 35

3.5. Langevin Quantum Monte Carlo 37

Chapter 4. Charge density waves on a half-filled decorated honeycomb lattice 39

4.1. Introduction 39
4.2. Model and Methods 41
4.3. Mean Field Theory Results 45
4.4. Quantum Monte Carlo Results 48

Chapter 5. Interplay of flat electronic bands with Holstein phonons 55
5.1. Introduction 55
5.2. Holstein Model 56
5.3. Computational Methodologies 58
5.4. Results 61
5.4.1. Mean Field Theory 61
5.4.2. Determinant Quantum Monte Carlo 65

Chapter 6. Phase Diagram of the Su-Schrieffer-Heeger-Hubbard model on a square lattice 72
6.1. Introduction 72
6.2. Model and Method 74
6.3. Results 76
6.3.1. Main Results 76
6.3.2. An approximate treatment of the SSHH model in terms of a pure Hubbard Hamiltonian with a renormalized U_{eff} 81
6.3.3. Bond ordered wave structure factor 83
6.3.4. Antiferromagnetic structure factor 85
6.3.5. Structure factors at several different temperatures 88

Chapter 7. Charge Singlets and Orbital Selective Charge Density Wave Transitions . 90
7.1. Introduction 90
7.2. Layered Holstein Hamiltonian 91

7.3. Langevin QMC Algorithm 94
7.4. Holstein bilayer 97
7.5. Results 101
7.5.1. Holstein-Metal interface 101
7.5.2. Spectral Functions and Double Occupancies 103
7.5.3. Connection to Magnetic Language 106
7.5.4. Extracting the critical exponents 108
7.5.5. Induced CDW in Ionic Hubbard Model 109
Chapter 8. Conclusions 112
Bibliography 117

List of Figures

2.1 Exact diagonalization results for the ground state charge, $\langle S_1^z S_2^z \rangle$, and superconducting, $\langle S_1^x S_2^x \rangle$, correlators (in magnetic language) on a two site Holstein dimer, as a function of ω_0 at fixed $U_{\text{eff}} = -2.89$. The vertical line at $\omega_0 = 1$ shows the phonon frequency used in the phase diagram of Chapter 4 of this thesis. The dashed horizontal line is the Hubbard model result at $U = 2.89$. It is notable that values $\omega_0/t \lesssim 1$ are quite far from the limit where the spin correlations (CDW-pairing correlations) are symmetric. 16

3.1 The Lieb lattice geometry. Additional sites (blue and green) are added to midpoint of each of the bonds linking the sites of a square lattice (red). The resulting structure is bipartite and has three sites per unit cell. 21

4.1 The structure of the 'decorated honeycomb lattice'. Two different hopping strengths are present. Hybridization t (thin black lines) links the sites of a collection of independent hexagons. These hexagons are then connected by t' (thick blue lines). In the $t' >> t$ limit, an alternate description in terms of elemental dimers linked by t is a more appropriate starting point. 41

4.2 Left: Energy dispersion $E(\vec{k})$ in the noninteracting ($\lambda = 0$) limit. The Dirac points of the two bands of the honeycomb lattice, $t = t'$ (middle panel), are split by the decoration $t \neq t'$. In both cases, $t > t'$ and $t < t'$, a gap is opened at half-filling. See text for a discussion of differences at other fillings. Right: Density of states for the same three cases as left panel. A gap at half-filling is evident when $t \neq t'$. 44

4.3 Top: Dependence of T_c on λ_D of the decorated Holstein model Eq. 6.1 within mean field theory. The CDW transition temperature is maximized for isotropic hopping ($\Delta = 0$), and is suppressed on the dimer side $\Delta < 0$ and the hexagon side ($\Delta > 0$). Bottom: Comparison of T_c given by MFT and classical Monte Carlo for a classical lattice gas. The difference between exact T_c and MFT T_c is more significant when Δ approaches to the limiting cases $\Delta = -1$ and $\Delta = 0.5$. 47

4.4 Charge structure factor S_{cdw} as a function of hopping difference Δ. There is a window near the isotropic point $\Delta = 0$ in which S_{cdw} is large and scales with system size, indicating long range charge order. 49

4.5 Difference $\mathcal{D}$ between density correlation function on t and t' bonds as a function of Δ. $\mathcal{D}$ rises steeply in the vicinity of the CDW to charge singlet QCP. 50

4.6 Scaled structure factor $S_{\text{cdw}}/L^{\gamma/\nu}$ as a function of β. The scaling exponent $\gamma/\nu = 7/4$ is taken to be the 2D Ising value, and provides a good universal crossing. The crossing points identify $T_c = 1/\beta_c$. 51

4.7 Top: Phase diagram of T_c as a function of Δ when $\lambda_D = 0.48$. T_c reaches its maximum for isotropic hopping ($\Delta = 0$), and drops sharply on the dimer side $\Delta < 0$ and the hexagon side ($\Delta > 0$). Bottom: Phase diagram of T_c as a function of λ_D when $t = 0.9, t' = 1.2$ with $(\lambda_D)_c \sim 0.32$. As λ_D grows, T_c increases first, as the electron-phonon coupling induces the CDW phase, but then decreases as large values of the electron-phonon coupling cause the polarons to become increasingly heavy [**1**, **2**]. The symbol along the horizontal axis of panel (b) is obtained by extrapolating the sharp descent of the DQMC data for T_c, combined with low temperature simulations which show the charge correlations are short ranged. 52

4.8 Spectral function for the two cases $\Delta = -0.6$ in the charge liquid phase and $\Delta = -0.2$ in the CDW phase. 54

5.1 The Lieb lattice geometry. Additional sites (blue and green) are added to midpoint of each of the bonds linking the sites of a square lattice (red). The resulting structure is bipartite and has three sites per unit cell. Note especially that the red sublattice contains only half as many sites as the sublattice comprised of blue and green sites. The $\pm$ pattern on on the four blue/green sites surrounding one of the vacancies illustrates a zero energy mode. See text. 57

5.2 The density of states of the Lieb lattice. Energy levels of two dispersing bands bracket the δ-function peak at $E = 0$. Particle-hole symmetry is reflected in the property that $N(E) = N(-E)$. 59

5.3 The band structure of the Lieb lattice. 60

5.4 Mean field order parameter Δ^* as a function of temperature T/t at half-filling, $\mu = -\frac{\lambda^2}{\omega_0^2} = -4$. For $T > T_c \sim 1.9\,t$, the MFT critical temperature, $\Delta^* = 0$ and each site has $\rho_{\mathbf{i}} = 1/2$. For $T < T_c$ there are two degenerate values of $\Delta = \pm\Delta^*$ which minimize $\mathcal{F}$. These correspond to $1/2 - d\rho$ and $1/2 + d\rho$ (and hence the *average* density is half-filled), with $d\rho$ gradually growing to $1/6$ as T decreases (corresponding to $1/3$ and $2/3$ filling). 62

5.5 Density ρ as a function of chemical potential μ within MFT. Temperature $T = 2\,t > T_c$ and $\rho(\mu)$ is smooth. For temperature $T = t < T_c$ the density $\rho(\mu)$ has plateaus at $\rho = 1/3, 2/3$ corresponding the a non-zero CDW gap. The sublatttice occupations are given by $\rho_A = 1/2 + \Delta^*$ and $\rho_{B/C} = 1/2 - \Delta^*$ so that when $\Delta^* > 0$ there is a smaller number of A sites with $\rho > 1/2$ and a larger number of B/C sites with $\rho < 1/2$ and the total density $\rho = 1/3$, and vice-versa for $\Delta^* > 0$. 63

5.6 The spectral function $A(\omega)$ determined in DQMC calculations. A gap opens at the Fermi surface $\omega = 0$ as the temperature is lowered (β increases). This provides a rough estimate of T_c. 64

5.7 Left: The scaled structure factor is plotted versus β for three lattice sizes. The crossing gives the position of the CDW transition. Right: If the horizontal (inverse temperature) axis is also scaled, a full data collapse is obtained. 66

5.8 Density-density correlation for a $3 \times (4 \times 4)$ Lieb lattice at $\omega_0 = 1, \lambda = 2(\lambda_D = \sqrt{2}/2)$. The simulation was initialized with HS field appropriate to being in the $\rho = 1/3$ minimum with dominant A sublattice ('Copper sites') occupation. First row: correlations between each site and the Cu site in the bottom left unit cell. Second row: correlations between each site and the B/C sublattice ('Oxygen sites') in the bottom left unit cell. 67

5.9 Same as Fig. 5.8 except starting in the $\rho = 2/3$ minimum. 67

5.10 Density ρ as a function of β at the $\lambda_D = \sqrt{2}/2$. Data for four different random seeds are shown. A spontaneous symmetry breaking begins to occur at $\beta \sim 5$. See text for details. The vertical dashed line is the value of β_c detemined from FSS of S_{cdw}. 68

5.11 Density ρ vs. chemical potential μ for several different β obtained in DQMC simulations. Here $\lambda = 2, (\lambda_D = \sqrt{2}/2)$. 69

5.12 Double occupancy $\mathcal{D}$ vs β at $\lambda = 2(\lambda_D = \sqrt{2}/2)$ for a $3 \times (4 \times 4)$ lattice and $\mu = -\lambda^2/\omega_0^2$. Data for four different random seeds are shown. The vertical dashed line is the value of β_c detemined from FSS of S_{cdw}. 70

5.13 Critical temperatures for the Lieb lattice (this work) and the honeycomb [**1**] and square lattices. 71

6.1 Phase diagram of the SSHH model at half-filling. g is the dimensionless electron-phonon coupling constant, and U/t is the Coulomb repulsion strength. A dotted (green) line shows the location of a crossover in the nature of the AF. $\beta = 16$ ensures the system is close to the ground state for all three lattice sizes. The AF-BOW transitions for $L = 10, 12$ coincide, indicating negligible finite size effects. The insets show schematically the AF and BOW phases. 75

6.2 DQMC results of the AF (BOW) structure factor S_{AF} ($S_{K_x}(\pi, \pi)$) for horizontal (left) and vertical (right) cuts in the phase diagram. In the AF phase, S_{AF} is finite and $S_{K_x}(\pi, \pi)$ is negligible. In the BOW phase, S_{AF} is negligible and $S_{K_x}(\pi, \pi)$ is finite. 77

6.3 DQMC results of average kinetic energy, $\langle K_{x(y)} \rangle$, and average phonon displacement, $\langle X_{x(y)} \rangle$, in x and y directions for horizontal (left) and vertical (right) cuts in the phase diagram. 79

6.4 (a) Average kinetic energy. (b) double occupancy for different U and fixed lattice size $L = 12$; (c) derivative of the kinetic energy with respect to g. The legends in panels (a,b) explain the symbols in panels (a,b,c). (d) pairing structure factors at fixed $U = 4$ and $L = 10$. 80

6.5 Inset in panel (a): In SSHH model, when $U = 4, \beta = 16$ on a $L \times L = 10 \times 10$ square lattice, for each g, we define U_{eff} as the onsite electron repulsion in the pure Hubbard model which gives the same double occupancy D. (a) AF structure factor (b) Electron Kinetic energy given in SSHH model (red curve), for $U = 4$, varying g, $\beta = 16$ on a $L \times L = 10 \times 10$ square lattice and in pure Hubbard model(blue dot) when $\beta = 16$ on a $L \times L = 10 \times 10$ with U_{eff} defined in Fig. 6.5 (a) inset. Two curves are in reasonable agreement at relatively small g, while the discrepancy at large g is because BOW phase can not be captured by the pure Hubbard model. 83

6.6 Bond ordered wave structure factor, $S_{K_x}(k_x, k_y)$ as a function of momentum k_x, k_y for $U = 4$, $g = 1.5$, $\beta = 16$, $L = 12$. 84

6.7 Finite size scaling of the antiferromagnetic structure factor, S_{AF}/L^2, for $g = 0,\ 0.2,\ 0.4,\ 0.6,\ 0.8$. The dotted lines are extrapolated from the simulations data. For all results shown in this panel, $U = 4,\ \beta = 16$. 85

6.8 Spin-spin correlation, $\langle S_i^x S_j^x \rangle$ versus spatial distance $|i - j|$ for various g. 86

6.9 Spin-spin correlation, $\langle S_i^x S_j^x \rangle$ versus spatial distance $|i - j|$ for several phonon frequencies, ω_0, for the pure SSH model on an 8×8 square lattice. Increasing ω_0 at fixed g^2/ω_0 enhances AF order. 87

6.10 Left panels: AF and BOW structure factors vs. electron-phonon coupling g for a fixed $U = 4$, at several different temperatures $\beta = 4, 8, 12, 16, 20$. Right panels: AF and BOW structure factors vs. onsite Coulomb interaction U for a fixed $g = 1.0$, $\beta = 16, 20$ on 8×8 and 12×12 lattices. Both panels indicate $\beta = 16$ is low enough to capture the ground state physics for the SSHH model. 88

7.1 (a) Sketch of a bilayer with relevant terms in Eq. (7.1) marked. (b) Phase diagram of the Holstein bilayer giving the CDW transition temperature T_c as a function of inter-layer hopping t_3. Two values of electron-phonon coupling, $\lambda = 0.2$ and $\lambda = 0.16$, are shown. Dashed lines are guides to the eye. Inset shows crossing plot of $S^{\rm cdw}/L^{7/4}$ versus t_3 at $\lambda = 0.2$ and low temperature $\beta = 20$. (c) Analog of (b), but for the Holstein-metal interface. Two crossings at $t_3 \sim 1.3$ and $t_3 \sim 3.2$ are revealed in the inset for layer $l = -1$. The CDW phase in this layer is present only in the region between the two crossings. QCPs are marked by stars on x-axis in both panel (b) and (c). Phonon frequency is set at $\omega = 0.1$ for all data. 95

7.2 (a) Charge structure factor $S^{\rm cdw}$; and (b) $p_{-1,1}$ and $d_{-1,1}$ as a function of interlayer hopping t_3 for the Holstein bilayer at low temperature $\beta = 16$ and $\lambda_{+1} = \lambda_{-1} = 0.2$. $S^{\rm cdw}$ shows significant finite size effects in the ordered phase $t_3 \lesssim 4.8$. Note that $d_{-1,1}$ vanishes at $t_3 = 0$, but jumps discontinuously to a non-zero value for infinitesmal t_3. Panels (c,d) are analog of (a,b) for the Holstein-metal interface. The two curves in (c) correspond to layers $l = +1$ and $l = -1$, with $\lambda_{+1} = 0.2$ and $\lambda_{-1} = 0$ respectively and temperature $\beta = 20$. In all plots the phonon frequency is set at $\omega = 0.1$. 98

7.3 (a) CDW structure factor $S^{\rm cdw}$ dependence on the inverse temperature β and finite size scaling of the Holstein bilayer at $t_3 = 2$. Both the crossing plot (b), and the full data collapse (c) using 2D Ising critical exponents and $\beta_c \simeq 3.0$. 100

7.4 (a) CDW structure factor, S^{cdw}, dependence on the inverse temperature, β, for layer $l = 1$ of the Holstein interface at $t_3 = 1$; (b) using 2D Ising critical exponents for finite size scaling (FSS). Panels (c) and (d) display the same but for the metallic layer $l = -1$. Panels (e–h) display the corresponding data for $t_3 = 2$. FSS in (f) and (h) show the same critical temperature for both layers at $t_3 = 2$, in contrast to $t_3 = 1$, where layer $l = +1$ (b) exhibits a clear CDW transition whereas data for layer $l = -1$ (d) does not exhibit crossing when using Ising critical exponents. 102

7.5 Full data collapse of the scaled CDW order parameter versus scaled reduced temperature in the 'Holstein interface' system. Only the Holstein layer (layer 1) shows a single universal curve for $t_3 = 1$ (a), while both collapse for $t_3 = 2t$ (panels b,d). 103

7.6 Spectral function $A(\omega)$ at $\beta = 12$ for several t_3 values cutting across the Holstein-metal interface phase diagram of Fig. 7.1. Top: Small t_3. Middle: Intermediate t_3. Bottom: Large t_3. Left and right columns correspond to Holstein and metallic layers $l = +1$ and $l = -1$ respectively. 105

7.7 Double occupancy D shown as a function of interlayer hopping t_3 at low temperature $\beta = 20$. D is a local observable, and its value is the same for $L = 8$ and $L = 12$ to within the symbol size; we show the latter. (a) Holstein bilayer; (b) Holstein-metal interface. In (a) the two layers are equivalent and a single curve is shown. In (b) the green curve shows data on layer $l = -1$, whereas the grey curve represents layer $l = +1$. 106

7.8 Contour plot of the sum of squared residuals of the least-squares fit $S(\nu, \gamma)$ of the scaled data for the CDW structure factor S^{cdw} of the Holstein bilayer at $t_3 = 2$ (see Fig. 7.3 for the original data). A 16-th order polynomial is used to fit the dataset, and the critical inverse temperature used is $\beta_c = 3.02$. The white marker denotes the minimum $S(\nu, \gamma)$ in the displayed range of ν and γ. 108

7.9 Solution of the tight binding Hamiltonian, Eq. 7.19. (a) Solid curves Occupations ρ on the $+\delta$ sites of the insulating band as functions of the magnitude of the staggered potential δ; dashed curves: Occupations on the partner sites in the metallic band to which those $+\delta$ sites are hybridized by t_3. (b) Solid Curve: Occupations on the $+\delta$ sites of the insulating band as a function of interlayer hybridization t_3. Dashed curves: Occupations on the partner sites in the metallic band to which those $+\delta$ sites are hybridized by t_3. The staggered potential in this case is $\delta = 1.25$. In both panels the linear lattice size and the inverse temperature are $L = 12$ and $\beta = 4$, respectively.... 110

Abstract

Electron-electron and electron-phonon interactions in strongly correlated systems have attracted considerable attention over the last several decades. The Hubbard, Holstein and Su-Schrieffer-Heeger(SSH) models are iconic models to capture the physics of these interactions and explore their rich and interesting phases caused by them, i.e. Ferromagnetism (FM), Anti-ferromagnetism (AF), Charge Density Wave (CDW), Bond Ordered Wave (BOW), Superconductivity(SC) and other exotic phases. Chapter 1 gives an introduction to the physics related to electron-electron and electron-phonon interactions. Then the paradigmatic models, the Hubbard, Holstein and SSH which describe these interactions are introduced in Chapter 2. Some basic properties of these models are discussed as well. Then we review the methods we use, Mean Field Theory (MFT), Determinant and Langevin quantum Monte Carlo (QMC) to study these systems in Chapter 3. Chapter 4 and Chapter 7 consider the effect of non-uniform hopping on a honeycomb lattice and a layered square lattice on Holstein electron-phonon couplings. In Chapter 5, we investigate the interplay of the flat band of a Lieb lattice and Holstein phonons. Chapter 6 considers both electron-electron and electron-phonon interactions and explores the competition between them and possible intermediate exotic phases. Finally Chapter 8 gives a summary and proposes some possible directions for future research.

Acknowledgements

As I am close to finishing my PhD thesis, I would like to extend my thanks to my family, all my teachers and friends for their love, care and cultivation, which makes me have the courage and confidence to overcome difficulties, accomplish my goals and go further along the road of pursuing science.

First of all, I would like to express my huge sincere gratitude to my excellent advisor Prof. Richard Scalettar. It is my great pleasure to have him as my advisor since my first year PhD. I have been impressed by his extreme hard working, rigorous scientific attitude and great enthusiasm in physics and this also inspires me to become the best I can be. His encouragement and patience make me feel very comfortable to put forward any ideas and questions I have and I always benefit a lot from intensive discussions with him. I also appreciate Richard's encouragement and support for me to attend lots of international meetings and participate in summer schools, where I have opportunities to communicate with outstanding scientists and broaden my horizons. Richard is more like a parent with wisdom of us in daily life, sharing his experiences, listening to our stories, providing useful suggestions, celebrating every achievement we have made and making us feel cared for and loved. I feel very fortunate to become a member of his group. His nice personality and attitudes towards science, research and life would have a profound and huge impact on my future career and life.

I am also grateful to Prof. Rajiv Singh, who has co-advised me since my first year. He always has some smart ideas and insightful suggestions. I benefit a lot from the discussions with him on the blackboard. Rajiv encouraged me to take my Qualifying Exam at an early stage, the end of my second year PhD. This wise suggestion liberates me from the pressure of examinations earlier and makes me have more time to focus on and enjoy my research in the last three years. His lectures are always clear and well organised. It's my first time to

have a clearer understanding and develop a stronger interest in Condensed Matter Theory in his Statistical Mechanics course I took in my first year PhD. It's also my great pleasure to be TA for his Quantum Mechanics course Phy 215C for graduate students for three years. I can always absorb some new knowledge from his lectures every time I attend it. I also appreciate his trust and giving me opportunities to cover advanced materials for junior graduate students. It makes me feel more confident about and get ready for teaching in my future career. He supported me to attend academic meetings and summer schools as well and I really appreciate it.

My sincere thanks also goes to Prof. Liang Jin, my research advisor in my undergraduate school, Nankai University. He is the first person who brought me into the world of scientific research and taught me patiently when I was at a beginner's level. I benefit a lot from the discussions with him and his insightful comments & suggestions about my graduate studies.

I would also like to thank Prof. Ching-Yao Fong, who is the instructor for four graduate courses I took at UC Davis. He taught & helped me a lot and patiently answered lots of my questions during the beginning of my PhD journey. I would also like to thank all the professors at UC Davis I learn from and have discussions with, Profs. Gergely T Zimanyi, Warren E. Pickett, Dong Yu, Valentin Taufour, Daniel L Cox, Shirley Chiang, Lloyd E Knox, Rena J Zieve, Daniel A Cebra, John B Rundle, Sergey Y Savrasov, and so on.

Besides, I would also like to thank all my collaborators, Profs. George Batrouni, Huaiming Guo, Rubem Mondaini, Kaden Hazzard, Ettore Vitali, Shiwei Zhang, who gave me lots of insightful suggestions and comments, provided me computer resources to complete the simulations presented in this thesis and invited me to give talks. I am also grateful to Dr. Miles Stoudenmire and Dr. Alexander Wietek, who were my advisors and guided me to conduct research during my summer 2020 internship at Center for Computational Quantum Physics (CCQ), Flatiron Institute.

Plus, I would like to thank all my classmates, friends I met at UC Davis and everyone in Richard's and Rajiv's group, Yuxi Zhang, Bo Xiao, Weiting Chiu, Benjamin Cohen-Stead, Owen Bradley, Yutan Zhang, Maxwell Casebolt, Tyler Cary, Aleksander Zujev and appreciate the time I spent with them, taking courses, doing homework and discussing problems. They indeed make my PhD life more colorful and enjoyable.

Furthermore, I am also grateful to all my mathematics and physics teachers in my middle schools, Mr. Guanming Yang, Ms. Qiuzhao Liu, Mr. Guangmin Zhang, Ms. Lin Wang et al. and professors in my undergraduate university. They showed me the beauty of science and made me develop a strong interest in exploring math and physics and choose them as my future career.

Last but not least, I would like to express my special thanks to my parents, uncles, aunts and cousins for their love, care, and company, especially to my mom, who visited me from China many times and spent lots of good times with me during my PhD journey.

CHAPTER 1

Introduction

Electron-electron and electron-phonon interactions play important roles in understanding the complex phases of many materials. The Hubbard (on-site Coulomb interaction U), Holstein (phonon displacements coupled to electron density operators), and Su-Schrieffer-Heeger(SSH) (electron hopping terms modulated by lattice distortions) models are commonly used to study these interactions and resultant phenomena. Metallic, (anti)ferromagnetic, superconducting and inhomogeneous spin & charge orders have been observed in the Hubbard model [**3**] depending on the doping and onsite Coulomb interaction strength [**4**, **5**]. The Holstein model has been widely explored to study conventional s-wave SC transitions [**6**, **7**], polaron physics and charge density wave (CDW) on various geometries [**1**, **2**, **8**–**16**], while the SSH interaction gives rise to the bond-ordered wave (BOW) pattern on a square lattice when the electron-phonon coupling is larger than the critical value $g > g_c$, antiferromagnetic (AF) order when $g < g_c$, and interesting topological effects. The SSH model is appropriate to describe systems like conjugate polymers [**17**], organic charge transfer salts [**18**], metal salts [**19**] and $CuGeO_3$ [**20**]. It would be interesting to explore the thermal phase transitions, whether there exists a critical coupling strength (quantum critical point) to support the corresponding phases on different geometries, and the effects of non-uniform hopping/different types of energy band (in the non-interacting limit) on these orders.

In this thesis, we will introduce the models, Hubbard, Holstein and SSH in Chapter 2. Mean Field Theory (MFT), Determinant and Langevin quantum Monte Carlo methods we use to explore these strongly correlated systems are discussed in Chapter 3.

After this foundation, Chapters 4-7 contain materials from four published or submitted manuscripts: " Charge density waves on a half-filled decorated honeycomb lattice", by Chunhan Feng, Huaiming Guo and Richard T. Scalettar, Phys. Rev. B 101 (20), 205103 (2020) [**10**]; "Interplay of flat electronic bands with Holstein phonons", by Chunhan Feng and Richard T. Scalettar, Phys. Rev. B 102 (23), 235152 (2020) [**13**]; "Phase diagram of the Su-Schrieffer-Heeger-Hubbard model on a square lattice", by Chunhan Feng, Bo Xing, Dario Poletti, Richard T. Scalettar and George Batrouni, arXiv:2109.09206 [cond-mat.str-el] [**21**]; and "Charge Singlets and Orbital Selective Charge Density Wave Transitions", by Yuxi Zhang, Chunhan Feng, Rubem Mondaini, George Batrouni and Richard T. Scalettar, arXiv:2109.13482 [cond-mat.str-el] [**22**]. I now summarize those chapters briefly. They are connected by a common computational theme: quantum Monte Carlo, and also by the general idea of exploring long range order induced by electron-phonon interactions.

In Chapter 4, we study the Holstein model on a decorated honeycomb lattice to explore the effects of non-uniform hopping on Holstein phonons. People have spent much effort to investigate itinerant electrons on a honeycomb lattice, which hosts a Dirac spectrum in the non-interacting limit [**23**–**28**]. However, this past work has mostly focussed on electron-electron interactions (onsite Hubbard U). The non-interacting density of states (DOE) vanishes linearly at $E = 0$, while on a square lattice, the DOS diverges logarithmically at $E = 0$ instead. As a consequence, a nonzero critical U_c is required to support AF order on the honeycomb lattice [**29**, **30**], whereas in a square lattice long range antiferromagnetic (AF) correlations onset in the ground state for any finite repulsive interaction U.

Recently, the effects of electron-phonon interactions on Dirac fermions have been explored [**1**,**2**]. The more complex situation of non-uniform t has been studied within a number of situations, perhaps most prominently in multi-band geometries where there is a natural distinction of hopping between orbitals of different degree of overlap. In this chapter, we

extend these investigations of the Holstein model on a 'decorated honeycomb lattice', consisting of hexagons with internal hopping t coupled together by t'. This modulation of the hopping introduces a gap in the Dirac spectrum and affects the nature of the topological phases. We determine the range of t/t' values which support a charge density wave (CDW) phase about the Dirac point of uniform hopping $t = t'$, as well as the critical transition temperature T_c.

Chapter 5 discusses the effects of a flat band on electron-phonon interactions. A number of periodic tight-binding lattices, e.g. Kagomé, Creutz, decorated honeycomb, and the dice lattice, contain such a macroscopic degeneracy of local, zero energy eigenstates [**31**, **32**]. One of the most prominent examples is the Lieb lattice, which is of special interest as the structure of the CuO_2 planes of the cuprate superconductors.

Existing Quantum Monte Carlo studies have investigated the properties of fermions on a Lieb (CuO_2) lattice interacting with an on-site, or near-neighbor electron-electron coupling. Attention has focused on the interplay of such interactions with the macroscopic degeneracy of local zero energy modes, from which Bloch states can be formed to produce a flat band in which energy is independent of momentum. The resulting high density of states, in combination with the Stoner criterion, suggests that there should be pronounced instabilities to ordered phases. Indeed, a theorem by Lieb [**33**] rigorously establishes the existence of ferrimagnetic order. Subsequent work further investigated flat band ferromagnetism [**34**–**37**].

Here, we again extend this past work to the new area of electron-phonon interactions, i.e. we investigate in Chapter 5 the phases of interacting electron-phonon systems for flat electronic bands [**38**]. Specifically, we study the Holstein Hamiltonian on a Lieb lattice and find a 1/3 filling charge density wave (CDW) pattern and its partner under Particle-Hole Transformation (PHT), at 2/3 filling, are generated spontaneously below a finite temperature.

Furthermore, Chapter 6 presents our recent work on the Su-Schrieffer-Heeger-Hubbard (SSHH) Hamiltonian on a square lattice, which examines the competition between electron-electron and electron-phonon interactions. For a half-filled Holstein model on a 2D square lattice, CDW patterns exist for any finite values of electron-phonon coupling λ [**39**]. When an extra on-site Coulomb repulsion U term is included, CDW or AF order will dominate in the system depending on the relative magnitude of U and λ [**40**, **41**]. Interestingly, an intermediate metallic phase between the AF and CDW phases is indicated [**42**–**45**], as well as other exotic regimes [**46**].

For the 2D square lattice SSH model at half-filling, there is an AF phase when the electron-phonon coupling λ is less than a critical value λ_c and a bond order wave when $\lambda > \lambda_c$ [**47**–**49**]. We study here the rich interplay of BOW and AF regimes in the SSHH model. A phase diagram is obtained. Besides the Antiferromagnetic (AF) phase (in the Hubbard limit) and Bond-ordered-wave (BOW) phase (in the SSH limit), there is also an intermediate region maintaining long range AF order, which exhibits larger electron kinetic energies and double occupancies, i.e. larger quantum fluctuations, similar to the AF phase found in the pure SSH model.

Over the last several decades, much attention has been attracted to layered materials including the cuprate superconductors (SC) [**50**–**54**] and bilayer graphene [**55**–**60**]. A theoretical motivation is that bilayer materials offer a possibility to explore the competition between the formation of long range order at weak interlayer coupling and collections of independent local degrees of freedom in the limit of strong interlayer coupling.

The possibility of 'orbitally selective Mott transitions' (OSMT) [**61**–**72**] within a multi-band Hubbard model, in which one orbital with large on-site electron-electron repulsion U_1 is insulating and another orbital, to which it is hybridized, with small U_{-1}, is metallic, is a problem of long-standing debate and investigation. In Chapter 7 we study an analogous

problem, the co-existence of metallic and insulating bands in a system of orbitals with different electron-phonon coupling and investigate the effects of interband hybridization t_3.

Finally, Chapter 8 summarizes the conclusions, reviews connections, and proposes open questions, further discussions and possible new directions in the future.

CHAPTER 2

Models describe electron-electron and electron-phonon interactions

Electron-electron and electron-phonon interactions play important roles in understanding the rich and diverse phases of strongly correlated systems. The Hubbard Hamiltonian is a paradigmatic model people widely use to study the electron-electron case, via inclusion of an onsite Coulomb interaction. It was first proposed in the 1960's to investigate the ferromagnetism of transition metals [**3**, **73**, **74**]. Later, it was found to exhibit metallic, ferromagnetic (FM), antiferromagnetic (AF) and superconducting (SC) orders, as well as intricate inhomogeneous spin and charge patterns, depending on U and the doping [**4**, **5**].

On the other hand, the Holstein [**75**] and the Su-Schrieffer-Heeger (SSH) [**76**] models are commonly studied to explore electron-phonon interactions. The main difference between these two models is that in the former, the phonon displacement is coupled to the electron density, while for the latter, phonons live on the bonds and the electron hopping is modulated. Polarons and charge-density wave (CDW) physics on different geometries [**1**,**2**,**8**–**16**,**77**], and conventional s-wave SC transitions [**6**,**7**] have been explored in the Holstein model. The SSH model can be used to capture the physics of conjugated polymers [**17**], organic charge transfer salts [**18**], metal salts [**19**] and $CuGeO_3$.

In this chapter, we will introduce the Hubbard, Holstein and Su-Schrieffer-Heeger models and illustrate what simplifications we need to make to extract these second quantization Hamiltonians from real materials with complicated electron-electron and electron-phonon interactions. We will also discuss the important properties of the models, e.g. the Particle-Hole symmetry, and the equivalence of the Holstein model in the anti-adiabatic limit to the

Hubbard model with attractive interactions, which shed light on the results we will present in the later chapters.

2.1. The Hubbard Model

In the past decades, condensed matter theorists spent much effort to study the Hubbard model, which captures the basic electron-electron repulsion in many-body problems, using various analytical and numerical methods, including exact diagonalization (ED), static and dynamical mean field theory (DMFT) and quantum Monte Carlo (QMC), etc. In this section we will give an introduction to the Hubbard model, illustrating how to get the second quantized form of the Hamiltonian, and discuss some basic concepts and interesting physics arising from it.

The Hamiltonian of a solid includes the kinetic energies of the electrons and ions, as well as the Coulomb interactions between these constituents. In general, we can use the Born-Oppenheimer approximation to separate the motion of ions and electrons since ions are much heavier than electrons. That is, the ionic coordinates $\vec{R}_\alpha$ are regarded as frozen degrees of freedom. The resulting Hamiltonian for the many-body electron problem can be written as

$$\hat{H} = \sum_i (-\frac{\hbar^2}{2m_e}\nabla_i^2) + \sum_i U_{el-ion}(\vec{r}_i) + \sum_{i\neq j} U_{el-el}(\vec{r}_i - \vec{r}_j), \tag{2.1}$$

where m_e is the mass of an electron, $\vec{r}_i$ is the position of the i^{th} electron, and $\vec{R}_\alpha$ is the position of the α^{th} ion. In this approximation the ion-ion term is a constant since it involves only $\vec{R}_\alpha$ and we can drop it from $\hat{H}$. $U_{el-ion}(\vec{r}_i)$ is the electron-ion interaction,

$$U_{el-ion}(\vec{r}_i) = -Ze^2 \sum_\alpha \left|\vec{r}_i - \vec{R}_\alpha\right|^{-1}, \tag{2.2}$$

where Z is the number of positive charges of the ion. Meanwhile

$$U_{el-el}(\vec{r}_i - \vec{r}_j) = e^2/\left|\vec{r}_i - \vec{r}_j\right| \tag{2.3}$$

describes the Coulomb repulsion between electrons. We refer to these expressions as being in "first quantized" form since they include the nontrivial quantum physics of the Schrodinger equation but do not yet use the more abstract notation of "second quantization".

Creation and destruction operators: Before we introduce second quantization for the electrons, let us review the definition of creation and annihilation operators in the Quantum Harmonic Oscillator (QHO) problem. They are expressed in terms of displacement and momentum operators,

$$\begin{aligned} \hat{a}^\dagger &= \sqrt{\frac{m\omega}{2\hbar}}\hat{x} - i\sqrt{\frac{1}{2m\omega\hbar}}\hat{p} \\ \hat{a} &= \sqrt{\frac{m\omega}{2\hbar}}\hat{x} + i\sqrt{\frac{1}{2m\omega\hbar}}\hat{p} \end{aligned} \tag{2.4}$$

The commutation relation between the creation and annihilation operators can be easily verified,

$$[\hat{a}, \hat{a}^\dagger] = 1 \tag{2.5}$$

as a direct consequence of the relation $[\hat{p}, \hat{x}] = -i\hbar$. Then the Hamiltonian for the QHO can be written in terms of $\hat{a}$ and $\hat{a}^\dagger$,

$$\begin{aligned} \hat{H} &= \frac{1}{2m}\hat{p}^2 + \frac{1}{2}m\omega^2\hat{x}^2 \\ &= \hbar\omega(\hat{a}^\dagger\hat{a} + \frac{1}{2}) \\ &= \hbar\omega(\hat{n} + \frac{1}{2}) \end{aligned} \tag{2.6}$$

in which $\hat{n} = \hat{a}^\dagger\hat{a}$ is the number operator. The creation and annihilation operators have the following properties,

$$\begin{aligned} \hat{a}|n\rangle &= \sqrt{n}|n-1\rangle \\ \hat{a}^\dagger|n\rangle &= \sqrt{n+1}|n+1\rangle \end{aligned} \tag{2.7}$$

$|0\rangle$ is used to represent the ground state of the QHO, and hence we have $\hat{a}|0\rangle = 0$ and ground energy $E_0 = \hbar\omega/2$.

We need to emphasize that the creation and annihilation operators in the QHO problem are for bosons and the number of particles can be $0, 1, 2, 3, \ldots$. It can also be easily verified that the average number of particles satisfies the Bose-Einstein distribution,

$$\langle \hat{n} \rangle = 1/(e^{\beta\hbar\omega} - 1). \tag{2.8}$$

The first quantized formulation of Eq. (2.1) requires that one separately impose an anti-symmetric condition on the electron wave function $\phi(\vec{r}_1, \vec{r}_2, \cdots, \vec{r}_N)$ to respect the fermionic character. It seems natural that a formulation which automatically includes the proper statistics might be more simple to use. This is the basic idea behind "second quantization". To employ second quantization for many-electron problems, we need to introduce *fermion* creation and annihilation operators. The main conceptual difference is that the fermion operators stand on their own instead of being related to the position and momentum operators as for the quantum oscillator. In addition, due to the Pauli principle, the number of electrons for a specified spin species on a particular site can only be 0 or 1. The fermion creation and annihilation operators anti-commute with each other and we have the following relations,

$$\{\hat{c}_{i\sigma}, \hat{c}^\dagger_{j\sigma'}\} = \delta_{i,j}\delta_{\sigma,\sigma'}, \qquad \{\hat{c}^\dagger_{i\sigma}, \hat{c}^\dagger_{j\sigma'}\} = 0, \qquad \{\hat{c}_{i\sigma}, \hat{c}_{j\sigma'}\} = 0 \tag{2.9}$$

Here i, j are site or orbital indices and σ labels the spin.

Second quantized form of the Hubbard Model: One-body operators: One can prove that a first quantized one-body operator $H^{(1)}(\vec{r})$, has a second quantized form written as

$$\begin{aligned} \hat{H}^{(1)} &= \sum_{\alpha,\beta} H^{(1)}_{\alpha\beta} \hat{c}^\dagger_\alpha \hat{c}_\beta \\ &= \sum_{\alpha,\beta} \int d\vec{r} \phi^*_\alpha(\vec{r}) H^{(1)}(\vec{r}) \phi_\beta(\vec{r}) \hat{c}^\dagger_\alpha \hat{c}_\beta \end{aligned} \tag{2.10}$$

Two-body operators: Similarly, one can also prove for a first quantized two-body operator $H^{(2)}(\vec{r},\vec{r}')$, its second quantized form can be written as

$$\begin{aligned}\hat{H}^{(2)} &= \sum_{\alpha,\beta,\gamma,\delta} H^{(2)}_{\alpha\beta\gamma\delta}\hat{c}^\dagger_\alpha\hat{c}^\dagger_\beta\hat{c}_\gamma\hat{c}_\delta \\ &= \sum_{\alpha,\beta,\gamma,\delta}\int d\vec{r}\phi^*_\alpha(\vec{r})\phi^*_\beta(\vec{r}')H^{(2)}(\vec{r},\vec{r}')\phi_\gamma(\vec{r}')\phi_\delta(\vec{r})\hat{c}^\dagger_\alpha\hat{c}^\dagger_\beta\hat{c}_\gamma\hat{c}_\delta\end{aligned} \tag{2.11}$$

After introducing the second quantization of Hamiltonians in general, we turn to the specific case of the Hubbard model. Considering the Hamiltonian in Eq. 2.1, we can view $H^{(1)}(\vec{r}_i) = -\frac{\hbar^2}{2m_e}\nabla_i^2 + U_{el-ion}(\vec{r}_i)$as the first quantized one-body operator and $H^{(2)}(\vec{r}_i,\vec{r}_j) = U_{el-el}(\vec{r}_i - \vec{r}_j)$ the two-body operator. Here we make several simplifications: 1)We assume the solid has one energy band at Fermi surface and hence each site has a single orbital (energy level); 2) only consider the onsite Coulomb repulsion; 3) since wavefunctions die off exponentially and hopping 't' is given by the overlap of wavefunctions on different sites, it makes sense to focus only on the nearest neighbour hopping. The abstract index α becomes the site i and spin σ of the electron. Then

$$\begin{aligned}\hat{H} = &-t\sum_{\langle i,j\rangle,\sigma}(\hat{c}^\dagger_{i\sigma}\hat{c}_{j\sigma} + \hat{c}^\dagger_{j\sigma}\hat{c}_{i\sigma}) + U\sum_i(\hat{n}_{i\uparrow} - 1/2)(\hat{n}_{i\downarrow} - 1/2) \\ &- \mu\sum_i(\hat{n}_{i\uparrow} + \hat{n}_{i\downarrow})\end{aligned} \tag{2.12}$$

The first term is the electron kinetic energy, describing the electron hopping process between nearest neighbour sites $\langle i,j\rangle$: An electron with spin σ is destroyed on site j and then recreated on site i. The second term delineates the onsite Coulomb repulsion. Finally, the last term is the chemical potential. μ can be tuned to control the filling.

Particle-Hole Transformation: $\mu = 0 \leftrightarrow$ half filling: Before we discuss the Particle-Hole Transformation, let us first introduce the concept of a bipartite lattice. This is a geometry in which we can divide all the sites into two sublattices A and B, such that the

nearest neighbours of a site in A are only sites in sublattice B and vice-versa. A PHT is defined as follows:

$$\hat{d}^{\dagger}_{i\sigma} = (-1)^i \hat{c}_{i\sigma} \tag{2.13}$$

and correspondingly we will also have

$$\hat{d}_{i\sigma} = (-1)^i \hat{c}^{\dagger}_{i\sigma} \tag{2.14}$$

$(-1)^i$ is defined to be $+1$ for sublattice A and -1 for sublattice B. If we apply this transformation to the density operator $\hat{n}_{i\sigma}$, we get

$$\hat{n}_{i\sigma} = \hat{c}^{\dagger}_{i\sigma}\hat{c}_{i\sigma} \rightarrow (-1)^i(-1)^i \hat{d}_{i\sigma}\hat{d}^{\dagger}_{i\sigma} = 1 - \hat{d}^{\dagger}_{i\sigma}\hat{d}_{i\sigma}. \tag{2.15}$$

The numbers of particles for spin σ on site i,$n_{i\sigma} = 0, 1$ are swapped, and this directly gives an explanation why it is called a particle-hole transformation. Now let us go back to the original Hubbard Hamiltonian and see what we will get after the PHT. First of all, let us apply it to the electron kinetic energy part,

$$\hat{c}^{\dagger}_{i\sigma}\hat{c}_{j\sigma} \rightarrow (-1)^i(-1)^j \hat{d}_{i\sigma}\hat{d}^{\dagger}_{j\sigma} = \hat{d}^{\dagger}_{i\sigma}\hat{d}_{j\sigma}. \tag{2.16}$$

Since only the nearest neighbours hopping is allowed in the Hubbard Hamiltonian Eq.(2.12), $(-1)^{i+j} = -1$ and this minus sign can be used to anticommute $\hat{d}_{i\sigma}\hat{d}^{\dagger}_{j\sigma}$ back to $\hat{d}^{\dagger}_{i\sigma}\hat{d}_{j\sigma}$. The main conclusion we can get here is that the electron kinetic energy part remains unchanged after the PHT on a bipartite lattice. Then we can move to the onsite interaction U term. As was pointed out earlier, the density operator $\hat{n}_{i\sigma}$ turns into $1 - \hat{n}_{i\sigma}$ after the PHT. As a consequence, $U(\hat{n}_{i\uparrow} - 1/2)(\hat{n}_{i\downarrow} - 1/2)$ becomes $U(1/2 - \hat{n}_{i\uparrow})(1/2 - \hat{n}_{i\downarrow})$, which is exactly the same as the original. The last term we need to consider here is the chemical potential. Here the sign of μ is changed under the PHT. To sum up, for the whole system the total density ρ changes to $2 - \rho$ and the Hamiltonian transforms to another Hamiltonian with the sign of

chemical potential μ reversed. Thus, we have the relation

$$\rho(\mu) = 2 - \rho(-\mu), \tag{2.17}$$

and it can be seen obviously when $\mu = 0$, the system is at half filling $\rho = 1$.

2.2. The Holstein Model

In the last section, we recognized the ions are much heavier than the electrons and hence assumed they are frozen at their equilibrium positions. We thus consider only the electron kinetic energy and the repulsive interactions between electrons. But in reality, lattice vibrations (phonons) exist and we will discuss the effects of phonons on the behaviors of the electrons and vice-versa by exploring the electron-phonon coupling.

The electron-phonon interaction term depends on the positions of both electron and ions and can be expressed as

$$\begin{aligned} \hat{H}_{el-ion} &= \sum_{i,\alpha} V(\vec{r}_i - \vec{R}_\alpha) \\ &\approx \sum_{i,\alpha} V(\vec{r}_i - \vec{R}_\alpha^{(0)}) - \sum_{i,\alpha} \hat{\vec{u}}_\alpha \frac{\partial V(\vec{r}_i - \vec{R}_\alpha^{(0)})}{\partial \vec{R}_\alpha}, \end{aligned} \tag{2.18}$$

where $\vec{R}_\alpha^{(0)}$ is the equilibrium position of the ion and $\vec{R}_\alpha = \vec{R}_\alpha^{(0)} + \vec{u}_\alpha$.

The first term in the above equation has already been considered in the previous section. We assume the electron-electron interaction is weak and we can approximate the Hamiltonian for electrons by

$$\hat{H}_e \approx \sum_{b,\vec{k},\sigma} E_{b,\sigma}(\vec{k}) \hat{c}^\dagger_{b,\vec{k},\sigma} \hat{c}_{b,\vec{k},\sigma} \tag{2.19}$$

where b is the band index, σ represents spin and $\vec{k}$ is the allowed momentum. We can use this $|b, \vec{k}, \sigma\rangle$ basis and figure out an expression for the second quantized form of the

electron-phonon interactions. Apply Eq.(2.10) discussed above, we get

$$\hat{H}_{el-ph} = \sum_{b,\vec{k},\sigma,b',\vec{k}',\sigma'} \int d\vec{r}\phi^*_{b,\vec{k},\sigma}(\vec{r}) \sum_{\alpha} \hat{\vec{u}}_{\alpha} \frac{-\partial V(\vec{r}_i - \vec{R}^{(0)}_{\alpha})}{\partial \vec{R}_{\alpha}} \phi_{b',\vec{k}',\sigma'}(\vec{r}) \hat{c}^{\dagger}_{b,\vec{k},\sigma} \hat{c}_{b,\vec{k},\sigma} \tag{2.20}$$

$\hat{\vec{u}}_{\alpha}$, the distortion of the lattice, will be expressed by phonon creation and annihilation operators. After some algebra and assuming only a single phonon mode interacts much more strongly with electrons, we can get a generic form for the electron-phonon coupling

$$\hat{H}_{el-ph} = \frac{1}{\sqrt{N}} \sum_{\vec{k},\vec{q},\sigma} C_{\vec{k},\vec{q}} (\hat{b}^{\dagger}_{-\vec{q}} + \hat{b}_{\vec{q}}) \hat{c}^{\dagger}_{\vec{k}+\vec{q},\sigma} \hat{c}_{\vec{k},\sigma}, \tag{2.21}$$

where $C_{\vec{k},\vec{q}}$ is a constant depending on the properties of real materials. $\hat{b}^{\dagger}_{-\vec{q}}$ and $\hat{b}_{\vec{q}}$ are just Fourier Transform of phonon creation and annihilation operators on the different spatial lattice sites.

We now consider a specific example of this procedure. The Holstein model [**75**] is the simplest model which depicts the electron-phonon coupling. It consists of a collection of electrons, described by fermionic creation and destruction operators $\hat{c}^{\dagger}_{i\sigma}, \hat{c}_{i\sigma}$ hopping between near neighbor sites on the lattice. The electron density on each site, $\hat{n}_i = \hat{n}_{i\uparrow} + \hat{n}_{i\downarrow}$ with $\hat{n}_{i\sigma} = \hat{c}^{\dagger}_{i\sigma}\hat{c}_{i\sigma}$, where i denotes lattice sites and σ is the spin index, couples linearly to the displacement $\hat{x}_i$ of a local quantum oscillator degree of freedom. The Hamiltonian is therefore,

$$\begin{aligned} \mathcal{H} = & -t \sum_{\langle i,j \rangle,\sigma} \left(\hat{c}^{\dagger}_{i\sigma} \hat{c}_{j\sigma} + \text{h.c.} \right) - \mu \sum_{i,\sigma} \hat{n}_{i\sigma} \\ & + \frac{1}{2} \sum_{i} \left(\hat{p}^2_i + \omega^2_0 \hat{x}^2_i \right) + \lambda \sum_{i,\sigma} \hat{x}_i \hat{n}_{i\sigma} \ . \end{aligned} \tag{2.22}$$

We have set the oscillator mass $M = 1$ and will also use units in which $\hbar = k_{\text{B}} = 1$ and the hopping amplitude $t = 1$ in the simulations presented in this thesis. The Holstein model is just the Fourier Transform of a special case of the general form 2.21 where $C_{\vec{k},\vec{q}}$ is a constant.

The next topic describes symmetry conditions which aid in the interpretation of the DQMC code.

Particle-Hole Symmetry: In discussing the Hubbard model, we showed the electron hopping term remains unchanged under PHT so that $\mu = 0$ is half-filling. We can follow a similar method to derive which chemical potential value corresponds to the half filling in the Holstein model. Excluding the electron kinetic energy term, the other parts in the Hamiltonian

$$-\mu \sum_{i,\sigma} \hat{n}_{i\sigma} + \frac{1}{2} \sum_{i} \left(\hat{p}_i^2 + \omega_0^2 \hat{x}_i^2 \right) + \lambda \sum_{i,\sigma} \hat{x}_i \hat{n}_{i\sigma} \tag{2.23}$$

will become

$$-\mu \sum_{i,\sigma} (1 - \hat{n}_{i\sigma}) + \frac{1}{2} \sum_{i} \left(\hat{p}_i^2 + \omega_0^2 \hat{x}_i^2 \right) + \lambda \sum_{i,\sigma} \hat{x}_i (1 - \hat{n}_{i\sigma}) \tag{2.24}$$

after PHT. We can define $\hat{y}_i = -\hat{x}_i$ and the above term is equivalent to

$$\begin{aligned} &\mu \ \textstyle\sum_{i,\sigma} \hat{n}_{i\sigma} + \frac{1}{2} \sum_i \left(\hat{p}_i^2 + \omega_0^2 \hat{y}_i^2 \right) + \lambda \sum_{i,\sigma} \hat{y}_i \hat{n}_{i\sigma} - \lambda \sum_{i,\sigma} y_i \qquad (2.25) \\ \rightarrow\ &\tfrac{1}{2} \textstyle\sum_i \hat{p}_i^2 + \frac{\omega_0^2}{2} [\sum_i (\hat{y}_i^2 - \frac{4\lambda}{\omega_0^2} \hat{y}_i + \frac{4\lambda^2}{\omega_0^4})] + \lambda \sum_{i,\sigma} (\hat{y}_i - \frac{2\lambda}{\omega_0^2}) \hat{n}_{i,\sigma} + (\mu + \frac{2\lambda^2}{\omega_0^2}) \sum_{i,\sigma} \hat{n}_{i,\sigma} \end{aligned}$$

After completing the square, we observe the QHO shifts its center after the transformation and chemical potential μ turns into $-(\mu + 2\lambda^2/\omega_0^2)$. As a consequence, we have the relation,

$$\rho(\mu) = 2 - \rho(-\mu - 2\lambda^2/\omega_0^2). \tag{2.26}$$

The conclusion is that $\mu = -\lambda^2/\omega_0^2$ corresponds to half filling $\rho = 1$ in the Holstein model. The physical picture is that the ions(phonons) can distort, lowering the energy of an electron, and so μ must shift downwards (relative to $\lambda = 0$) to keep the lattice half filled.

Holstein model in the anti-adiabatic limit: In the anti-adiabatic limit ($\omega_0 \to \infty$), the Holstein model becomes equivalent to the attractive Hubbard model with $U_{eff} = -\lambda^2/\omega_0^2$.

This can be seen via the Lang-Firsov Transformation [**78**]. However, it is important to emphasize that the Holstein model breaks the superconducting-charge symmetry present in the attractive Hubbard model (the analogy of spin symmetry in the repulsive case), with charge order (the analog of ordering in the S^z channel) dominating over superconducting order (which maps onto S^x, S^y). As a result, the CDW transition in the half-filled 2D Holstein model occurs at finite temperature [**77**], whereas long range magnetic order in the 2D repulsive Hubbard model occurs only at $T = 0$. This breaking of symmetry introduces a fundamental difference between the physics of the repulsive Hubbard and Holstein models with multiple hopping energy scales, which is especially marked as the phonon frequency ω_0 decreases.

In particular, consider the well-known "partial" particle-hole transformation (PHT) $c^\dagger_{i\downarrow} \rightarrow (-1)^i c_{i\downarrow}$ acting only on the down spin fermions. On a bipartite lattice, and at $\mu = 0$, this PHT leaves the kinetic energy unchanged as with the full PHT of Eq.(2.13)(2.14), but now reverses the sign of the interaction term. The different components of the spin operator map into charge and pairing correlations,

$$\begin{aligned} S^z_i \equiv n_{i\uparrow} - n_{i\downarrow} \;&\rightarrow\; n_i \equiv n_{i\uparrow} + n_{i\downarrow} \\ S^+_i \equiv c^\dagger_{i\uparrow} c_{i\downarrow} \;&\rightarrow\; \Delta^\dagger_i \equiv (-1)^i \, c^\dagger_{i\uparrow} c^\dagger_{i\downarrow} \\ S^-_i \equiv c^\dagger_{i\downarrow} c_{i\uparrow} \;&\rightarrow\; \Delta_i \equiv (-1)^i \, c_{i\downarrow} c_{i\uparrow} \end{aligned} \tag{2.27}$$

This PHT yields insight into some of the expected physics in the presence of attractive interactions. Long range magnetic order in the repulsive model implies long range charge and pairing order in the attractive model. Another common phenomenon in the repulsive case is the formation of singlets on adjacent sites. We now discuss this in detail because it will be important to our solution of the decorated honeycomb lattice in Chapter 4. In analogy with the formation of spin singlets in the repulsive case, for the attractive Hubbard and Holstein

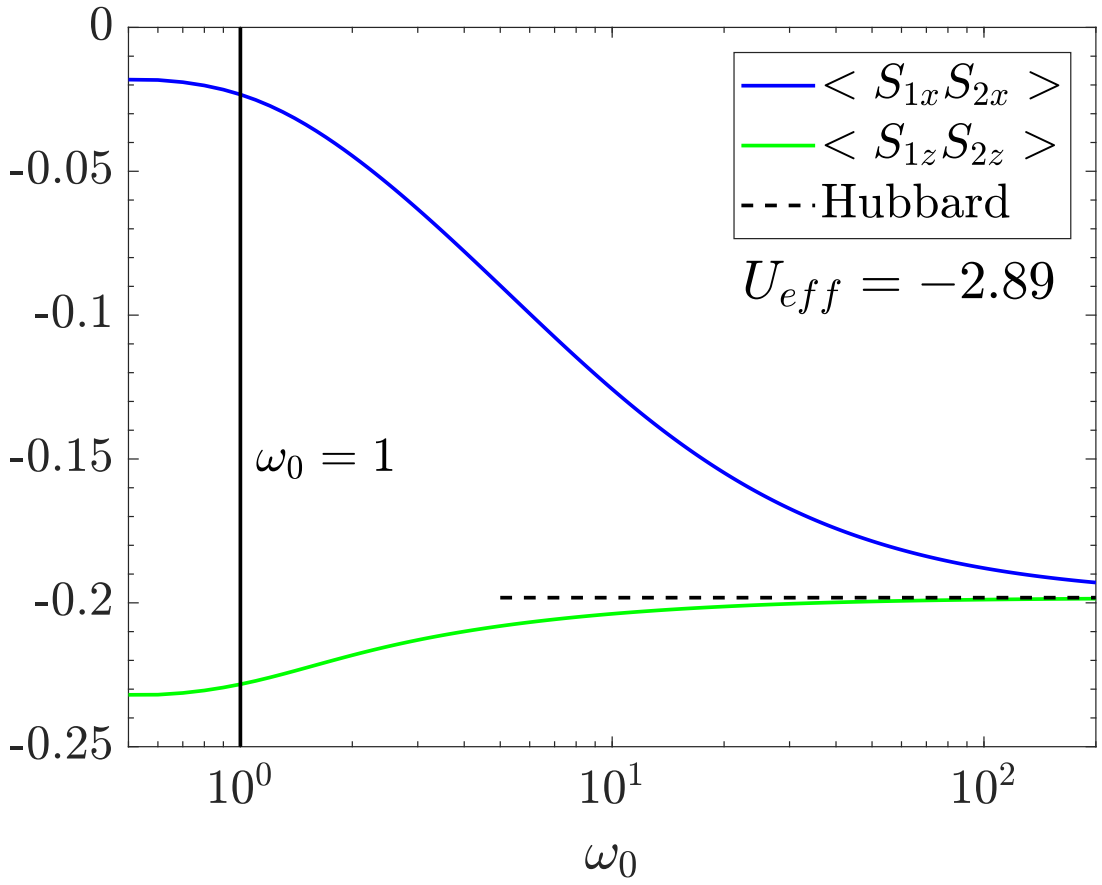

FIGURE 2.1. Exact diagonalization results for the ground state charge, $\langle S_1^z S_2^z \rangle$, and superconducting, $\langle S_1^x S_2^x \rangle$, correlators (in magnetic language) on a two site Holstein dimer, as a function of ω_0 at fixed $U_{\text{eff}} = -2.89$. The vertical line at $\omega_0 = 1$ shows the phonon frequency used in the phase diagram of Chapter 4 of this thesis. The dashed horizontal line is the Hubbard model result at $U = 2.89$. It is notable that values $\omega_0/t \lesssim 1$ are quite far from the limit where the spin correlations (CDW-pairing correlations) are symmetric.

models we expect the development of 'charge singlets' in which the three components of charge/pairing operators on the right side of Eq. (2.27) form local objects.

With this said, it is worth emphasizing that the Holstein $\leftrightarrow$ Hubbard mapping is exact only in the anti-adiabatic limit $\omega_0 \to \infty$. Figure 2.1 shows the effect of finite phonon frequency ω_0 on the different components of Eq. (2.27). Symmetry is restored as $\omega_0 \to \infty$, but for the values $\omega_0 = 0.1$ to 1 used in this dissertation, $|\langle S_1^z S_2^z \rangle| \gg |\langle S_1^x S_2^x \rangle|$. Thus,

while the analogy to magnetic physics is useful, it is far from clear how it will manifest itself quantitatively. (The fact that these correlators are less in magnitude than the singlet value $-1/4$ is due to charge fluctuations. As U also becomes large, they approach the Heisenberg limit $-\frac{1}{4}$ so that $\vec{S}_1 \cdot \vec{S}_2 = -\frac{3}{4}$.)

2.3. The Su-Schrieffer-Heeger Model

In the preceding section of this chapter, we introduced a type of electron-phonon interaction, the Holstein model, where the phonon position operator is correlated to electron density. Here let us discuss another type of electron-phonon interactions, where phonons live on the bonds of the lattice and their displacements $\hat{X}_{ij}$ are correlated to the electron hopping term. The Hamiltonian is

$$\begin{aligned}\mathcal{H} = & -t \sum_{\langle i,j\rangle,\sigma} \left(1 - \lambda \hat{X}_{ij}\right) \left(\hat{c}^{\dagger}_{i\sigma} \hat{c}_{j\sigma} + \text{h.c.}\right) - \mu \sum_{i,\sigma} \hat{n}_{i\sigma} \\ & + \sum_{\langle i,j\rangle} \left(\frac{1}{2M} \hat{P}^2_{ij} + \frac{M}{2} \omega_0^2 \hat{X}^2_{ij}\right) \\ & ,\end{aligned} \tag{2.28}$$

where $\hat{c}_{i\sigma}$ ($\hat{c}^{\dagger}_{i\sigma}$) is electron creation (annihilation) operator for spin $\sigma =\uparrow,\downarrow$ on site i, μ is the chemical potential, M is the phonon mass and ω_0 the phonon frequency. The bond phonon displacement and momentum operators are denoted as $\hat{X}_{ij}$ and $\hat{P}_{ij}$. As we discuss in Chapter 6, the magnitude of electron phonon coupling is given by the dimensionless parameter $g = \lambda/\sqrt{2M\omega_0/\hbar}$, so that the coupling term is $tg(\hat{b}_{ij} + \hat{b}^{\dagger}_{ij})(\hat{c}^{\dagger}_{i\sigma}\hat{c}_{j\sigma} + \text{h.c.})$. $\hat{n}_{i\sigma} = \hat{c}^{\dagger}_{i\sigma}\hat{c}_{i\sigma}$ is the density operator on site i. We will work in units for which $\hbar = t = M = 1$ and fix $\omega_0 = 1$.

SSH model in the anti-adiabatic limit: The SSH model turns into

$$\hat{H}_{eff} = -t \sum_{\langle i,j\rangle} \hat{K}_{ij} - \sum_{\langle i,j\rangle} \hat{K}^2_{ij}, \tag{2.29}$$

in the anti-adiabatic limit ($\omega_0 \to \infty$), since the effective electron interaction becomes instantaneous [**48**, **49**]. $\hat{K}_{ij}$ is the electron hopping term between site i and j. Notice that $\hat{K}_{ij}^2$ term can be re-expressed by using spin $\hat{S}_i, \hat{S}_j$ and pseudospin operators $\hat{\eta}_i, \hat{\eta}_j$.

$$-\frac{1}{4}\hat{K}_{ij}^2 \sim \hat{S}_i \cdot \hat{S}_j + \hat{\eta}_i \cdot \hat{\eta}_j \tag{2.30}$$

where $\hat{\eta}_i, \hat{\eta}_j$ can be obtained by applying PHT for spin down to the spin operators $\hat{S}_i, \hat{S}_j$. Thus the z component of pseudospin operators corresponds to charge density wave (CDW) order and x&y components reflect Superconductivity (SC), i.e. in the anti-adiabatic limit, AF, SC and CDW orders become degenerate. It would be interesting to explore these orders at finite ω_0 as well.

2.4. Summary

In this chapter, we started from first quantized Hamiltonians which describe the interactions between electrons and ions, and then briefly discussed the second quantized forms of the one- and two-body operators. This allowed us to introduce the iconic models people widely use to study electron-electron (Hubbard) and electron-phonon (Holstein, SSH) interactions. The Particle-Hole symmetry of the models have also been discussed. Finally, we introduced the effective model of the Holstein and SSH models in the anti-adiabatic limit. All these arguments lay important foundations for our numerical solution of these models on different geometries which will be expanded in the following chapters.

CHAPTER 3

A Review of Mean Field Theory and Quantum Monte Carlo Algorithms

In this Chapter, we will discuss the methods we use to study strongly correlated systems, including the Holstein model, and the Su-Schrieffer-Heeger-Hubbard (SSHH) model. Mean Field Theory will be introduced first. In this approach, we assume the four fermion quantum operator terms can be replaced by quadratic terms coupled to mean values. The reduced model can then be solved analytically. Although the results given by MFT will differ from the exact solutions (e.g. Quantum Monte Carlo (QMC)) in many cases, the rough picture of physics can still be captured.

After MFT, Determinant and Langevin QMC methods and their mathematical background will be illustrated. Monte Carlo methods can be viewed as "computer experiments", which generate configurations with desired distributions. It is an iterative stochastic procedure and can be used to solve complicated problems where an analytical solution is absent. Instead of getting an exact value/equation for the target observables, Monte Carlo simulations will generate many configurations with the appropriate probability distribution and measurements can be made based on them. After the process reaches its equilibrium, taking the average will give us a result consistent with the exact solution within error bars.

For classical problems, the Boltzmann distribution is the appropriate statistical distribution. Each configuration has a probability proportional to $e^{-\beta E}$, where E is the energy and $\beta = 1/k_B T$ is the inverse temperature. Then we can use some well designed algorithms, e.g. Metropolis Algorithm, to decide whether we accept or reject a suggested configuration and

make measurements correspondingly. These methods guarantee the configurations are generated according to the Boltzmann distribution as well be shown in Sec. 3.2. For quantum problems, there isn't a probability distribution directly associated with classical configurations since the energy, a number, is replaced by an operator, the Hamiltonian. This requires us to map the quantum problem into a new classical problem with one higher dimension. But we will see that the "probability" of the resulting patterns might not always be positive. This is called the "sign problem" in QMC methods. Despite this limitation, there are still lots of strongly correlated Hamiltonians which are free of the sign problem and can be solved efficiently by using QMC methods. More details will be discussed in the following.

3.1. Mean Field Theory

In this section, we will use the Holstein model on a Lieb lattice as an example to discuss how to use the Mean Field Theory approach to understand the physics in a strongly correlated system with electron-phonon interactions. The Lieb lattice is of special interest since it contains a flat electronic band in the non-interacting limit. It is also the structure of the CuO_2 planes of the cuprate superconductors. The Lieb lattice structure is shown in Fig. 3.1 and has three sites per unit cell and contains three unit cells along both $\vec{a}_1$ and $\vec{a}_1$ directions, where $\vec{a}_1 = (1, 0)$ and $\vec{a}_2 = (0, 1)$ are basis vectors. The total number of sites $N = 3 \times (L \times L) = 3 \times (3 \times 3) = 27$ in Fig. 3.1.

The Mean Field Theory (MFT) method is the simplest approach to study strongly correlated systems. Although the tendency of getting an ordered pattern is overestimated in the mean field approximation, since it ignores fluctuations. Hence, for example, the transition temperature obtained for the Holstein model by MFT is higher than QMC results. However, it can still be used to capture physics quantitatively to some extent. The idea of MFT is to use some simple ansatz, i.e. some average values of the field, to replace the original operators in the Hamiltonian. After applying the ansatz, original cubic or quartic terms in

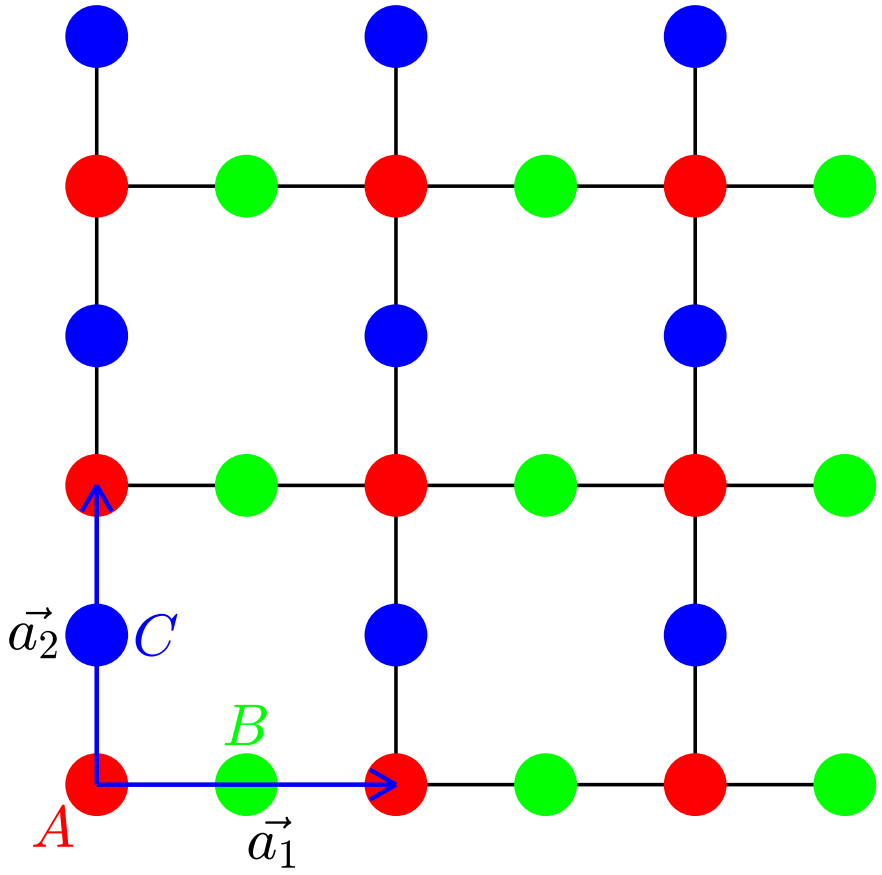

FIGURE 3.1. The Lieb lattice geometry. Additional sites (blue and green) are added to midpoint of each of the bonds linking the sites of a square lattice (red). The resulting structure is bipartite and has three sites per unit cell.

the Hamiltonian can be reduced to a quadratic form and then we can solve for energy levels, the partition function and operator expectation values analytically.

For the MFT treatment of the Holstein model we will discuss here, we use the adiabatic approximation, ignoring the $\hat{p}_i^2$ term, and assume a staggered pattern of phonon displacements with the ansatz $\hat{x}_i \to \langle \hat{x}_i \rangle = x_0 - \Delta$ and $\langle \hat{x}_i \rangle = x_0 + \Delta$ for different sublattice A and B&C respectively. The basic idea is that the Holstein model favors doubly occupied sites (and hence empty ones if the filling is fixed). Inserting this ansatz into Eq. 2.22, the

resulting quadratic fermion Hamiltonian,

$$\begin{aligned}\hat{H}_{MF} &= \frac{1}{2}\omega_0^2\frac{N}{3}[(x_0-\Delta)^2+(x_0+\Delta)^2+(x_0+\Delta)^2] \\ &+ (\lambda x_0-\mu)\sum_{\vec{l},\sigma}(\hat{n}_{\vec{l},A,\sigma}+\hat{n}_{\vec{l},B,\sigma}+\hat{n}_{\vec{l},C,\sigma}) \\ &+ \lambda\Delta\sum_{\vec{l},\sigma}(-\hat{n}_{\vec{l},A,\sigma}+\hat{n}_{\vec{l},B,\sigma}+\hat{n}_{\vec{l},C,\sigma}) \\ &- t\sum_{\vec{l},\sigma}(\hat{c}^\dagger_{\vec{l},A,\sigma}\hat{c}_{\vec{l},B,\sigma}+\hat{c}^\dagger_{\vec{l},A,\sigma}\hat{c}_{\vec{l},C,\sigma}+\hat{c}^\dagger_{\vec{l}+\vec{a}_1,A,\sigma}\hat{c}_{\vec{l},B,\sigma}+\hat{c}^\dagger_{\vec{l}+\vec{a}_2,A,\sigma}\hat{c}_{\vec{l},C,\sigma}+h.c.)\end{aligned} \tag{3.1}$$

can be diagonalized analytically, where $\vec{l}$ represents the unit cell. To do this, we take the Fourier Transform of electron creation and annihilation operators and insert the relation

$$\hat{c}^\dagger_{\vec{l},A/B/C,\sigma} = \frac{1}{\sqrt{N}}\sum_{\vec{k}}\hat{c}^\dagger_{\vec{k},A/B/C,\sigma}e^{i\vec{k}\cdot\vec{l}} \tag{3.2}$$

into Eq. (3.1). The resulting Hamiltonian can be written into a matrix form

$$\begin{aligned}\hat{H}_{MF} &= \frac{1}{2}\omega_0^2 N(x_0^2+\Delta^2)+\frac{1}{3}\omega_0^2 N x_0\Delta \\ &+\sum_{\vec{k},\sigma}\begin{pmatrix}\hat{c}^\dagger_{\vec{k},A,\sigma} & \hat{c}^\dagger_{\vec{k},B,\sigma} & \hat{c}^\dagger_{\vec{k},C,\sigma}\end{pmatrix} \\ &\begin{pmatrix}\lambda x_0-\mu-\lambda\Delta & -t-te^{ik_x} & -t-te^{ik_y} \\ -t-te^{-ik_x} & \lambda x_0-\mu+\lambda\Delta & 0 \\ -t-te^{-ik_y} & 0 & \lambda x_0-\mu+\lambda\Delta\end{pmatrix}\begin{pmatrix}\hat{c}_{\vec{k},A,\sigma} \\ \hat{c}_{\vec{k},B,\sigma} \\ \hat{c}_{\vec{k},C,\sigma}\end{pmatrix}\end{aligned} \tag{3.3}$$

We can diagonalize the matrix and get the three fermion energy bands,

$$\epsilon_{\alpha,\sigma}(\vec{k}) = \begin{cases}\lambda\Delta+\lambda x_0-\mu, \\ \pm\sqrt{(\lambda\Delta)^2+4t^2(\cos^2\frac{k_x}{2}+\cos^2\frac{k_y}{2})}+\lambda x_0-\mu\end{cases} \tag{3.4}$$

where $\vec{k}=(k_x,k_y)$; $k_x,k_y=\frac{2\pi n}{L}, n=1,2,\cdots,L$ (L is the number of unit cells along x/y direction.) are allowed momentum vectors. Then the free energy can be obtained, as a

function of x_0, Δ and inverse temperature β,

$$F = \frac{1}{2}N\omega_0^2(x_0^2 + \Delta^2 + \frac{2}{3}x_0\Delta) - \frac{1}{\beta}\sum_{\alpha,\sigma,\vec{k}} \ln\left(1 + e^{-\beta\epsilon_{\alpha,\sigma}(\vec{k})}\right), \tag{3.5}$$

At a fixed temperature T, we determine the (x_0^*, Δ^*) which minimizes F. Results obtained by this approach will be presented in the following sections.

3.2. Markov chain Monte Carlo

A Markov chain is a process to generate a series of values $X^{(1)}, X^{(2)}, \cdots X^{(t)}, \cdots$ of a random variable X where the probability of getting the current value X^t only depends only on its previous configuration X^{t-1}, i.e.

$$P(X^{(t)}|X^{(t-1)}, \cdots, X^{(1)}) = P(X^{(t)}|X^{(t-1)}). \tag{3.6}$$

We will use the superscript (t) to represent the time and subscript $i, j, \cdots$ to stand for different configurations. The probability of configuration i at time t, $X^t = X_i$ is denoted as $p_i^{(t)}$. A Markov chain can be defined by an initial probability of all the configurations and a transition probability matrix, with entries $P_{ij} = P(X_i|X_j)$, each column of which is normalized to 1, $\sum_i P_{ij} = 1$. The next time step configuration can be generated iteratively by

$$p_i^{(t+1)} = \sum_j P_{ij} p_j^{(t)}, \tag{3.7}$$

where $p^{(0)} = [p_1^{(0)}, p_2^{(0)}, \cdots, p_i^{(0)} \cdots]^T$ is the initial probability of all configurations. We repeat this process and get a series of values. If the series converges, we will have the stationary condition,

$$p_i = \sum_j P_{ij} p_j. \tag{3.8}$$

Metropolis et al. found that we will obtain the desired distribution p_i if the transition probability obeys the detailed balance,

$$P_{ij}p_j = P_{ji}p_i. \tag{3.9}$$

Before we move on, let us look at several important properties of a transition probability matrix. 1) It has an eigenvalue equal to 1. This can be easily verified by considering the normalization of each column in a transition probability matrix. A vector with all entries equal to 1 is the left eigenvector of the transition probability matrix with eigenvalue 1, i.e. $\sum_i v_i P_{ij} = \sum_i P_{ij} = 1 = v_j$. 2) 1 is the largest eigenvalue of a transition probability matrix. Assume it has some other eigenvalue λ and the eigen-function is $\sum_j P_{ij} v_j = \lambda v_i$. Using the triangle inequality, we get $\sum_j P_{ij}|v_j| \geq |\lambda||v_i|$. Take the sum over i on both sides and use the relation $\sum_i P_{ij} = 1$. We get $\sum_j |v_j| \geq |\lambda| \sum_i |v_i|$. Then $|\lambda| \leq 1$ is obtained.

Another important matter we need to emphasize here, which is also a requirement for Monte Carlo methods to work, is, in order to get an unique stationary distribution, the transition probability needs to be a primitive stochastic matrix (which is also called ergodicity). A stochastic matrix is a matrix with no negative matrix elements and each column normalized to be 1. These are obviously precisely the properties a transition matrix would have. Primitive matrices contain two properties, one is irreducible and the other one is aperiodic. Irreducible means a matrix is not similar to a block upper triangular matrix

$$\begin{pmatrix} A & B \\ 0 & C \end{pmatrix}, \tag{3.10}$$

via a permutation, where A and C are square matrices with arbitrary dimensions. Aperiodic means a matrix cannot be transformed into the form

$$\begin{pmatrix} 0 & A_1 & 0 & \cdots & 0 \\ \vdots & 0 & A_2 & \ddots & \vdots \\ \vdots & \vdots & 0 & \ddots & 0 \\ \vdots & \vdots & \vdots & \ddots & A_{n-1} \\ A_n & 0 & 0 & \cdots & 0 \end{pmatrix}, \tag{3.11}$$

via a permutation.

Ergodicity of a matrix P guarantees the right eigenvector of it with eigenvalue equal to 1 is unique and positive. Imagine we have some initial probability

$$p^{(0)} = \sum_{\alpha} a_\alpha \phi_\alpha, \tag{3.12}$$

where $a_1 = 1$ and $1 \geq |\lambda_1| \geq |\lambda_2| \geq \ldots$, expressed as a combination of eigenvectors ϕ_α with corresponding eigenvalues λ_α of the probability matrix P. Let the probability matrix P act on the initial probability p_i^0, k times,

$$P^k p^{(0)} = \phi_1 + \sum_{\alpha \geq 2} \lambda_\alpha^k \phi_\alpha. \tag{3.13}$$

When the number of Markov chain Monte Carlo iterations k is sufficiently large, the eigenvector with eigenvalue equal to 1 which is the target distribution dominates in the right hand side, i.e. the probability distribution converges to the desired distribution after sufficient number of iterations. This process does not depend on the initial probability p_i^0 as long as it is not orthogonal to ϕ_1.

3.3. Classical Monte Carlo

Monte Carlo methods have been widely used to study complicated problems, e.g. in statistical physics, which we can not solve analytically. In this section we will start with classical models and discuss how to update the configuration, whether to accept or reject the proposed move, in order to satisfy the detailed balance and make computers generate configurations according to the target probability distribution.

3.3.1. The master equation

As noted in the preceding section, in classical statistical mechanics, the probability of the system in a particular state (configuration) $|n\rangle$ with energy E_n is given by the Boltzmann distribution

$$P(n) = \frac{1}{Z} e^{-\beta E_n}, \tag{3.14}$$

where $Z = \sum_n e^{-\beta E_n}$ is the partition function. For a many-body problem, the size of the Hilbert space grows exponentially with the lattice size. If the local degrees of freedom have n choices and the total number of sites is N, then the total number of possible configurations is n^N. For a relatively large system N, the size of configuration space n^N is too large to enumerate all the states (e.g. For the Ising model ($n = 2$) on a 8×8 square lattice ($N = 64$), the total number of possible states is 2^{64}. It would take $2^{64}/10^9 \sim 10^{10}$ seconds $\sim 10^5$ days to generate configurations) and we need to use Monte Carlo techniques to sample the configurations with the desired Boltzmann probability distribution efficiently. The point is that most of the enormous number of configurations are very unlikely. Monte Carlo "importance sampling" steers the sampling to the important region of phase space which is much smaller. For an observable $\mathcal{O}$, its average value can be calculated by

$$\langle \hat{O} \rangle = \frac{1}{N_{meas}} \sum_{l=1}^{N_{meas}} O_l, \tag{3.15}$$

where N_{meas} is the number of measurements and O_l is the value for observable $\hat{O}$ in configuration l.

In the preceding section, we already argued that if the probability matrix satisfies the detailed balance, we will get the target probability distribution. Here let us discuss it in more detail. Let $p_i(t)$ be the probability of having configuration i at time t. P_{ij} is the probability per unit time for the system to transform from configuration j to configuration i. Then we can derive the master equation which describe how the probability of configuration i evolves with time,

$$\frac{dp_i^{(t)}}{dt} = \sum_{j \neq i} [p_j^{(t)} P_{ij} - p_i^{(t)} P_{ji}] \tag{3.16}$$

After the Monte Carlo process reaches its equilibrium, we have the stationary condition,

$$\lim_{t \to \infty} p_i^{(t)} = p_i \tag{3.17}$$

where p_i is the desired Boltzmann distribution. It implies when $t \to \infty$, both sides of Eq. (3.16) tend to be 0. Naturally we can impose the sufficient but not necessary condition, detailed balance Eq. (3.9)

3.3.2. Detailed Balance Algorithms

Metropolis Algorithm The simplest and commonly used algorithm that satisfies the detailed balance condition is the Metropolis Algorithm. The procedures are the following:

1) suggest a move to a new configuration j from the current configuration i

2) If the new configuration is more likely than the original one, i.e. $p_j > p_i$, directly accept the new configuration j; if the new configuration is less likely, i.e. $p_j < p_i$, accept the new

proposed configuration with probability p_j/p_i. That is,

$$P_{ji} = \begin{cases} p_j/p_i = e^{-\beta(E_j - E_i)}, & \text{if } \mathrm{p_j} < \mathrm{p_i}, \text{ or } \mathrm{E_j} > \mathrm{E_i} \\ 1, & \text{otherwise} \end{cases} \tag{3.18}$$

3) take measurements and repeat all these processes

Step 1) is actually a bit subtle. One must suggest j "randomly", i.e. not introduce any specific bias in the selection process. For example, for a continuous degree of freedom x, step 1) might suggest x' randomly on $[x - \Delta, x + \Delta]$, where Δ is some step size. But suggesting x' on $[x - \Delta, x + 2\Delta]$ would give incorrect results. It is fairly easy to see the latter choice would violate detailed balance.

We can easily verify that constructing the transition probability matrix as above satisfies detailed balance: if $E_j > E_i$, $P_{ji} = e^{-\beta(E_j - E_i)}$, $P_{ij} = 1$; and if $E_j < E_i$, $P_{ji} = 1$, $P_{ij} = e^{-\beta(E_i - E_j)}$.

Heat Bath Algorithm The main difference between Heat Bath and Metropolis algorithm is that Heat Bath Algorithm does not reject configurations explicitly. The new configuration j is accepted with probability,

$$P_{ji} = \frac{1}{\exp[\beta(\mathrm{E_j} - \mathrm{E_i})] + 1} \tag{3.19}$$

instead of depending on the sign of $E_j - E_i$. It can also be verified detailed balance is satisfied using the Heat Bath Algorithm.

3.4. Determinant Quantum Monte Carlo

In this section, we will discuss the Determinant Quantum Monte Carlo methods commonly used simulating in electron-electron (e.g. Hubbard) and electron-phonon (e.g. Holstein and SSH) coupling models. In this approach, the full imaginary time propagator $e^{-\beta\hat{H}}$

is written as a product of incremental factors $e^{-\Delta\tau\hat{H}}$. This discretization allows for the 'Trotter' approximation, $e^{-\Delta\tau\hat{H}} \approx e^{-\Delta\tau\hat{H}_1}e^{-\Delta\tau\hat{H}_2}$ with $\hat{H} = \hat{H}_1 + \hat{H}_2$. The purpose of dividing up the imaginary time evolution is to isolate the interactions so that the trace over the fermions can be evaluated analytically. The key point is that a trace over a product of exponentials of quadratic forms in fermion operators can be performed analytically. After the Trotter approximation, electron-phonon models are already in this form. Electron-electron models can be put in this form by introducing a Hubbard-Stratonovich field to decouple the interactions. The partition function of the system can be written as a sum of a product of two determinants which are the result of the trace, one for spin up and one for spin down. In electron-phonon models, there are factors determined by the pure phonon part of $\hat{H}$ as well. For the Holstein model, because the up and down species couple to the phonon coordinate in the same way, the determinants are identical. The fermion sign problem is absent in the resulting square of determinants.

DQMC treats interacting quantum Hamiltonians exactly. The sole (controlled) approximation is in the discretization of β. With the usual choices of $\Delta\tau$ the associated errors are easily made smaller than those arising from the sampling. (The exception is for local quantities like the energy and double occupancy whose statistical errors are extremely small. For these observables, a $\Delta\tau \to 0$ extrapolation is straightforward to perform.) Simulations are carried out on lattices of finite size, necessitating a finite size scaling analysis, as described in the later chapters. We now provide details of this algorithm by considering specific Hamiltonians.

3.4.1. DQMC for the Hubbard model: Hubbard-Stratonovich Transformation

In statistical mechanics, the partition function of a quantum system can be written as

$$Z = Tr(e^{-\beta\hat{H}}). \tag{3.20}$$

The Hubbard Hamiltonian involves an electron hopping term combined with a chemical potential term

$$\hat{K} = -t \sum_{\langle i,j \rangle} (\hat{c}^{\dagger}_{i,\sigma} \hat{c}_{j,\sigma} + \hat{c}^{\dagger}_{j,\sigma} \hat{c}_{i,\sigma}) - \mu \sum_{i} (\hat{n}_{i,\uparrow} + \hat{n}_{i,\downarrow}) \tag{3.21}$$

and an onsite Coulomb repulsion term,

$$\hat{V} = U \sum_{i} (\hat{n}_{i,\uparrow} - \frac{1}{2})(\hat{n}_{i,\downarrow} - \frac{1}{2}). \tag{3.22}$$

We first divide β into L terms, $\beta = \Delta\tau L_\tau$ and re-express the partition function as

$$\begin{aligned} Z &= Tr(e^{-\beta \hat{H}}) \\ &= Tr(\underbrace{e^{-\Delta\tau \hat{H}} e^{-\Delta\tau \hat{H}} \dots e^{-\Delta\tau \hat{H}}}_{L_\tau \text{ terms}}). \end{aligned} \tag{3.23}$$

and then employ the Suzuki-Trotter approximations,

$$e^{-\Delta\tau(\hat{A}+\hat{B})} = e^{-\Delta\tau \hat{A}} e^{-\Delta\tau \hat{B}} + \mathcal{O}((\Delta\tau)^2), \tag{3.24}$$

where $\hat{A}$ and $\hat{B}$ are operators and do not commute with each other $[\hat{A}, \hat{B}] \neq 0$. A higher order approximation can be realized by,

$$e^{-\Delta\tau(\hat{A}+\hat{B})} = e^{-\Delta\tau \hat{B/}2} e^{-\Delta\tau \hat{A}} e^{-\Delta\tau \hat{B/}2} + \mathcal{O}((\Delta\tau)^3), \tag{3.25}$$

Apply the higher order Trotter approximation Eq.(3.25) to the partition function Eq.(3.23),

$$\begin{aligned} Z &= Tr(\underbrace{e^{-\Delta\tau \hat{K/}2} e^{-\Delta\tau \hat{V(1)}} e^{-\Delta\tau \hat{K}} e^{-\Delta\tau \hat{V(2)}} \dots e^{-\Delta\tau \hat{K}} e^{-\Delta\tau \hat{V}(\hat{L}_\tau)} e^{-\Delta\tau \hat{K/}2}}_{L_\tau \text{ terms}}) + \mathcal{O}((\Delta\tau)^2) \\ &= Tr(e^{-\Delta\tau \hat{K}} e^{-\Delta\tau \hat{V(1)}} e^{-\Delta\tau \hat{K}} e^{-\Delta\tau \hat{V(2)}} \dots e^{-\Delta\tau \hat{K}} e^{-\Delta\tau \hat{V}(\hat{L}_\tau)} + \mathcal{O}((\Delta\tau)^2). \end{aligned} \tag{3.26}$$

The second row in the above equation is obtained by using the cyclic property of the trace. Since Trotter errors are accumulated in L_τ terms, the total error is of order $\mathcal{O}((\Delta\tau)^3 L_\tau) \sim$

$\mathcal{O}((\Delta\tau)^2)$. The imaginary time step $\Delta\tau$ is usually chosen to satisfy $tU(\Delta\tau)^2 < 1/10$ such that the imaginary time discretization error is negligible.

Before we move on, let us introduce some general identities we need to use in the later derivation. If the Hamiltonian in the second quantized form can be written as

$$H(l) = \begin{pmatrix} \hat{c}^\dagger_{1\sigma} & \hat{c}^\dagger_{2\sigma} & \cdots \end{pmatrix} \begin{pmatrix} h(l)_{11} & h(l)_{12} & \cdots \\ h(l)_{21} & h(l)_{22} & \cdots \\ \vdots & \vdots & \ddots \end{pmatrix} \begin{pmatrix} \hat{c}_{1\sigma} \\ \hat{c}_{2\sigma} \\ \vdots \end{pmatrix} \tag{3.27}$$

then the partition function

$$\begin{aligned} Z &= Tr(e^{-\Delta\tau H(1)} e^{-\Delta\tau H(2)} \cdots e^{-\Delta\tau H(L)}) \\ &= \det(\mathrm{I} + \mathrm{e}^{-\Delta\tau \mathrm{h}(1)} \mathrm{e}^{-\Delta\tau \mathrm{h}(2)} \cdots \mathrm{e}^{-\Delta\tau \mathrm{h}(\mathrm{L})}) \end{aligned} \tag{3.28}$$

and fermions Green function

$$\begin{aligned} G_{ij} = \langle c_{i\sigma} c^\dagger_{j\sigma} \rangle &= Z^{-1} Tr(c_{i\sigma} c^\dagger_{j\sigma} e^{-\Delta\tau H(1)} e^{-\Delta\tau H(2)} \cdots e^{-\Delta\tau H(L)}) \\ &= [I + e^{-\Delta\tau h(1)} e^{-\Delta\tau h(2)} \cdots e^{-\Delta\tau h(L)}]^{-1}_{ij} \end{aligned} \tag{3.29}$$

In order to use the above formalism to perform traces for fermions, we implement the Hubbard-Stratonovich Transformation to convert the quartic onsite Coulomb repulsion term into a quadratic form. The Hubbard-Stratonovich Transformation has many different forms and here we will focus on the one introducing a discrete auxiliary field, which can be sampled more efficiently. For the repulsive Hubbard ($U > 0$) model, the transformation is

$$e^{-\Delta\tau U(n_{i,\uparrow} - \frac{1}{2})(n_{i,\downarrow} - \frac{1}{2})} = \frac{1}{2} e^{-\Delta\tau U/4} \sum_{s_i = \pm 1} e^{\lambda s_i (n_{i,\uparrow} - n_{i,\downarrow})} \tag{3.30}$$

where λ is defined by $\cosh(\lambda) = \exp(\Delta\tau U/2)$. For the attractive Hubbard model ($U < 0$), the transformation becomes

$$e^{-\Delta\tau U(n_{i,\uparrow} - \frac{1}{2})(n_{i,\downarrow} - \frac{1}{2})} = \frac{1}{2} e^{+\Delta\tau U/4} \sum_{s_i = \pm 1} e^{\lambda s_i (n_{i,\uparrow} + n_{i,\downarrow} - 1)}. \tag{3.31}$$

Notice we need a variable at each site i of the spatial lattice and also at each imaginary time slice l in Eq.(3.23). Applying the Hubbard-Stratonovich Transformation and using the identities of (3.28),(3.29), we finally get the partition function, which can be expressed as a summation of statistical weights over all the possible HS field configurations and the weight can be written as a product of two determinants, one for spin up and one for spin down.

$$Z = \sum_{s(i,l)} \det(\mathrm{M}_\uparrow)\det(\mathrm{M}_\downarrow), \tag{3.32}$$

where $s(i,l) = \pm 1$ is Hubbard-Stratonovich (HS) variable for site i at time slice l and

$$M_\sigma = I + B_L^\sigma B_{L-1}^\sigma \cdots B_1^\sigma, \tag{3.33}$$

where I is a $N \times N$ identity matrix and the equal time single particle propagator

$$B_l^{\uparrow(\downarrow)} = e^{\mp v(l)} e^{-k} \tag{3.34}$$

Here k is the matrix corresponding to the electron kinetic energy part. Using $N = 6$, $1D$ chain with periodic boundary condition system as an example,

$$k = \Delta\tau \begin{pmatrix} -\mu & -t & 0 & 0 & 0 & -t \\ -t & -\mu & -t & 0 & 0 & 0 \\ 0 & -t & -\mu & -t & 0 & 0 \\ 0 & 0 & -t & -\mu & -t & 0 \\ 0 & 0 & 0 & -t & -\mu & -t \\ -t & 0 & 0 & 0 & -t & -\mu \end{pmatrix} \tag{3.35}$$

Usually the "checkerboard decomposition" is employed to make the calculation of e^{-k} rapid. $v(l)$ reflects the onsite Coulomb interaction, with HS variables for different sites i (which

runs from 1 to N) and time slice l (which runs from 1 to L) on the diagonal line,

$$v(l) = \lambda \begin{pmatrix} s(1,l) & 0 & 0 & \cdots & 0 \\ 0 & s(2,l) & 0 & \cdots & 0 \\ 0 & 0 & s(3,l) & \cdots & 0 \\ 0 & 0 & 0 & \ddots & 0 \\ 0 & 0 & 0 & \cdots & s(N,l) \end{pmatrix} \tag{3.36}$$

where each HS variable can be randomly chosen as ± 1 initially.

The original $2D$ quantum problem is converted into a $(2+1)D$ classical problem. $s(i,l)$ has an imaginary time index l in addition to its spatial index i. We can now follow the Metropolis algorithm for classical Monte Carlo to sample possible configurations of HS variables $s(i,l)$ according to its statistical weight $det(M_\uparrow)\det(\mathrm{M}_\downarrow)$.

Now let us discuss how to update configurations of HS variables in more detail below. If we calculate the matrix determinant for each updated configuration, the algorithm scales as N^4L, since we have to calculate the determinant NL times to sweep over all the HS variables $s(i,l)$ and calculating a determinant requires N^3 operations. In order to make the algorithm more efficient, we use the "Sherman Morrison Formula" and calculate the Green function for the updated configuration from its previous calculated Green function for the preceding configuration.

Let us first define the single particle equal-time Green's function

$$G_\sigma(l) = [I + B_l^\sigma \cdots B_1^\sigma B_L^\sigma \cdots B_{l+1}^\sigma]^{-1} = [I + A(l)]^{-1} = [M(l)]^{-1} \tag{3.37}$$

Note that the determinant does not depend on time slice l, i.e. we have $\det(\mathrm{M}_\sigma) = \det(\mathrm{G}_\sigma^{-1}(\mathrm{l}))$ for arbitrary l values. Once the current time slice Green's function $G_\sigma(l)$ has been calculated, the next time slice Green's function $G_\sigma(l+1)$ can be derived by matrix

multiplications, which only takes $\mathcal{O}(N^2)$ operations,

$$G_\sigma(l+1) = B^\sigma_{l+1} G_\sigma(l) [B^\sigma_{l+1}]^{-1}, \tag{3.38}$$

because B^σ_l are sparse matrices.

One needs to sweep over all the sites at different time slices to update HS variables configurations. Instead of calculating the new determinant for each sweep, we only care about the ratio of the determinant for the new proposed configuration and the one for the previous pattern, which is the probability of acceptance of the new configuration.

$$R = R_\uparrow R_\downarrow = \frac{\det(\mathrm{M}'_\uparrow)\det(\mathrm{M}'_\downarrow)}{\det(\mathrm{M}_\uparrow)\det(\mathrm{M}_\downarrow)} \tag{3.39}$$

Now let us derive the formula for R and express it by using Green's function at time slice l. Assume at time slice l after the update of HS variable on a single site i, the new $A'(l)$ can be expressed as

$$A'(l) = [I + \Delta(i,l)A(l)], \tag{3.40}$$

where

$$\Delta(i,l)_{jk} = \delta_{ij}\delta_{ik}[\exp(2\Delta\tau \mathrm{s(i,l)}) - 1]. \tag{3.41}$$

Let us ignore the index sigma for a moment and get an expression applied for both spin up and down,

$$\begin{aligned} R &= \frac{\det(\mathrm{M}')}{\det(\mathrm{M})} = \det(\mathrm{M}'\mathrm{G}) \\ &= \det\Big[\big(\mathrm{I} + (\mathrm{I} + \Delta(\mathrm{i},\mathrm{l}))\mathrm{A}(\mathrm{l})\big)\mathrm{G}(\mathrm{l})\Big] \\ &= \det\Big[\big(\mathrm{M}(\mathrm{l}) + \Delta(\mathrm{i},\mathrm{l})\mathrm{A}(\mathrm{l})\big)\mathrm{G}(\mathrm{l})\Big] \\ &= \det\Big[\mathrm{I} + \Delta(\mathrm{i},\mathrm{l})(\mathrm{I} - \mathrm{G}(\mathrm{l}))\Big] \\ &= 1 + \Delta(i,l)_{ii}(1 - G(l)_{ii}) \end{aligned} \tag{3.42}$$

In the above derivation, we use the identity $I = G(l) + A(l)G(l)$ and this is obtained from multiplying $G(l)$ to the both sides of the relation $M(l) = I + A(l)$. Similarly, we can also figure out an expression for $G'(l)$ using the Sherman Morrison Formula,

$$\begin{aligned} G'(l) &= [M'(l)]^{-1} = [I + A'(l)]^{-1} \\ &= [M(l) + \Delta(i,l)A(l)]^{-1} \\ &= G(l) - \frac{G(l)\Delta(i,l)(I - G(l))}{1 + [1 - G(l)_{ii}]\Delta(i,l)_{ii}} \end{aligned} \tag{3.43}$$

Since $\Delta(i,l)$ has only one nonzero element, it is very efficient to use Eq.(3.42)(3.43) to update phonon displacements for all the sites. Once the update is done for time slice l, we can use Eq.(3.38) to get the Green's function for the next time slice $l+1$.

3.4.2. DQMC for the Holstein model: Feynman path integral

Unlike in the Hubbard model, where the Hamiltonian has a quartic onsite Coulomb potential term $Un_{i\uparrow}n_{i\downarrow}$ which can be decoupled to quadratic forms by introducing a Hubbard-Stratonovich transformation, in the Holstein model, we have the electron-phonon coupling term $\lambda\sum_{i,\sigma}\hat{n}_{i,\sigma}\hat{x}_i$ instead, where $\hat{n}_{i,\sigma} = \hat{c}^{\dagger}_{i,\sigma}\hat{c}_{i,\sigma}$ is the density operator. A path integral converts the phonon displacement operators into numbers, thus the original Hamiltonian

will become quadratic in terms of electron creation and annihilation operators and can be diagonalized analytically.

Let us first use the simple Quantum Harmonic Oscillator as an example to illustrate how to introduce a path integral to solve phonon problems and convert the original quantum d dimensional Hamiltonian into a $d+1$ dimensional classical problem. The Hamiltonian for a simple Quantum Harmonic Oscillator is

$$\hat{H} = \frac{1}{2}\hat{p}^2 + \frac{1}{2}\omega_0^2\hat{x}^2 \tag{3.44}$$

After implementing the Trotter approximation, we will get an expression for the partition function,

$$\begin{aligned} Z &= Tr(e^{-\beta H}) = Tr(e^{-\Delta\tau H}e^{-\Delta\tau H}\dots e^{-\Delta\tau H}) \\ &\approx Tr(e^{-\frac{1}{2}\Delta\tau\hat{p}^2}e^{-\frac{1}{2}\Delta\tau\omega_0^2\hat{x}^2}\dots e^{-\frac{1}{2}\Delta\tau\hat{p}^2}e^{-\frac{1}{2}\Delta\tau\omega_0^2\hat{x}^2}) \\ &= \int_{-\infty}^{+\infty} dx_1dx_2\dots dx_L\langle x_1|e^{-\frac{1}{2}\Delta\tau\hat{p}^2}e^{-\frac{1}{2}\Delta\tau\omega_0^2\hat{x}^2}|x_2\rangle\dots\langle x_L|e^{-\frac{1}{2}\Delta\tau\hat{p}^2}e^{-\frac{1}{2}\Delta\tau\omega_0^2\hat{x}^2}|x_1\rangle \end{aligned} \tag{3.45}$$

Each individual term in the above equation can be obtained by inserting eigenstates of momentum operators. For example (recall $\hbar = 1$),

$$\begin{aligned} \langle x_1|e^{-\frac{1}{2}\Delta\tau\hat{p}^2}e^{-\frac{1}{2}\Delta\tau\omega_0^2\hat{x}^2}|x_2\rangle &\sim \int_{-\infty}^{+\infty} e^{-\Delta\tau\frac{1}{2}\omega_0^2x_2^2}\langle x_1|e^{-\frac{1}{2}\Delta\tau\hat{p}^2}|p\rangle\langle p|x_2\rangle dp \\ &= e^{-\Delta\tau\frac{1}{2}\omega_0^2x_2^2}\int_{-\infty}^{+\infty} e^{-\frac{1}{2}\Delta\tau p^2}e^{ip(x_1-x_2)}dp \\ &= e^{-\Delta\tau\frac{1}{2}\omega_0^2x_2^2}e^{\frac{-(x_1-x_2)^2}{2\Delta\tau}} \end{aligned} \tag{3.46}$$

Plug Eqn. (3.46) into the partition function for quantum harmonic oscillator (3.45), we get

$$Z = \int e^{-S_{bose}(x_l)}dx_1dx_2\dots dx_L, \tag{3.47}$$

where

$$S_{bose}(x_l) = \Delta\tau(\frac{\omega_0^2}{2}\sum_l x_l^2 + \frac{1}{2}\sum_l(\frac{x_{l+1}-x_l}{\Delta\tau})^2) \tag{3.48}$$

In the Holstein model, we can follow exactly the same procedure to deal with electron-phonon coupling term and convert the original quantum problem into a classical problem with one higher dimension.

$$Z = \int d\vec{x}_1 d\vec{x}_2 d\ldots\vec{x}_L e^{-S_{bose}(\vec{x}_l)}\det(\mathrm{M}_\uparrow)\det(\mathrm{M}_\downarrow), \tag{3.49}$$

where $S_{bose}(\vec{x}_l) = \Delta\tau(\frac{\omega_0^2}{2}\sum_l \vec{x}_l^2 + \frac{1}{2}\sum_l(\frac{\vec{x}_{l+1}-\vec{x}_l}{\Delta\tau})^2)$ and $\vec{x}_l = (x_{1,l}, x_{2,l}, \ldots x_{N,l})$is a vector of dimension N, representing the phonon displacements for different sites $i = 1, 2, \ldots N$ at time slice l. $\vec{x}_l^2$ is defined as $\vec{x}_l^2 = \sum_i x_{i,l}^2$ The integrand can be viewed as the probability $P(x(i,l))$ for the phonon configuration $x(i,l)$, which depends on both site i and time slice l. It includes both a bosonic piece from the quantum oscillator term and a product of two determinants, one for spin up and one for spin down. For the Holstein model, because the spin-up and spin-down species play exactly the same role in the Hamiltonian, the determinants for spin up and down are identical. Thus the probability $P(x(i,l))$ is always positive and the Holstein model is free of sign problems. $x(i,\tau)$ needs to be sampled stochastically in the simulation. We need to follow the procedures discussed in Sec. 3.4.1 to update phonon fields $x(i,l)$ and calculate the acceptance probability of the suggested move and Green's functions using the Sherman Morrison formula.

3.5. Langevin Quantum Monte Carlo

The Langevin equation can also be applied in Monte Carlo simulations. A more detailed discussion about the algorithm can be found in Chapter 7. Here we will discuss some background of the Langevin QMC and show the Langevin equation satisfies the detailed balance condition.

Consider a system with energy $E(x)$, which depends on the degree of freedom x. We update the variable x via the Langevin Equation,

$$x' = x - \epsilon \frac{dE}{dx} + \sqrt{2\epsilon T} R, \tag{3.50}$$

where T is the temperature and R is a random variable that obeys the Gaussian distribution $p(R) = e^{-R^2/2}/\sqrt{2\pi}$. Thus the transition probability of changing from x to x' can be expressed as,

$$\begin{aligned} P(x \to x') &= e^{-1/2[x'-x+\epsilon dE/dx]^2/2\epsilon T}/\sqrt{2\pi} \\ &= e^{-[dx^2+2\epsilon dE+\epsilon^2(dE/dx)^2]/4\epsilon T}/\sqrt{2\pi}, \end{aligned} \tag{3.51}$$

where $dx = x' - x$ and $dE = E(x') - E(x)$. Similarly, we can also write out the transition probability of $x' \to x$,

$$P(x' \to x) = e^{-[dx^2-2\epsilon dE+\epsilon^2(dE/dx')^2]/4\epsilon T}/\sqrt{2\pi}, \tag{3.52}$$

Thus the ratio of these transition probabilities is,

$$\frac{P(x \to x')}{P(x' \to x)} = e^{-E(x')/T} e^{E(x)/T} \tag{3.53}$$

i.e.

$$P(x \to x') e^{-E(x)/T} = P(x' \to x) e^{-E(x')/T}. \tag{3.54}$$

We can clearly see from the above equation that detailed balance is satisfied up to errors of order ϵ. The application of Langevin QMC to the Holstein model on a layered square lattice will be discussed in Chapter 7.

CHAPTER 4

Charge density waves on a half-filled decorated honeycomb lattice

4.1. Introduction

Itinerant electrons on a honeycomb lattice host a Dirac spectrum in the absence of interactions which has attracted considerable attention [**23**–**28**]. The linearly vanishing density of states (DOS) at $E = 0$ forms an interesting counterpoint to that of the square lattice (of interest to cuprate superconductivity) whose DOS diverges (logarithmically) at $E = 0$. An immediate consequence is that, whereas in the square lattice long range antiferromagnetic (AF) correlations onset in the ground state for any finite repulsive interaction U, a nonzero critical U_c is required for AF order on the honeycomb lattice [**29**, **30**].

Recently, the effects of electron-phonon interactions on Dirac fermions have been explored [**1**, **2**]. Similar to the case of electron-electron interactions, the semi-metallic band structure requires a critical electron-phonon interaction strength for CDW formation at half-filling. A crucial difference is that, unlike Neél order which occurs only at $T = 0$ in the two dimensional Hubbard model [**79**], owing to the continuous nature of the spin symmetry being broken, the CDW transition occurs at finite temperature.

In this chapter we extend these investigations of the Holstein model on a honeycomb lattice by examining the effect of a regular pattern of non-uniform hopping. The particular 'Kekulé hopping texture' we investigate has been proposed [**80**] to give rise to nontrivial topological properties associated with an opening of a gap at the Dirac point, and linked to the 'pseudo-angular momentum' of electrons residing on sets of strongly hybridized hexagons. Similar 'decorated lattices' have been studied previously in the context of the depleted square lattice Heisenberg [**81**] and Hubbard [**82**] Hamiltonians as possible theoretical descriptions of

spin liquid phases in CaV_4O_9 [**83**–**87**]. It was shown that while long range antiferromagnetic correlations exist in the ground state when the hoppings t and t' are roughly balanced, spin liquid phases consisting of independent spin dimers or spin plaquettes are present when the hoppings are sufficiently unequal. Within mean field theory, a rich variety of spin-ordered phases, characterized by different patterns of spin inside and between the plaquettes, can arise as a function of doping and U in such decorated Hubbard models [**82**].

Strongly correlated physics in the presence of several kinetic energy scales gives rise to a further variety of phenomena in other important realizations, including orbitally-selective Mott transitions [**88**–**94**]. In the case of the Periodic Anderson Model (PAM) which includes both conduction c and local d orbitals, a dominant interorbital hopping $t_{cd} \gtrsim t_{cc}$ can lead to singlet formation and a spin-liquid ground state [**95**, **96**], as seen in QMC studies in $d = 1, 2, 3$ and $d = \infty$ [**97**–**100**]. As in the less widely studied case of decoration, the existence of several hopping energy scales whose difference is large disrupts magnetic order. Most of these investigations have focused on electron-electron interactions.

We will discuss some interesting analogies between the spin-singlet formation in such situations, and charge singlets in the electron-phonon case. However, it is important to emphasize that the Holstein model breaks the spin symmetry present in the Hubbard model, with charge order (the analog of ordering in the S^z channel) dominating over superconducting order (which maps onto S^x, S^y). As a result, the CDW transition in the half-filled 2D Holstein model occurs at finite temperature [**77**], whereas long range magnetic order in the 2D Hubbard model occurs only at $T = 0$. This breaking of symmetry introduces a fundamental difference between the physics of the repulsive Hubbard and Holstein models with multiple hopping energy scales, which is especially marked as the phonon frequency ω_0 decreases.

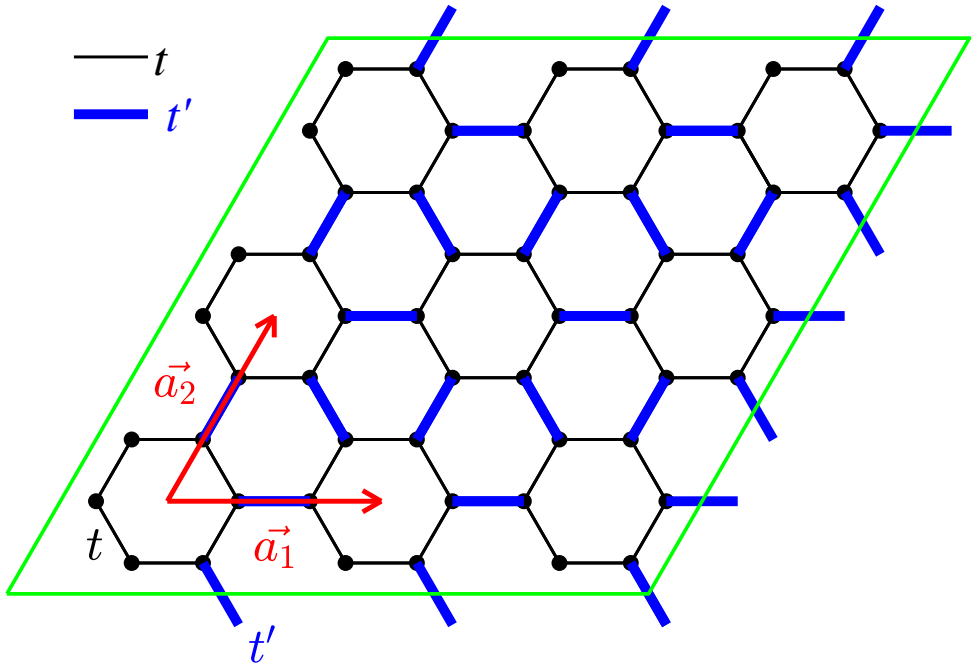

FIGURE 4.1. The structure of the 'decorated honeycomb lattice'. Two different hopping strengths are present. Hybridization t (thin black lines) links the sites of a collection of independent hexagons. These hexagons are then connected by t' (thick blue lines). In the $t' >> t$ limit, an alternate description in terms of elemental dimers linked by t is a more appropriate starting point.

4.2. Model and Methods

We investigate the Holstein Hamiltonian,

$$\hat{\mathcal{H}} = -\sum_{\langle \mathbf{ij}\rangle\sigma} t_{\mathrm{ij}} \left(\hat{c}^{\dagger}_{\mathbf{i}\sigma}\hat{c}_{\mathbf{j}\sigma} + \hat{c}^{\dagger}_{\mathbf{j}\sigma}\hat{c}_{\mathbf{i}\sigma}\right) - \mu \sum_{\mathbf{i}\,\sigma} n_{\mathbf{i}\,\sigma} + \frac{1}{2}\sum_{\mathbf{i}} \hat{p}^2_{\mathbf{i}} + \frac{1}{2} M\omega_0^2 \sum_{\mathbf{i}} \hat{x}^2_{\mathbf{i}} + \lambda \sum_{\mathbf{i}} \hat{x}_{\mathbf{i}}(\hat{n}_{\mathbf{i}\uparrow} + \hat{n}_{\mathbf{i}\downarrow}) \; . \tag{4.1}$$

Here the kinetic energy sum is over sites on a hexagonal lattice, with $t_{\rm ij} = t$ for pairs of sites internal to a set of hexagons, and $t_{\rm ij} = t'$ for pairs of sites bridging distinct hexagons. See Fig. 4.1. We will report lattice sizes N in terms of the number of hexagons, i.e. the unit cell count. Figure 4.1 corresponds to $N = (3 \times 3) \times 6 = 54$ sites. The remaining terms in $\hat{\mathcal{H}}$ consist of a collection of local quantum oscillators of frequency ω_0 ($\omega_0 = 1$ is used in all the simulations in this chapter) and an electron-phonon coupling λ of the fermionic charge density $\hat{n}_{\mathbf{i}\uparrow} + \hat{n}_{\mathbf{i}\downarrow}$ to the displacement $\hat{x}_i$. We will measure the strength of the coupling via the dimensionless combination $\lambda_D \equiv \lambda^2/(M\omega_0^2 W)$. In the anti-adiabatic limit $\omega_0 \to \infty$, the coupling λ_D can be thought of as the ratio of an effective attraction between electrons mediated by the phonons, $U_{\rm eff} = -\lambda^2/(M\omega_0^2)$, to the kinetic energy scale W. The choice $t = 1 + \Delta$ and $t' = 1 - 2\Delta$ keeps the bandwidth $W = 6$ fixed as Δ is varied, allowing us to study the effects of modulated hopping while keeping λ_D constant. We set the phonon mass $M = 1$ and tune the chemical potential $\mu = -\lambda^2/\omega_0^2$ to the particle-hole symmetry point so that the filling is always $\langle\, n_{\mathbf{i}\,\sigma}\,\rangle = \frac{1}{2}$.

We solve for the properties of Eq. 6.1 using two methods. The first is a mean field approach in which we make an *ansatz* for the phonon coordinates. (See Sec. 3.) The resulting Hamiltonian is quadratic in the remaining fermion degrees of freedom and can be solved analytically. The free energy is minimized within the parameter space allowed in the *ansatz*. The second approach is DQMC [**101**, **102**]. Unlike MFT, it solves the many-body problem exactly, on finite lattices. DQMC has statistical errors associated with the sampling, which are of the order of 0.1% for local quantities like the double occupancy and energy, but can be several percent for global quantities like structure factors in the vicinity of phase transitions. DQMC also has 'Trotter errors' [**103**–**106**] arising from the discretization of imaginary time. Because these Trotter errors are of the same order as, or smaller than, the statistical ones for the quantities we use in determining the phase boundary, we do not

perform any extrapolation in the imaginary time discretization. For all the work in this chapter we use $\Delta\tau = 0.1$.

Regardless of the value of Δ, the decorated honeycomb lattice is bipartite, and hence the local fermionic pairs which form due to the effective attractive interaction U_{eff} mediated by the phonons tend to form a charge density wave phase at half-filling. Previous investigations have determined the phase diagram in the λ_D-T plane for $t = t'$ [**1**, **2**]. For $\omega_0/t = 1$, there is a quantum critical point at $(\lambda_D)_c = 0.27$ above which CDW order forms in the ground state. T_c rises rapidly at $(\lambda_D)_c$, reaching a maximum value $T_c/t \sim 0.2$ at $\lambda_D \sim 0.5$. We are interested here in the effect of the nonuniform hoppings Δ on T_c and on $(\lambda_D)_c$. In the limits $\Delta = 0.5$ and $\Delta = -1$ the system separates into collections of independent hexagons and dimers, making long range order impossible and $T_c = 0$ trivially.

The two site unit cell of the honeycomb lattice is expanded by the decoration, so that now there are six bands. Figure 4.2 shows $E(\vec{k})$ for the undecorated honeycomb lattice $t = t'$ (central panel); the dimer limit $t < t'$ (top panel); and the hexagon limit $t' < t$ (bottom panel). In either case, the touching of the two bands at the Dirac cones which occurs at half-filling and $t = t'$ is replaced by a gap.

The associated densities of states (DOS) for the three cases are shown in Fig. 4.2 Right. Consistent with the dispersion relations of Fig. 4.2 Left, when $\Delta \neq 0$, the linearly vanishing DOS at $E = 0$ of the isotropic honeycomb lattice is replaced with a gap.

The decorated lattice geometry of Fig. 4.1 has been proposed as a generalization of the isotropic honeycomb lattice with a topological gap opened by the difference between the inter- and intra-plaquette hoppings [**80**]. The six resulting bands can be viewed as arising from the six single electron states ("orbitals") which exist on each independent ($t' = 0$) hexagon and whose degenerate levels are broadened when $t' \neq 0$. The topological nature is

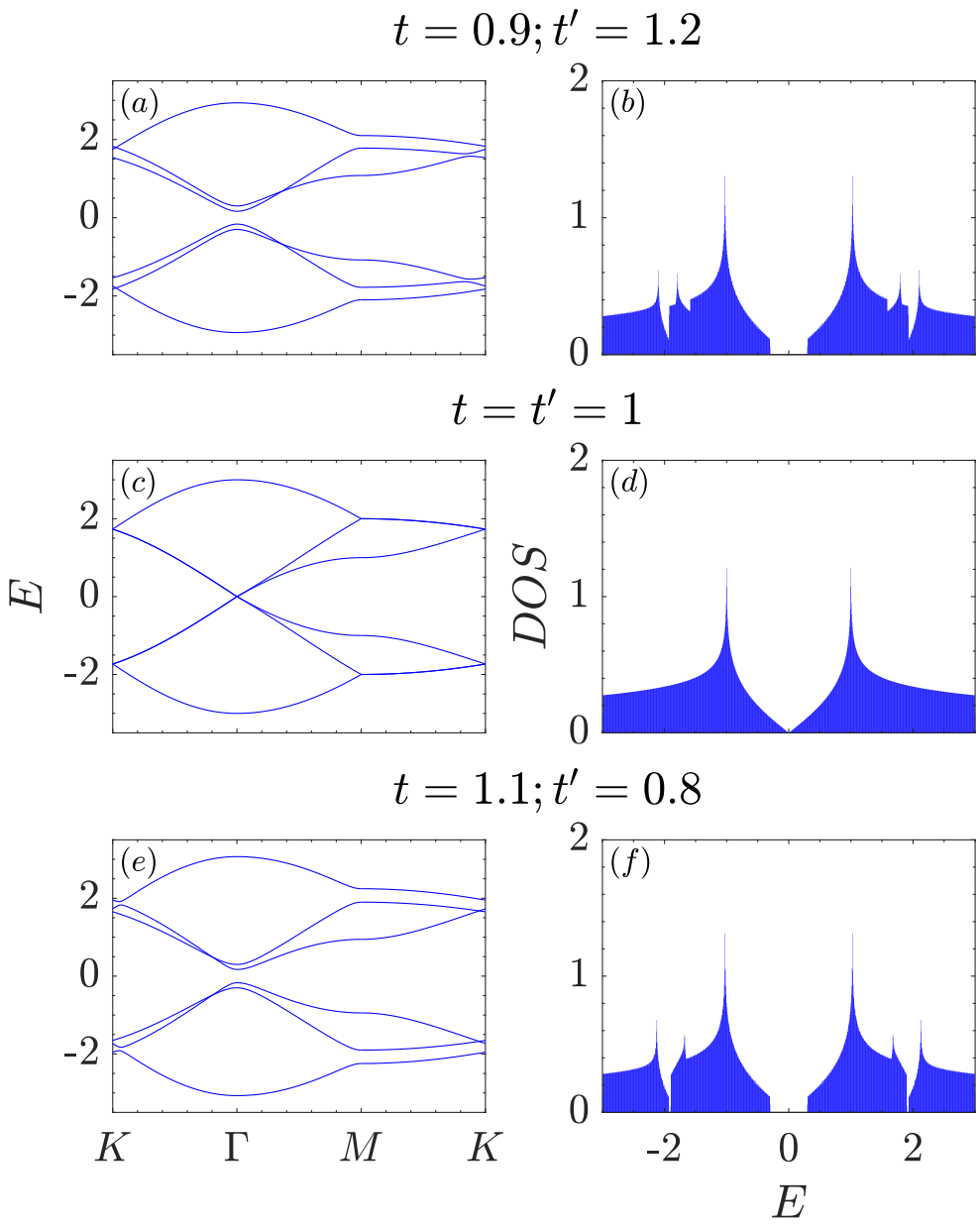

FIGURE 4.2. Left: Energy dispersion $E(\vec{k})$ in the noninteracting ($\lambda = 0$) limit. The Dirac points of the two bands of the honeycomb lattice, $t = t'$ (middle panel), are split by the decoration $t \neq t'$. In both cases, $t > t'$ and $t < t'$, a gap is opened at half-filling. See text for a discussion of differences at other fillings. Right: Density of states for the same three cases as left panel. A gap at half-filling is evident when $t \neq t'$.

not like that induced by spin-orbit coupling. Instead, it is similar to the 1D Su-Schrieffer-Heeger model, which also contains weak and strong bonds. Domain walls which arise from $t \neq t'$ are associated with a gapless boundary state.

Other versions of decoration exist. For example, Rüegg *etal* [**107**] have explored topological insulators of a tight-binding Hamiltonian with spin-orbit and Rashba interactions on a "star" lattice which interpolates between honeycomb and Kagomé geometries. Similarly, when honeycomb rhodates like Li_2RhO_3, are pressurized various bond dimerization patterns emerge on the Rh hexagons, and are associated with different magnetic patterns [**108**]. A final example is strained graphene, in which the hoppings t_1, t_2, t_3 along the three primitive lattice vectors are allowed to be unequal [**109**–**112**].

As noted in the introduction, in quantum spin-1/2 and itinerant electron Hamiltonians with repulsive interactions, unequal hoppings tend to degrade long range magnetic order. It is worth discussing the relation between those (spin) singlet phases and the disordered phases in the attractive Hubbard model, since that has a close connection to the Holstein model studied here; both exhibit CDW and superconducting phases and a quantitative link is provided by $U_{\rm eff} = -\lambda^2/\omega_0^2$.

4.3. Mean Field Theory Results

We first examine the physics of the Hamiltonian of Eq. 6.1 within mean field theory. In this approach, we ignore the phonon kinetic energy and assume a staggered pattern for the phonon displacements, $x_i = x_0 + (-1)^i\, x_1$. Here $(-1)^i = \pm 1$ on the two sublattices of the (bipartite) honeycomb geometry. The quadratic fermion Hamiltonian can be diagonalized, resulting in a total free energy per site which combines both electron and phonon contributions, $f(x_0, x_1, T) = N\,\omega_0^2\,(x_0^2 + x_1^2)/2 - T\,\sum_\alpha \ln\big(\,1 + e^{-\epsilon_\alpha(x_0,x_1)/T}\,\big)$, where ϵ_α are the fermion energy levels. A nonzero bond dimerization x_1 implies an associated charge modulation, since λx_i acts as a local chemical potential on site i.

The resulting phase diagram is shown in the top panel of Fig. 4.3. T_c is decreased by decoration, as might be expected from the Stoner criterion and the opening of a true gap (vanishing of the Fermi surface density of states in a finite chemical potential range). However, for $\lambda_D = \frac{2}{3}$, the effect is relatively small: Even in the extreme independent hexagon and dimer limits $T_c(\Delta = 0.5)/T_c(\Delta = 0) = 0.965$ and $T_c(\Delta = -1)/T_c(\Delta = 0) = 0.822$, respectively. The MFT T_c is nonzero even though there can be no symmetry breaking on small finite clusters. On the other hand, for smaller λ_D, MFT results indicate that a critical Δ is needed in order to have a CDW phase, which is consistent with the DQMC results in Fig. 4.7. We have verified that, for $\lambda_D > 0.24$, the MFT results shown for $(50\times50)\times6$ lattices change by less than the thickness of the lines if the lattice size is decreased to $(4 \times 4) \times 6$, an observation which aids in interpreting the DQMC results of the next section, which are necessarily on smaller lattices. At $\lambda_D < 0.24$, where T_c gets small and the CDW region is minute, finite size effects, unsurprisingly, become more pronounced.

It is interesting to contrast this with the behavior of the simplest model of CDW physics in this geometry, the classical lattice gas $E = \sum_{\langle ij \rangle} V_{ij} n_i n_j$. Here $n_i = 0, 1$ and we choose $V_{ij} = V_0(1 + \Delta)$ or $V_{ij} = V_0(1 - 2\Delta)$, with the same geometry and bond convention as in Fig. 4.1. The total coupling $\sum_j V_{ij}$ at each site i is independent of Δ, in analogy to fixing the bandwidth W. The transition temperature as a function of Δ is given in the bottom panel of Fig. 4.3. Within MFT, T_c is completely independent of Δ because T_c is only a function of the total, and invariant, $\sum_j V_{ij}$. The bottom panel of Fig. 4.3 also gives the exact T_c (obtained by Binder crossings of classical Monte Carlo simulations). The exact T_c does depend on Δ, and can be seen to vary by a factor of three from its $\Delta = 0$ value when $\Delta = -0.8$ or $\Delta = +0.4$, values which approach the decoupled hexagon and dimer limits. Unlike the MFT calculation, the exact T_c must vanish at $\Delta = -1$ and $\Delta = +0.5$, and the lattice consists of independent clusters.

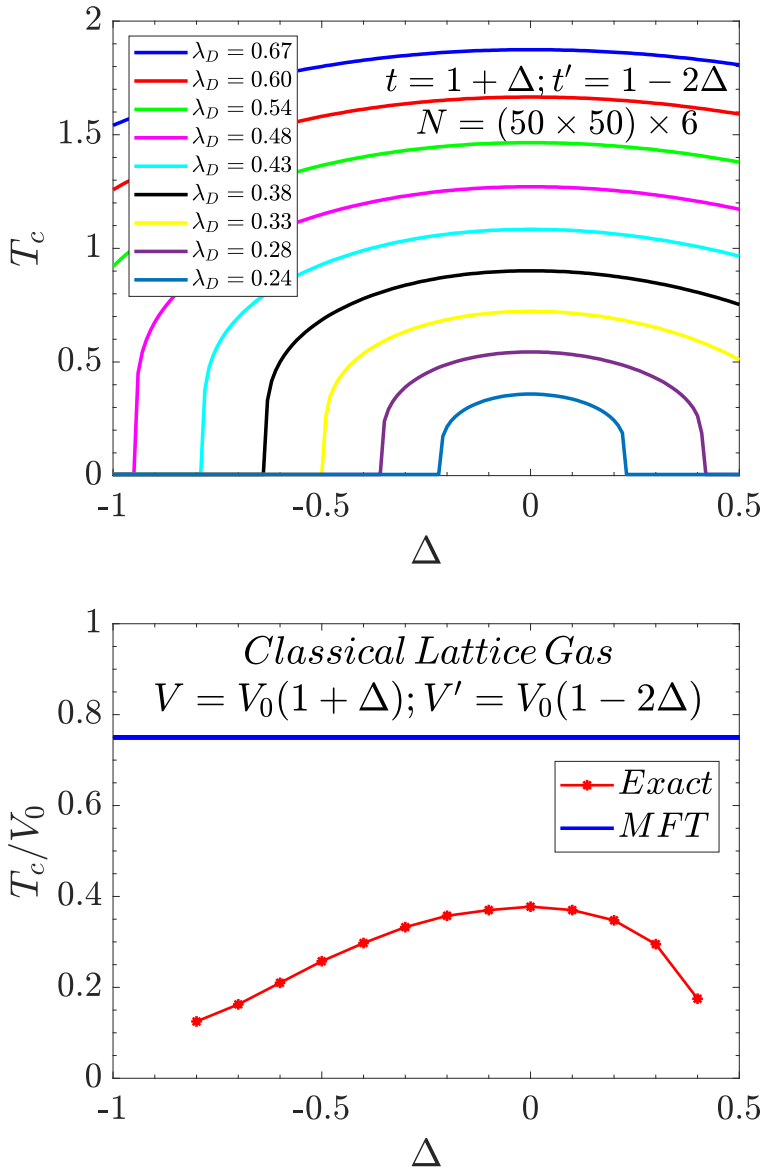

FIGURE 4.3. Top: Dependence of T_c on λ_D of the decorated Holstein model Eq. 6.1 within mean field theory. The CDW transition temperature is maximized for isotropic hopping ($\Delta = 0$), and is suppressed on the dimer side $\Delta < 0$ and the hexagon side ($\Delta > 0$). Bottom: Comparison of T_c given by MFT and classical Monte Carlo for a classical lattice gas. The difference between exact T_c and MFT T_c is more significant when Δ approaches to the limiting cases $\Delta = -1$ and $\Delta = 0.5$.

As we shall see in the following section, the MFT values for the critical temperature of Fig. 4.3(top) are an order of magnitude larger than those of QMC. This is perhaps not too surprising given the low dimensionality being studied. We note that a similar comparison of phase diagrams for the 2D Hubbard model revealed MFT in considerable disagreement with DQMC [**113**].

4.4. Quantum Monte Carlo Results

We now turn to the results of DQMC simulations which include fluctuations neglected in the preceding MFT treatment. We begin by showing the charge structure factor,

$$S_{\rm cdw} = \frac{1}{N} \sum_{i,j} (-1)^{i+j} \langle\, n_i n_j \,\rangle. \tag{4.2}$$

with $(-1)^{i+j} = \pm 1$ according to whether sites i, j are on the same or different sublattices. In an ordered phase, $T < T_c$, we expect $S_{\rm cdw}$ to grow linearly with the lattice size since $\langle\, n_i n_j \,\rangle$ is non-zero even for widely separated i, j pairs.

Figure 4.4 gives $S_{\rm cdw}$ for several values of λ_D and lattice sizes N at low temperature, $\beta = 10$. In a window about the isotropic Holstein limit ($\Delta = 0$), $S_{\rm cdw}$ is large and increases with lattice size, suggesting the presence of long range charge correlations for those values. Meanwhile, for large Δ, $S_{\rm cdw}$ is small and independent of size. Two quantum critical points (QCP) Δ_c separate the CDW from charge singlet regions at the two extremes of hopping difference $\Delta = -1.0$ and. $\Delta = 0.5$.

The difference

$$\mathcal{D} \equiv C_{\rm nn} - C'_{\rm nn} \equiv \langle\, n_i n_{i+\hat{x}} \rangle_t - \langle\, n_i n_{i+\hat{x}} \rangle_{t'} \tag{4.3}$$

between the near-neighbor density-density correlations $C_{\rm nn}$ on the t and t' bonds provides a measure of the effect of hopping difference on the order. For Δ small, $\mathcal{D}$ is small. $\mathcal{D}$ rises

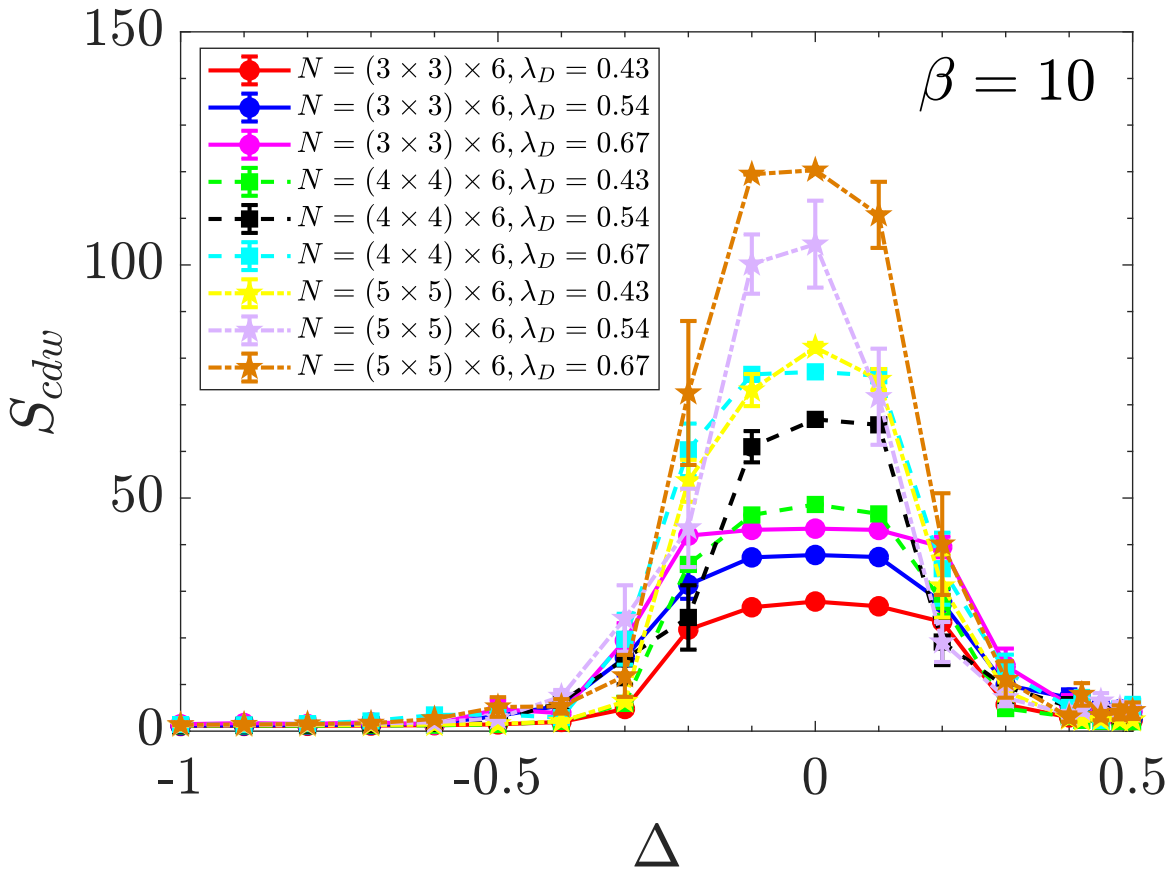

FIGURE 4.4. Charge structure factor $S_{\rm cdw}$ as a function of hopping difference Δ. There is a window near the isotropic point $\Delta = 0$ in which $S_{\rm cdw}$ is large and scales with system size, indicating long range charge order.

rapidly in the vicinity of the QCPs Δ_c. See Fig. 4.5. Indeed, $d\mathcal{D}/d\Delta$ can be regarded as a "inhomogeneity susceptibility" which diverges at $T = 0$ as $\Delta \to \Delta_c$.

Figures 4.4–4.5 focus on the low temperature charge correlations and identify the positions of the QCPs which bound the CDW regions near the isotropic lattice limit. Within the CDW, there is a finite temperature phase transition as T is decreased. Crossings of the scaled structure factor $S_{\rm cdw}/L^{\gamma/\nu}$ are shown in Fig. 4.6 and identify T_c in the region of small Δ where long range order persists.

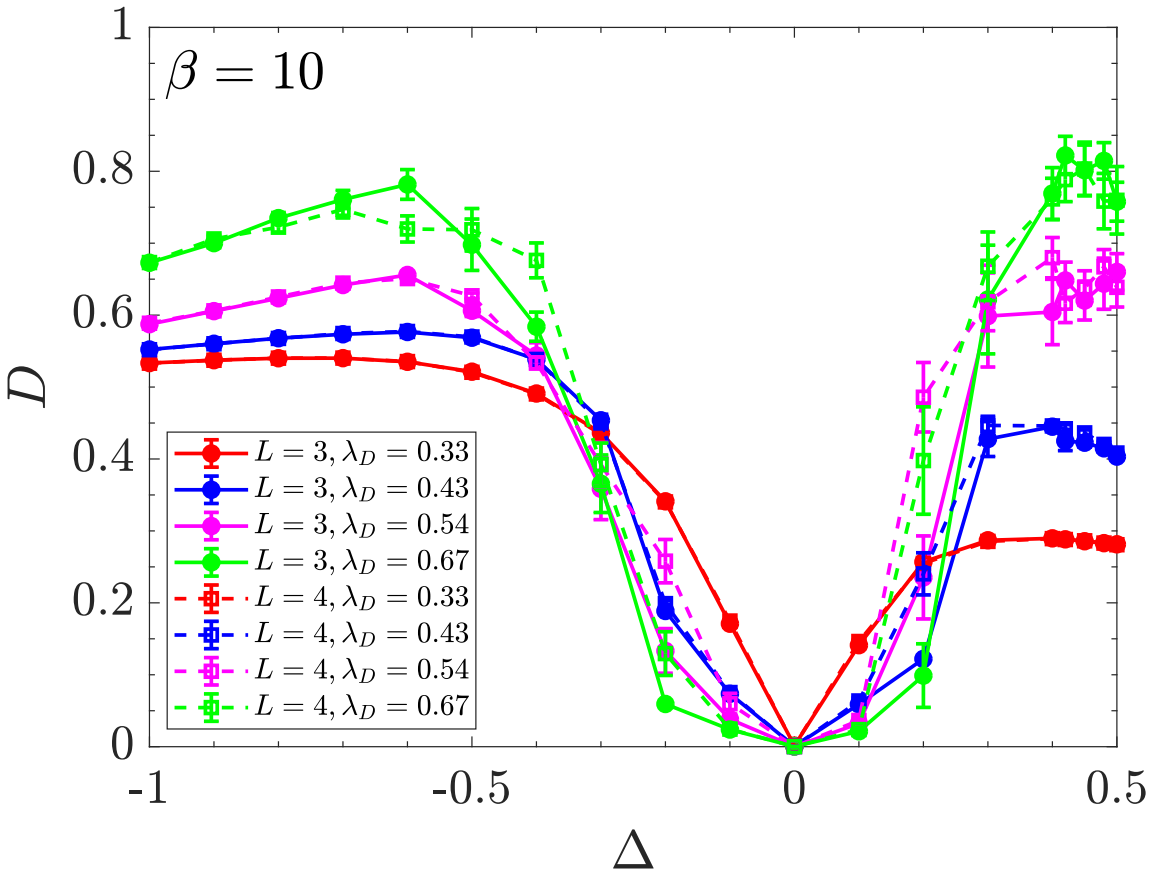

FIGURE 4.5. Difference $\mathcal{D}$ between density correlation function on t and t' bonds as a function of Δ. $\mathcal{D}$ rises steeply in the vicinity of the CDW to charge singlet QCP.

As discussed in the introduction, it seems natural to connect the loss of charge order in this electron-phonon model to analogous AF-singlet transitions in Hamiltonians describing quantum magnetism which have several exchange energy scales, e.g. the periodic Anderson and bilayer Hubbard Hamiltonians, and the bilayer or random bond Heisenberg Hamiltonians. We have used that language extensively in the present chapter, since it does constitute a useful touchstone. However, the fact that a finite temperature CDW transition occurs in the Holstein model suggests care should be taken in emphasizing this connection, since the continuous symmetry of the ordering direction forbids such a finite T transition in the 2D

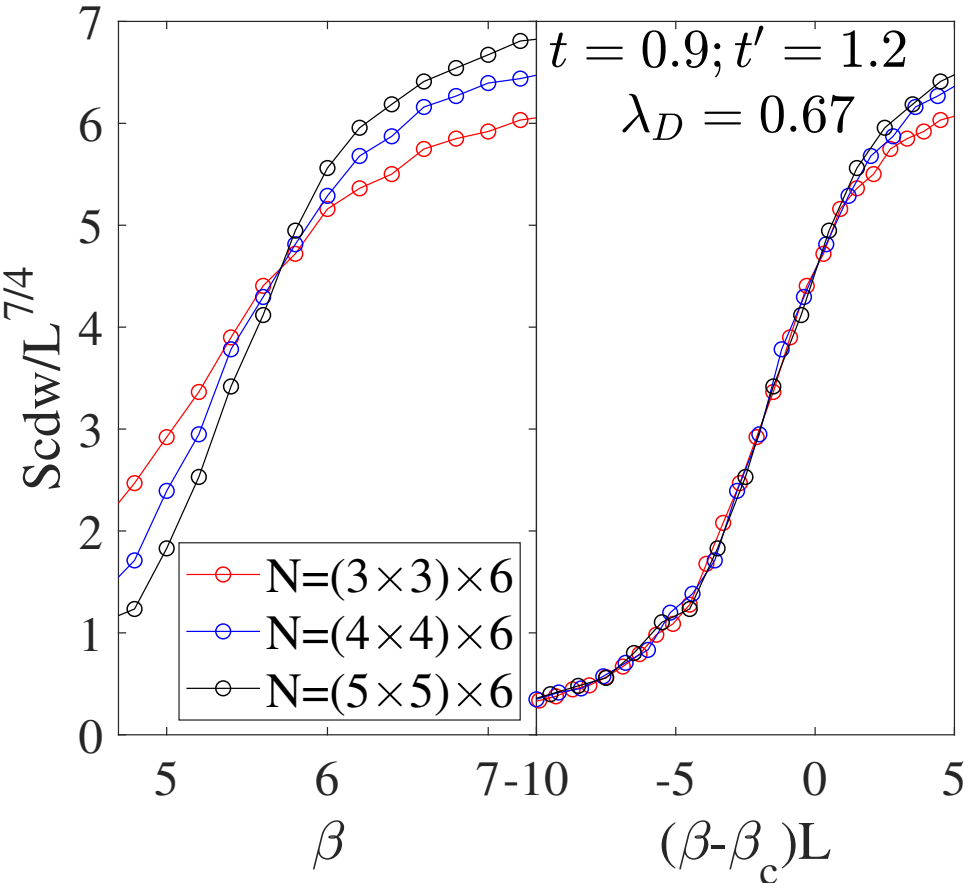

FIGURE 4.6. Scaled structure factor $S_{\rm cdw}/L^{\gamma/\nu}$ as a function of β. The scaling exponent $\gamma/\nu = 7/4$ is taken to be the 2D Ising value, and provides a good universal crossing. The crossing points identify $T_c = 1/\beta_c$.

magnetic models. Indeed, Figure 2.1 shows that the parameters explored in Figs. 4.4-4.6 are in fact very far from the regime where the analogy is precise.

Phase diagrams are obtained for fixed $\lambda_D = 0.48$, varying t and t' (top panel) and fixed $t = 0.9, t' = 1.2$, varying λ_D (bottom panel) in Fig. 4.7. It is numerically challenging to attempt to extract T_c when it becomes too small. Nevertheless, we can put reliable upper bounds on T_c by measuring $S_{\rm cdw}$ at large β and verifying its value is consistent with only short range charge correlations. Doing simulations at β up to $\beta = 25$ (temperature $T = 0.04$) strongly suggests that, similar to the undecorated honeycomb case [**1**, **2**], there is a nonzero

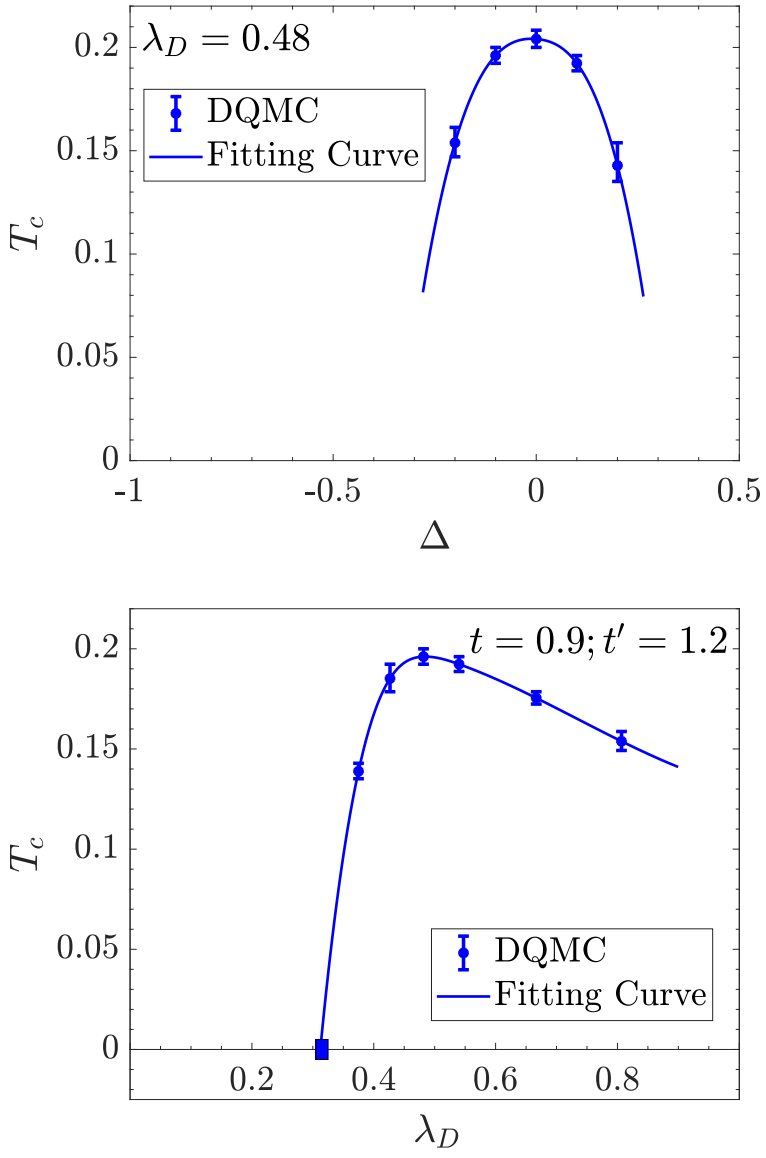

FIGURE 4.7. Top: Phase diagram of T_c as a function of Δ when $\lambda_D = 0.48$. T_c reaches its maximum for isotropic hopping ($\Delta = 0$), and drops sharply on the dimer side $\Delta < 0$ and the hexagon side ($\Delta > 0$). Bottom: Phase diagram of T_c as a function of λ_D when $t = 0.9, t' = 1.2$ with $(\lambda_D)_c \sim 0.32$. As λ_D grows, T_c increases first, as the electron-phonon coupling induces the CDW phase, but then decreases as large values of the electron-phonon coupling cause the polarons to become increasingly heavy [**1**, **2**]. The symbol along the horizontal axis of panel (b) is obtained by extrapolating the sharp descent of the DQMC data for T_c, combined with low temperature simulations which show the charge correlations are short ranged.

critical coupling $(\lambda_D)_c \sim 0.32$, for $t = 0.9, t' = 1.2$, as indicated along the $T = 0$ axis in the bottom panel, Fig. 4.7(bottom). Correspondingly, for fixed $\lambda_D = 0.48$, large β simulations suggest there are critical hopping differences Δ_c, as shown in the top panel, Fig. 4.7a. The presence of these QCP is further supported by their appearance in the MFT results in Fig. 4.3.

The fitting curves in Fig. 4.7 (top and bottom) are based on a simple cubic spline through the data and hence are best regarded as "guides to the eye". Since this is based on an *ad-hoc* functional form, there is considerable uncertainty in the positions of the QCPs which are seen in the MFT treatment (Fig. 4.3).

We conclude by examining the single particle spectral function, $A(\omega)$, which is related to the fermion Greens function $G(\tau)$ obtained in DQMC *via*,

$$G(\tau) = \int d\omega \frac{e^{-\omega\tau}}{e^{\beta\omega} + 1} A(\omega) \ . \tag{4.4}$$

$A(\omega)$ is the many-body analog of the single-particle density of states, and hence carries information concerning the opening of energy gaps in the excitation spectrum. We invert Eq. 5.2 via the maximum entropy method [**114**]. Fig. 4.8 gives $A(\omega)$ for two values of hopping difference on opposite sides of the CDW-charge singlet QCP. Despite the difference in the nature of the ground state, $A(\omega)$ vanishes at the Fermi surface $\omega = 0$ in both cases, as T is lowered. In the case of larger Δ, this reflects the presence of a charge singlet gap. In the case of smaller Δ, this is a CDW gap. Similar behavior occurs on the two sides of the antiferromagnetic-spin singlet QCP in the multiband Hubbard model [**115**].

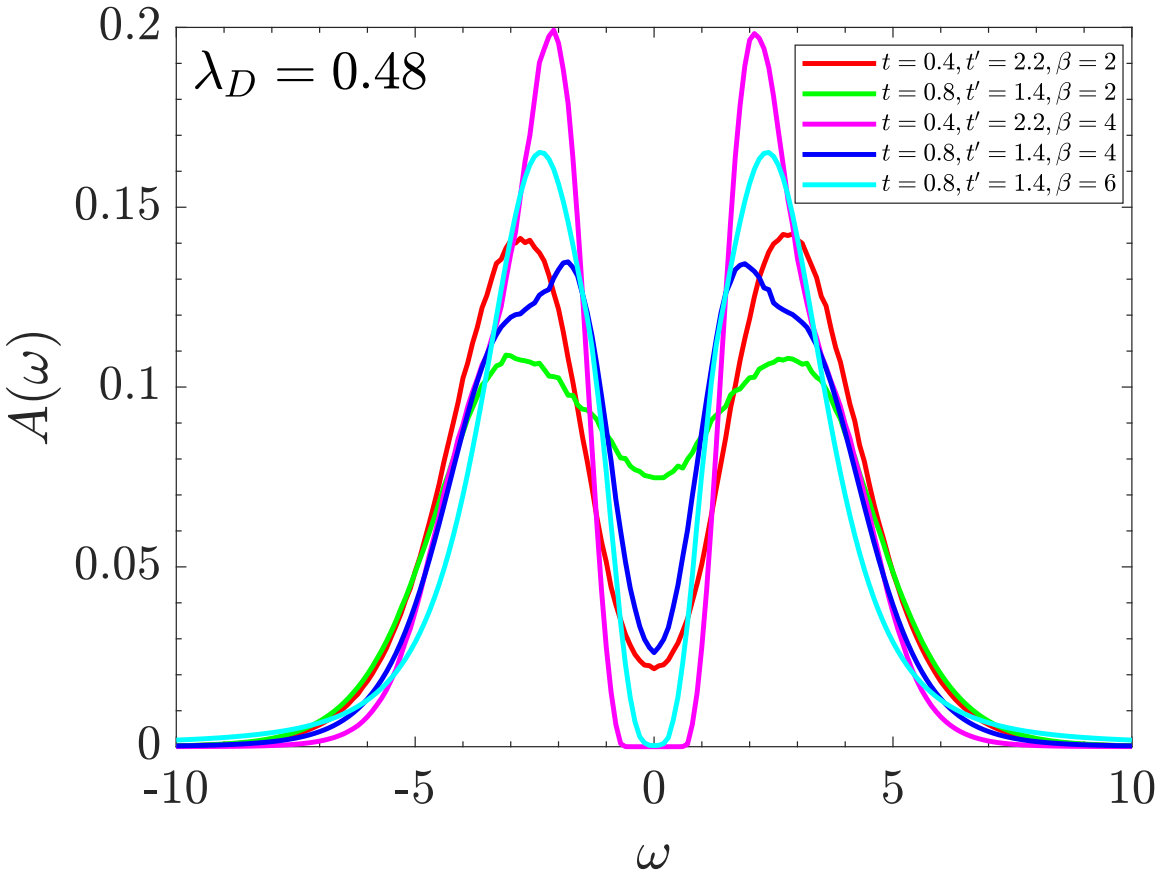

FIGURE 4.8. Spectral function for the two cases $\Delta = -0.6$ in the charge liquid phase and $\Delta = -0.2$ in the CDW phase.

CHAPTER 5

Interplay of flat electronic bands with Holstein phonons

5.1. Introduction

A number of periodic tight-binding lattices contain a macroscopic degeneracy of local, zero energy eigenstates which arise from the perfect cancellation of hopping for an appropriately phased occupation state [**31**, **32**]. These include the Kagomé, sawtooth, Creutz, diamond-octagon, square-octagon, decorated honeycomb, and finally the dice lattice, where the phenomenon was first noted [**116**]. One of the most prominent examples is the Lieb lattice, shown in Fig. 5.1, which is of special interest as the structure of the CuO_2 planes of the cuprate superconductors.

The existence of these 'compact localized states' is a property of the non-interacting system. Several years after their discovery, it was pointed out that precise statements can be made concerning the role of repulsive electron-electron interactions in flat band systems. Specifically, the existence of a ferrimagnetic ground state can be rigorously established [**33**]. Subsequent work further investigated flat band ferromagnetism [**34**–**37**]. The effect of attractive electron-electron interactions is also of interest [**117**–**120**], especially since the momentum at which Bose-Einstein condensation of fermionic pairs might occur is uncertain in a flat band [**121**–**123**].

Flat bands have also been considered within the context of the Fractional Quantum Hall Effect, [**124**] Chern insulating behavior, [**125**], Tomonaga-Luttinger liquids [**126**] and Haldane phases [**127**]. Perhaps the most dramatic explosion of theoretical and computational interest coincided with the recent discovery that bi-layer graphene, when twisted at a "magic angle" of about 1.1 degrees, displays unconventional superconductivity (SC) which is likely

closely linked to the appearance of a nearly dispersionless bands in the effective Moire pattern lattice [**128**–**133**]. This SC is characterized by a ratio of critical temperature to Fermi temperature higher than the cuprates.

In addition to realizations in these solid state materials, flat band physics has also been explored in photonic Lieb Lattices [**134**, **135**], and optical Lieb [**136**, **137**], Kagomé [**138**] and honeycomb [**139**] lattices.

Here, we investigate the phases of interacting *electron-phonon* systems for flat electronic bands [**38**]. Specifically, we study the Holstein Hamiltonian on a Lieb lattice. Although there are suggestive analogies between the Holstein model and the attractive Hubbard model, the former has a non-trivial frequency dependent coupling which distinguishes the two situations, the most significant consequence of which is the presence of a finite temperature phase transition even on 2D lattices which are the most commonly investigated flat band geometries. It is only in the extreme anti-adiabatic limit, where the phonon frequency is one to two orders of magnitude larger than the electronic bandwidth, that the Holstein and attractive Hubbard models become quantitatively equivalent [**10**].

5.2. Holstein Model

The Holstein model [**75**] has been introduced in Chapter 2. The electronic density of states in the absence of the electron-phonon interactions, is given in Fig. 5.2. The $\delta-$function spike at $E = 0$ reflects the macroscopic degenerate collection of local $E = 0$ vectors $|\psi\rangle$ constructed by forming a state with equal amplitude, and with the indicated phases, on four sites surrounding any vacant site the Lieb lattice. See Fig. 5.1. All these $|\psi\rangle$ have the property $\hat{\mathcal{K}}|\psi\rangle = 0$. where $\hat{\mathcal{K}}$ is the first (hopping) term in Eq. 6.1. The band structure is given in Fig. 5.3

When $\lambda \neq 0$, the qualitative physics of the Holstein model is as follows: at low densities individual electrons distort the lattice sites in their vicinity. The resulting composite particle, a 'polaron', possesses an increased effective mass, reflecting the fact that when the electron

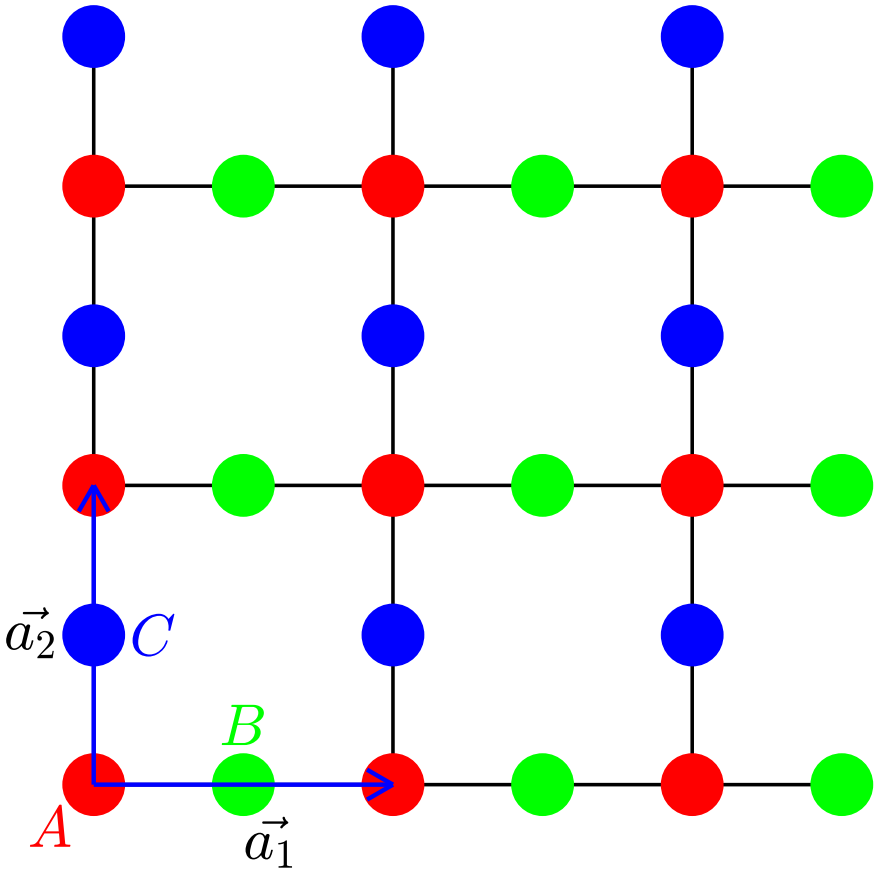

FIGURE 5.1. The Lieb lattice geometry. Additional sites (blue and green) are added to midpoint of each of the bonds linking the sites of a square lattice (red). The resulting structure is bipartite and has three sites per unit cell. Note especially that the red sublattice contains only half as many sites as the sublattice comprised of blue and green sites. The $\pm$ pattern on on the four blue/green sites surrounding one of the vacancies illustrates a zero energy mode. See text.

hops between sites, the oscillator degrees of freedom must reconfigure themselves [**140**–**144**]. These dressed quasiparticles tend to attract one another, since the distortion caused by one provides a favorable environment for another. Indeed, solving the $t = 0$ Holstein model one can see an effective attraction $U_{\rm eff} = -\lambda^2/\omega_0^2$ exists between spin up and down fermions. This independent site form is consistent with the interaction between electrons mediated by a phonon propagator, $V_{\rm eff}(\omega) = \lambda^2/(\,\omega^2 - \omega_0^2\,)$, if one sets $\omega = 0$.

The pairs of up and down electrons which arise from this attraction can participate in ordered phases. One possibility, which dominates on half-filled ($n_{\mathbf{i},\sigma} = 1/2$) bipartite lattices with equal number of sites in the two sublattices, such as square and honeycomb geometries, is a CDW arrangement in which pairs occupy one of the two sublattices. CDW formation is energetically favorable because, by surrounding itself with empty sites, a pair of electrons has the optimal ability for virtual hopping processes to adjacent sites, thereby lowering its energy by $J \sim -zt^2/U_{\text{eff}}$ where z is the coordination number. This situation is similar to that giving rise to antiferromagnetic order in the half-filled repulsive Hubbard model.

Another possible ordered state occurs when the pairs condense into a superconducting phase. This is expected to occur when the system is doped away from fillings which favor CDW order and has been studied with, for example, Eliashberg theory [**145**–**149**]. QMC simulations have given indications of pairing as well [**8**, **16**, **150**].

In this chapter, we consider the CDW transition in the Holstein model on the Lieb lattice. We set the phonon frequency $\omega_0/t = 1$ to facilitate comparisons with most of the existing QMC literature [**1**, **2**, **8**, **11**, **39**, **77**, **150**–**153**]. This historical choice was in part made as a simple starting point to explore the qualitative physics of the CDW and SC transitions, but also because it facilitated the DQMC simulations, which were known to exhibit long autocorrelation times at $\omega_0/t \lesssim 1/2$. Recent algorithmic improvements have made possible the study of smaller ω_0 [**22**, **154**–**157**].

5.3. Computational Methodologies

Mean field theory method discussed in Chapter 2 will be applied to study the Holstein model on a Lieb lattice. Although much insight can be gleaned from MFT, especially concerning the possible types of order, it has a number of well-understood defects, especially an overestimate of the tendency to long range order arising from ignoring fluctuations. This is particularly evident in lattice models like the Hubbard and Holstein Hamiltonians where it fails to distinguish two separate energy scales. The first is the temperature $T \sim U$ at

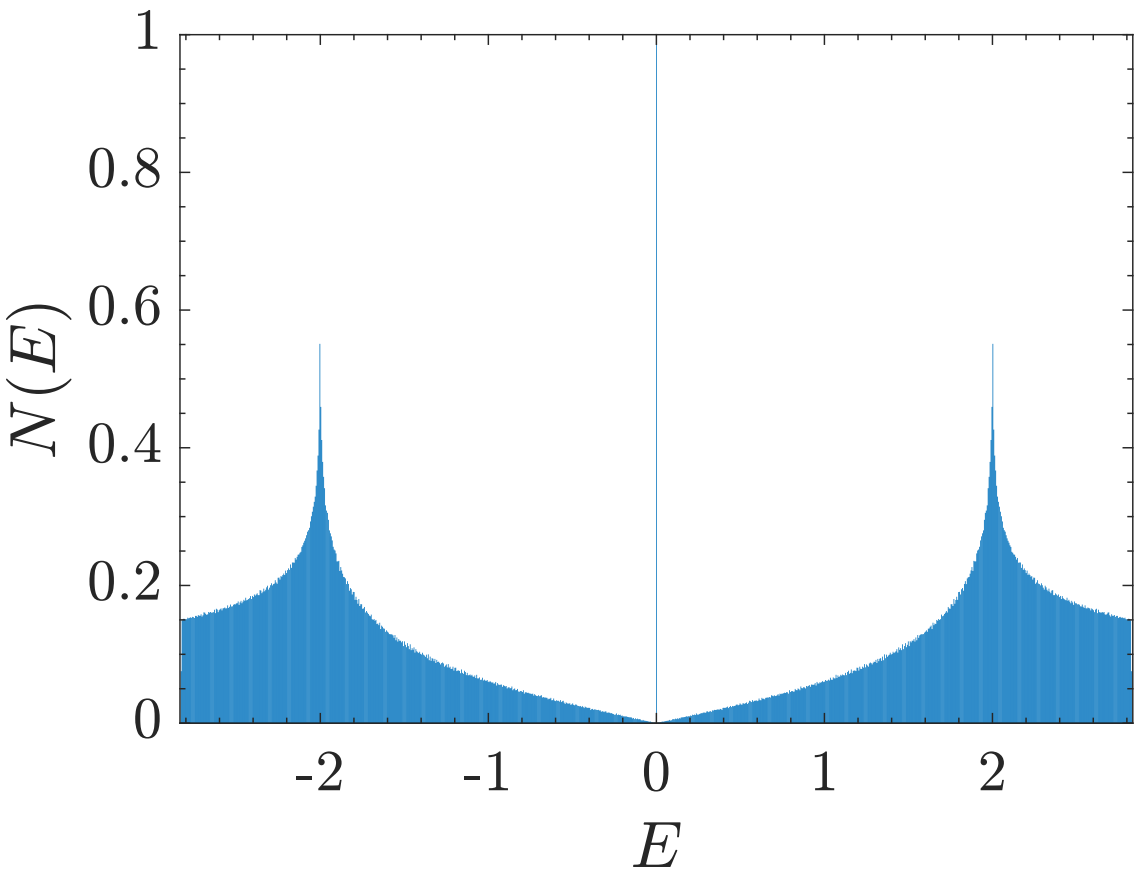

FIGURE 5.2. The density of states of the Lieb lattice. Energy levels of two dispersing bands bracket the δ-function peak at $E = 0$. Particle-hole symmetry is reflected in the property that $N(E) = N(-E)$.

which local moments (in the case of repulsive interactions) or pairs (in the case of attractive interactions) form. The second is the temperature at which inter-site ordering occurs. Since the former grows linearly with the interaction strength U, and the latter falls as $1/U$, MFT overestimates T_c by a far wider margin at strong coupling than in simpler classical descriptions of long range order such as the Ising model.

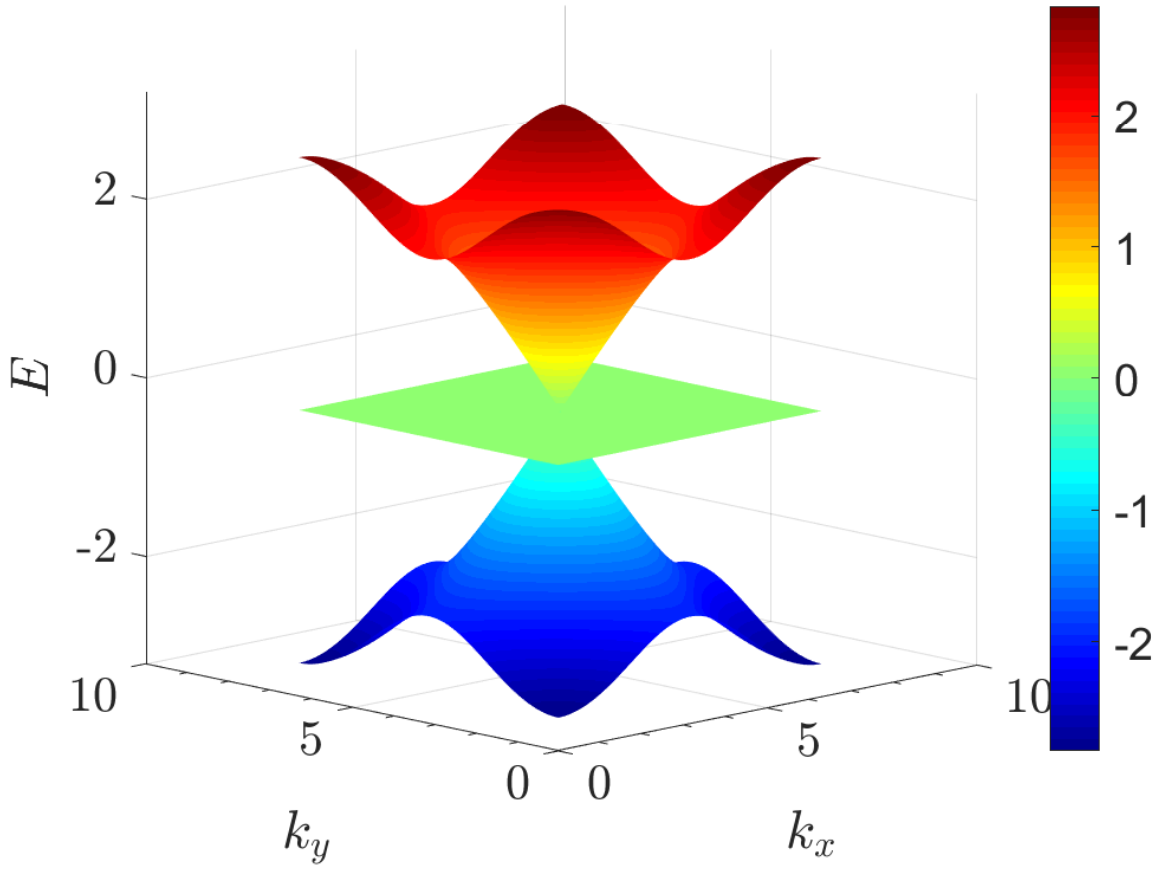

FIGURE 5.3. The band structure of the Lieb lattice.

To provide a more accurate treatment of the electron-phonon correlations, we turn to the use of the Determinant Quantum Monte Carlo (DQMC) methodology [**101**, **158**]. Simulations are carried out on lattices of finite size, necessitating a finite size scaling analysis, as described below.

We focus on several local observables, the density $\rho = \langle \hat{n}_{\mathbf{i}} \rangle$ and double occupancy $\mathcal{D} = \langle \hat{n}_{\mathbf{i}\uparrow} \hat{n}_{\mathbf{i}\downarrow} \rangle$, and on the CDW structure factor, the Fourier transform of the real-space density-density correlation function.

$$S(\mathbf{q}) = \sum_{\mathbf{r}} c(\mathbf{r})\, ^{i\mathbf{q}\cdot\mathbf{r}}$$
$$c(\mathbf{r}) = \langle\, \Delta\hat{n}_{\mathbf{i}+\mathbf{r}}\, \Delta\hat{n}_{\mathbf{i}}\, \rangle\ , \tag{5.1}$$

where $\Delta\hat{n}_{\mathbf{i}} = \hat{n}_{\mathbf{i},B} + \hat{n}_{\mathbf{i},C} - 2\hat{n}_{\mathbf{i},A}$ is the charge density difference within a unit cell, labeled by $\mathbf{i}$. When only the A or B/C sublattice is occupied, corresponding to one-third or two-thirds filling, the dominant $S(\mathbf{q})$ will be $S_{\text{cdw}} = S(\pi, \pi)$.

The spectral function $A(r, \omega)$ is obtained by an analytic continuation of the non-equal time Greens function

$$G(\mathbf{r}, \tau) = \langle\, \hat{c}_{\mathbf{i}+\mathbf{r},\sigma}(\tau)\hat{c}_{\mathbf{i},\sigma}(0)\, \rangle$$
$$= \langle\, e^{\tau\hat{\mathcal{H}}}\hat{c}_{\mathbf{i}+\mathbf{r},\sigma}(0)e^{-\tau\hat{\mathcal{H}}}\hat{c}_{\mathbf{i},\sigma}(0)\, \rangle$$
$$G(\mathbf{r}, \tau) = \int d\omega A(\mathbf{r}, \omega)\frac{e^{-\omega\tau}}{e^{\beta\omega} + 1} \tag{5.2}$$

We report the Fourier transform of the spectral function at zero momentum, a quantity which is the analog of the non-interacting density of states in a correlated system.

DQMC has been used to explore various properties of the attractive and repulsive Hubbard models on the Lieb Lattice [**123**, **159**, **160**], but has not yet been used for the Holstein model.

5.4. Results

5.4.1. Mean Field Theory

We first explore the effect of electron phonon interaction by using the mean field theory approach described in section 3A. Since the $\lambda x_{\mathbf{i}} n_{\mathbf{i}}$ term in the mean field Holstein Hamiltonian

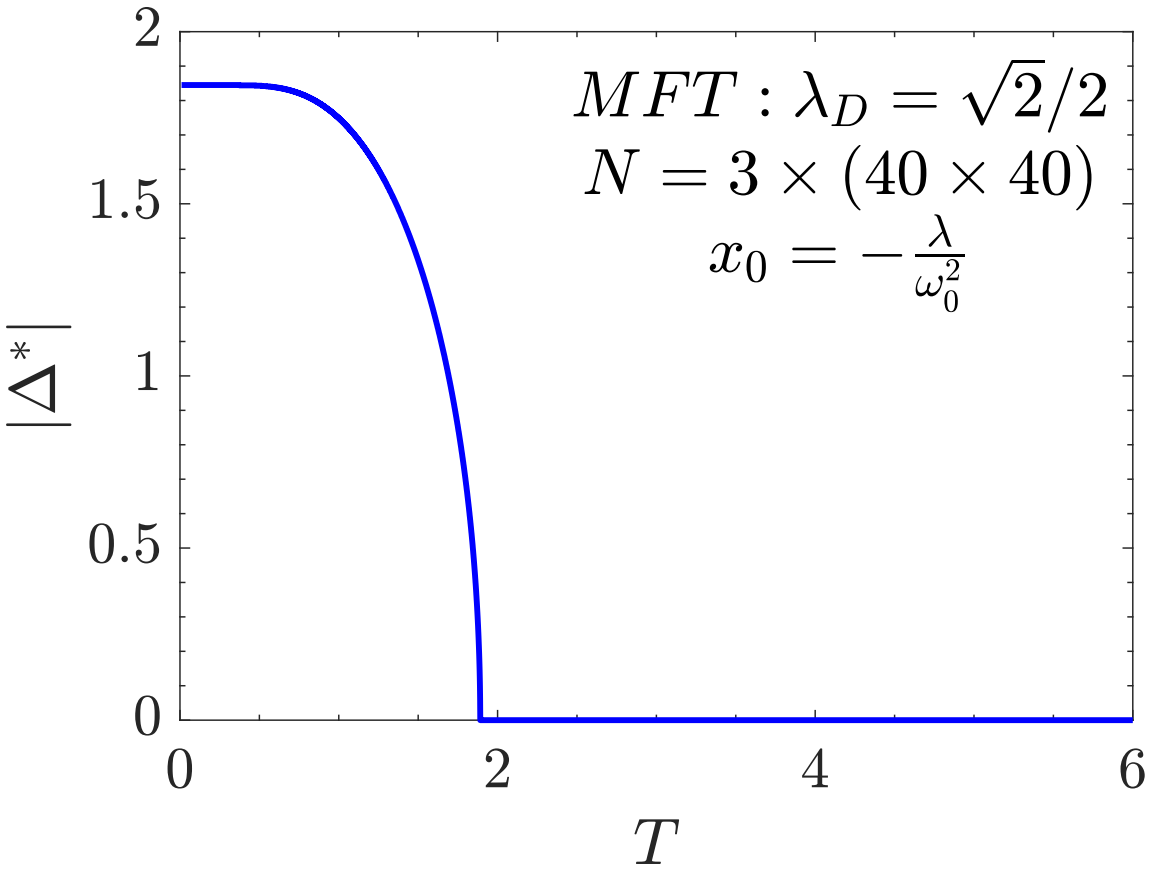

FIGURE 5.4. Mean field order parameter Δ^* as a function of temperature T/t at half-filling, $\mu = -\frac{\lambda^2}{\omega_0^2} = -4$. For $T > T_c \sim 1.9\,t$, the MFT critical temperature, $\Delta^* = 0$ and each site has $\rho_{\mathbf{i}} = 1/2$. For $T < T_c$ there are two degenerate values of $\Delta = \pm\Delta^*$ which minimize $\mathcal{F}$. These correspond to $1/2 - d\rho$ and $1/2 + d\rho$ (and hence the *average* density is half-filled), with $d\rho$ gradually growing to $1/6$ as T decreases (corresponding to 1/3 and 2/3 filling).

can be viewed as a chemical potential $\lambda x_{\mathbf{i}}$ acting on site $\mathbf{i}$, a nonzero bond dimerization Δ implies a staggered pattern of electron density, i.e. a CDW phase. We first fix $x_0 = -\frac{\lambda}{\omega_0^2}$ so that the lattice is half filled. For $T > T_c \sim 1.9t$, the order parameter $\Delta = 0$ minimizes $\mathcal{F}$. Below T_c, we find there is a pair of degenerate solutions $\Delta = \pm\Delta^*$, corresponding the equal weights of $1/2 - d\rho$ and $1/2 + d\rho$,with $d\rho$ gradually growing to $1/6$ as temperature T is lowered (corresponding to 1/3 and 2/3 filling). Δ^* is plotted as a function of temperature

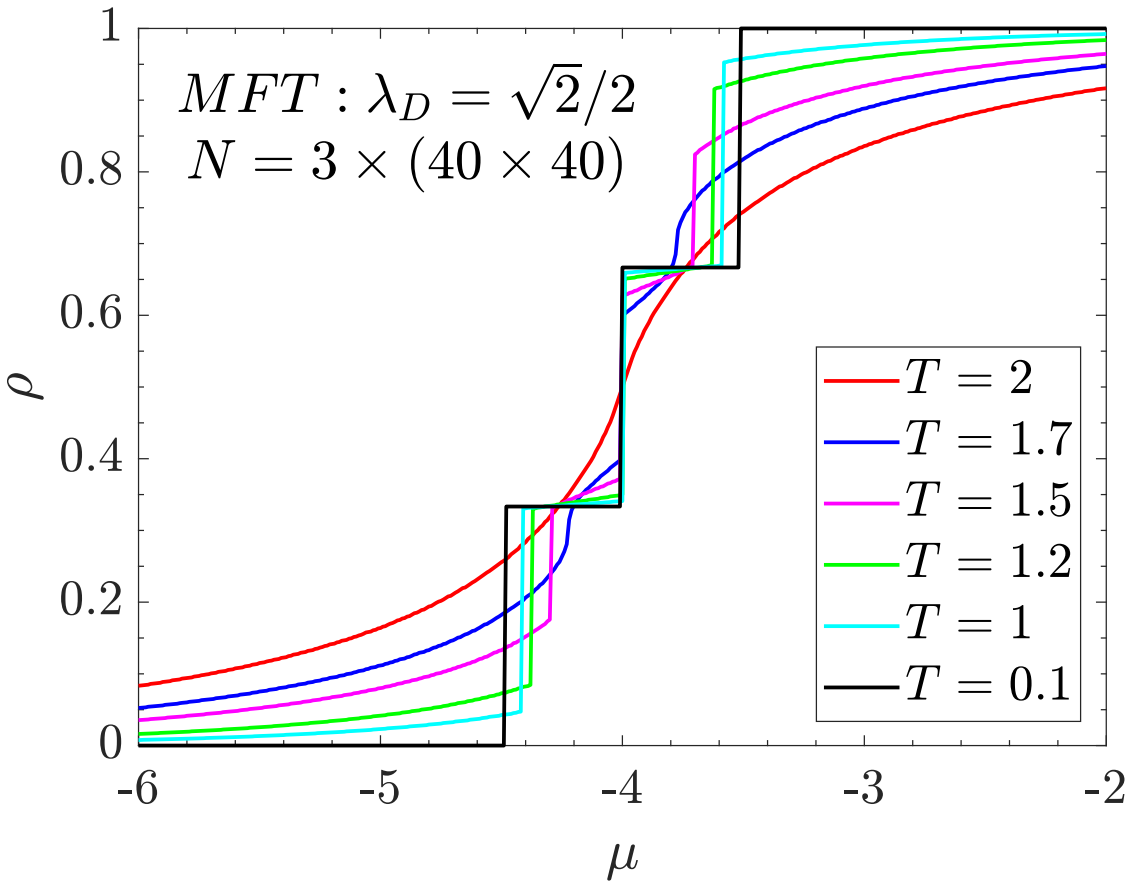

FIGURE 5.5. Density ρ as a function of chemical potential μ within MFT. Temperature $T = 2\,t > T_c$ and $\rho(\mu)$ is smooth. For temperature $T = t < T_c$ the density $\rho(\mu)$ has plateaus at $\rho = 1/3, 2/3$ corresponding the a non-zero CDW gap. The sublatttice occupations are given by $\rho_A = 1/2 + \Delta^*$ and $\rho_{B/C} = 1/2 - \Delta^*$ so that when $\Delta^* > 0$ there is a smaller number of A sites with $\rho > 1/2$ and a larger number of B/C sites with $\rho < 1/2$ and the total density $\rho = 1/3$, and vice-versa for $\Delta^* > 0$.

T in Fig. 5.4. All MFT results presented in this chapter are obtained on a $3 \times (40 \times 40)$ Lieb lattice with a dimensionless electron phonon coupling constant $\lambda_D \equiv \frac{\lambda^2}{\omega_0^2 W} = \sqrt{2}/2$. Here $W = 4\sqrt{2}t$ is the fermion band width for a Lieb lattice in the noninteracting limit. We will see later the MFT $T_c \sim 1.9\,t$ is more than an order of magnitude higher than the T_c given by DQMC.

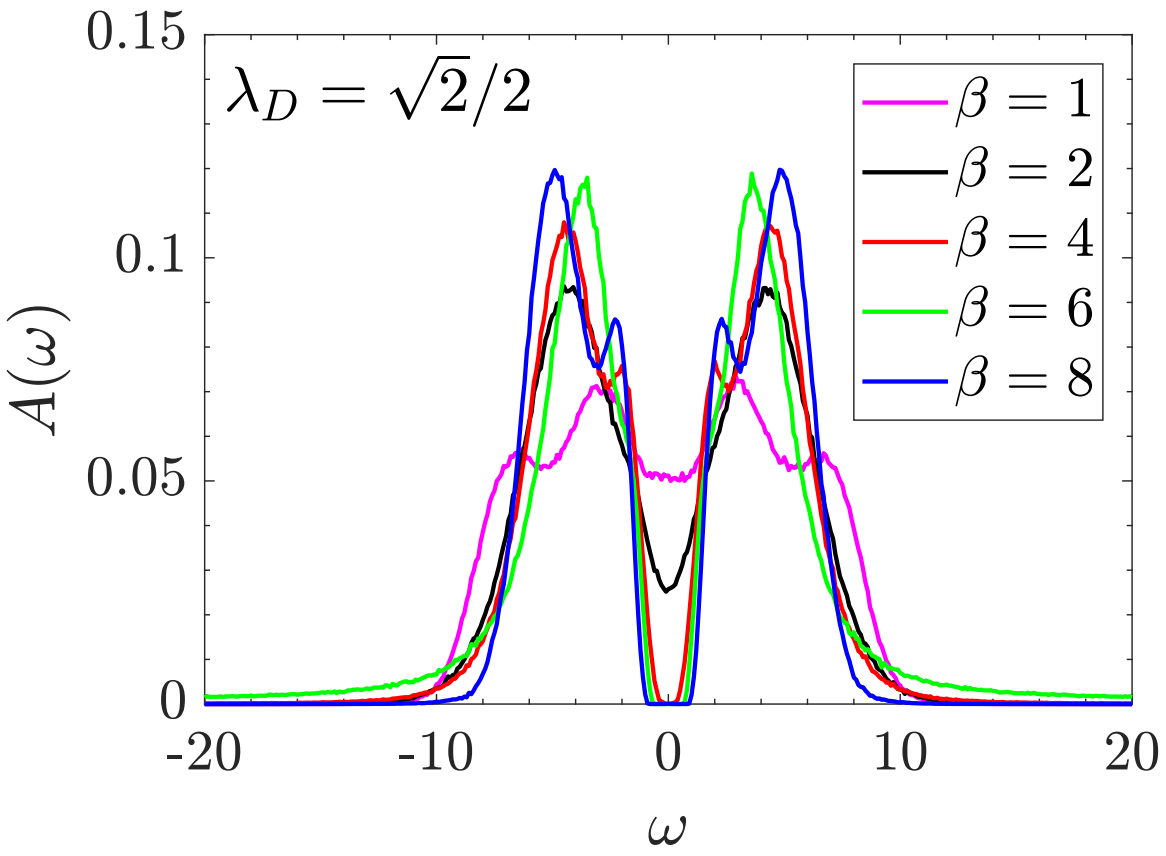

FIGURE 5.6. The spectral function $A(\omega)$ determined in DQMC calculations. A gap opens at the Fermi surface $\omega = 0$ as the temperature is lowered (β increases). This provides a rough estimate of T_c.

For different chemical potential μ, we follow the same steps to determine (x_0^*, Δ^*) minimizing the free energy and find $\Delta^* > 0$ ($\rho = 1/3$ CDW pattern) when $\mu < -\frac{\lambda^2}{\omega_0^2}$; $\Delta^* < 0$ ($\rho = 2/3$ CDW pattern) when $\mu > -\frac{\lambda^2}{\omega_0^2}$. The electron density can be obtained by $n = \sum_{\alpha,\mathbf{k}} \frac{1}{1+e^{\beta\epsilon_\alpha}}$. Figure 5.5 shows the density ρ as a function of chemical potential μ. As temperature is lowered, plateaus at $\rho = 1/3$ and $\rho = 2/3$ develop, indicating that a 1/3 filling CDW pattern and its partner at 2/3 filling, extend over a finite range of μ, which is consistent with the DQMC results below. A similar phenomenon is also observed in the '$t-V$ model' of spinless fermions interacting with a nearest neighbor repulsion on a Lieb lattice. [**161**].

5.4.2. Determinant Quantum Monte Carlo

We now turn to DQMC results. We begin with the spectral function in Fig. 5.6. At high temperatures (small β) $A(\omega = 0)$ is non-zero. A gap is fully formed at $\beta_c t \sim 6$, suggesting a transition to an insulating CDW phase.

A more accurate determination of the location of the CDW transition is obtained by a finite size scaling analysis of $S_{\rm cdw}$. Because the low temperature phase involves occupying one of two spatial sublattices, it breaks a $\mathcal{Z}_2$ symmetry, and therefore the transition should be in the Ising universality class. Using the known 2D Ising critical exponents $\nu = 1$ and $\gamma/\nu = 7/4$ yields the finite size scaling plots of Fig.5.7. We find $\beta_c t = 6.4 \pm 0.1$. If we eschew this knowledge and instead vary the critical exponents and minimize the scatter of the data collapse plot, the resulting γ/ν is within 5% of the 2D Ising value. An example of such an analysis (for the honeycomb lattice) is given in [**1**].

The real space density correlations $c(\mathbf{r})$ provide additional insight into the nature of the CDW order. Figures 5.8 and 5.9 give color intensity plots of $c(\mathbf{r})$ for different temperatures and initializations of the phonon displacement $x(\mathbf{i}, \tau)$. At high temperatures, the correlations are independent of the starting configuration and $c(\mathbf{r}) = \langle n_{\mathbf{i}+\mathbf{r}} n_{\mathbf{i}} \rangle = \langle n_{\mathbf{i}+\mathbf{r}} \rangle \langle n_{\mathbf{i}} \rangle \sim 1$. Short range correlations begin to develop at $\beta t \sim 6$ and a strong alternation between $c(\mathbf{r}) \sim 4$, where $\mathbf{r}$ connects a pair of doubly occupied sites, and $c(\mathbf{r}) \sim 0$, where one of the sites is empty, becomes apparent. In the case of the initialization in the $\rho = 1/3$ state (Fig. 5.8) with only sublattice A sites occupied, density correlations referenced to an A site (top panel) show the alternation, whereas if referenced to an unoccupied B site (bottom panel) all $c(\mathbf{r})$ become small. Conversely, for initialization in the $\rho = 2/3$ state (Fig. 5.9) with sublattice B,C sites occupied, density correlations referenced to a B site (bottom panel) show the alternation, whereas if referenced to an unoccupied A site (top panel) all $c(\mathbf{r})$ become small.

Another way to examine the evolution into one of two possible ground states, characterized by distinct densities, is to begin several simulations with constant density $\rho = 1$, and

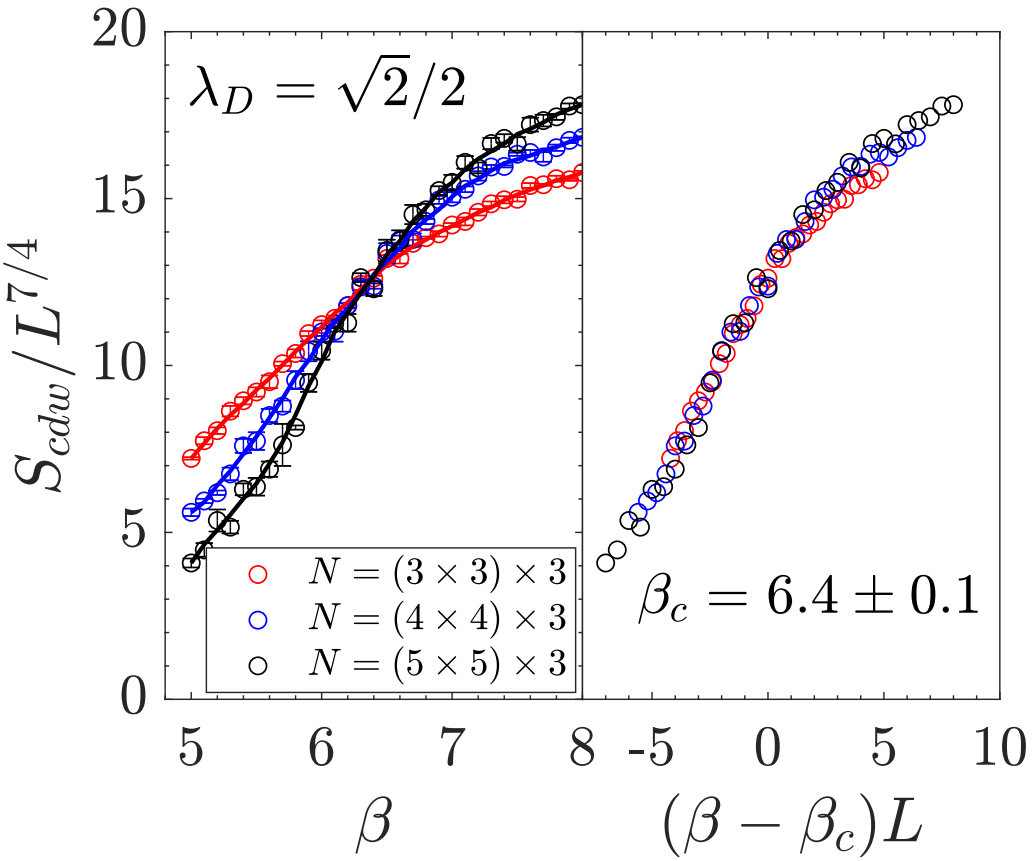

FIGURE 5.7. Left: The scaled structure factor is plotted versus β for three lattice sizes. The crossing gives the position of the CDW transition. Right: If the horizontal (inverse temperature) axis is also scaled, a full data collapse is obtained.

examine the final densities achieved. Figure 5.10 shows the result for four such simulations. At small β the lattice remains half-filled, but as β increases the lattice falls into either the $\rho = 1/3$ or the $\rho = 2/3$ minimum. The tendency for this splitting begins about $\beta \sim 5$. For $5 \lesssim \beta \lesssim 9$ the data tend to fill the region between the upper and lower densities. This happens because at finite temperatures and on finite lattices, tunneling between the two minima can occur in the course of a simulation. Depending on the relative amount of time spent at $\rho = 1/3$ and $\rho = 2/3$, the average density can take different values. For $\beta \gtrsim 9$ very little tunneling occurs, and the data instead lie on just one of the two bounding lines. Note

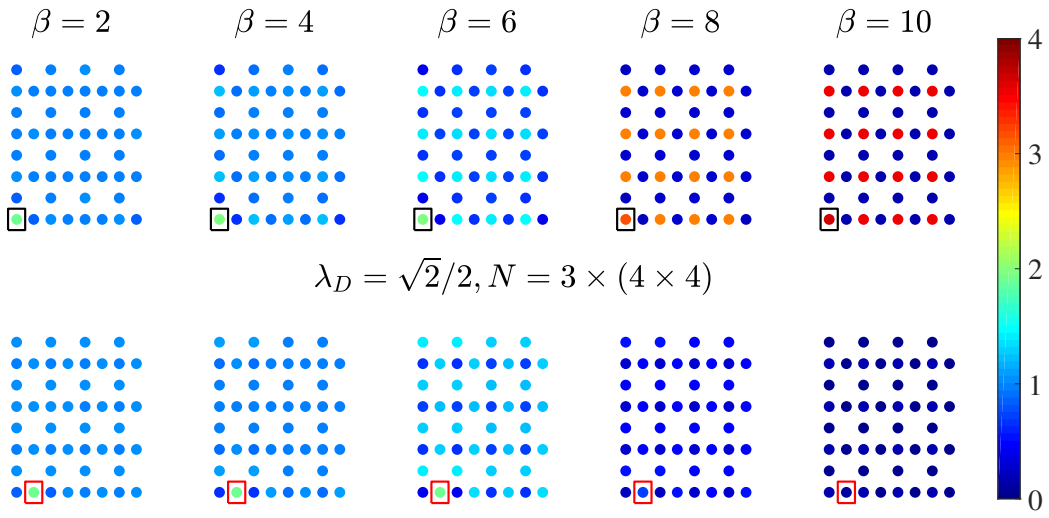

FIGURE 5.8. Density-density correlation for a $3 \times (4 \times 4)$ Lieb lattice at $\omega_0 = 1, \lambda = 2(\lambda_D = \sqrt{2}/2)$. The simulation was initialized with HS field appropriate to being in the $\rho = 1/3$ minimum with dominant A sublattice ('Copper sites') occupation. First row: correlations between each site and the Cu site in the bottom left unit cell. Second row: correlations between each site and the B/C sublattice ('Oxygen sites') in the bottom left unit cell.

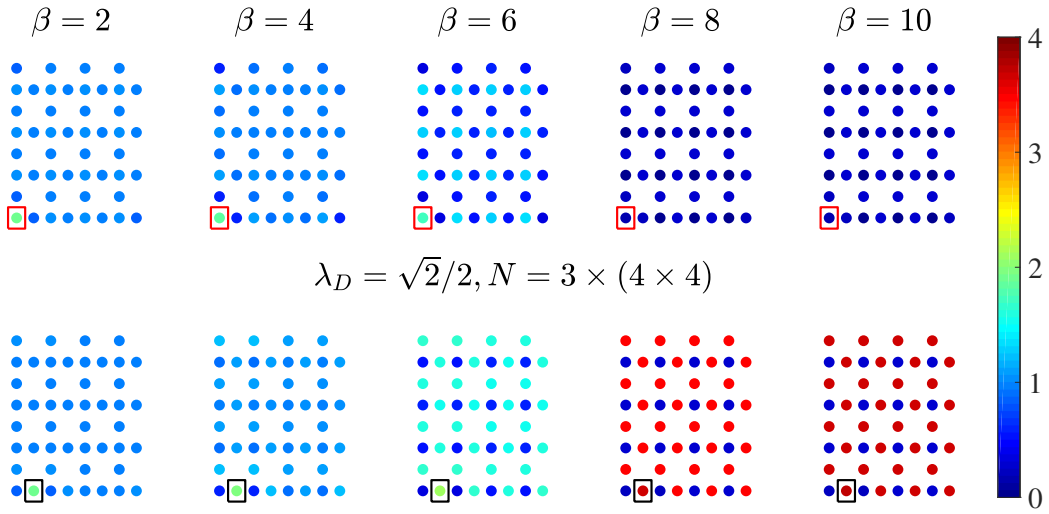

FIGURE 5.9. Same as Fig. 5.8 except starting in the $\rho = 2/3$ minimum.

that the order parameter depends on β so that the increasing width of the ρ curves reflects the growth of the CDW order parameter below β_c.

It is important to emphasize a subtlety of the physics. Although the simulations of Fig. 5.10 were done at the chemical potential $\mu = -\lambda^2/\omega_0^2$ which should give $\rho = 1$ by particle-hole symmetry, the symmetry is broken and there are two low temperature phases with $\rho = 1/3$ and $\rho = 2/3$. This is precisely analogous to a simulation of a magnetic (e.g. Ising) model at zero external field. Although symmetry demands magnetization $M = 0$, below T_c there are two phases with $M = \pm M_*$.

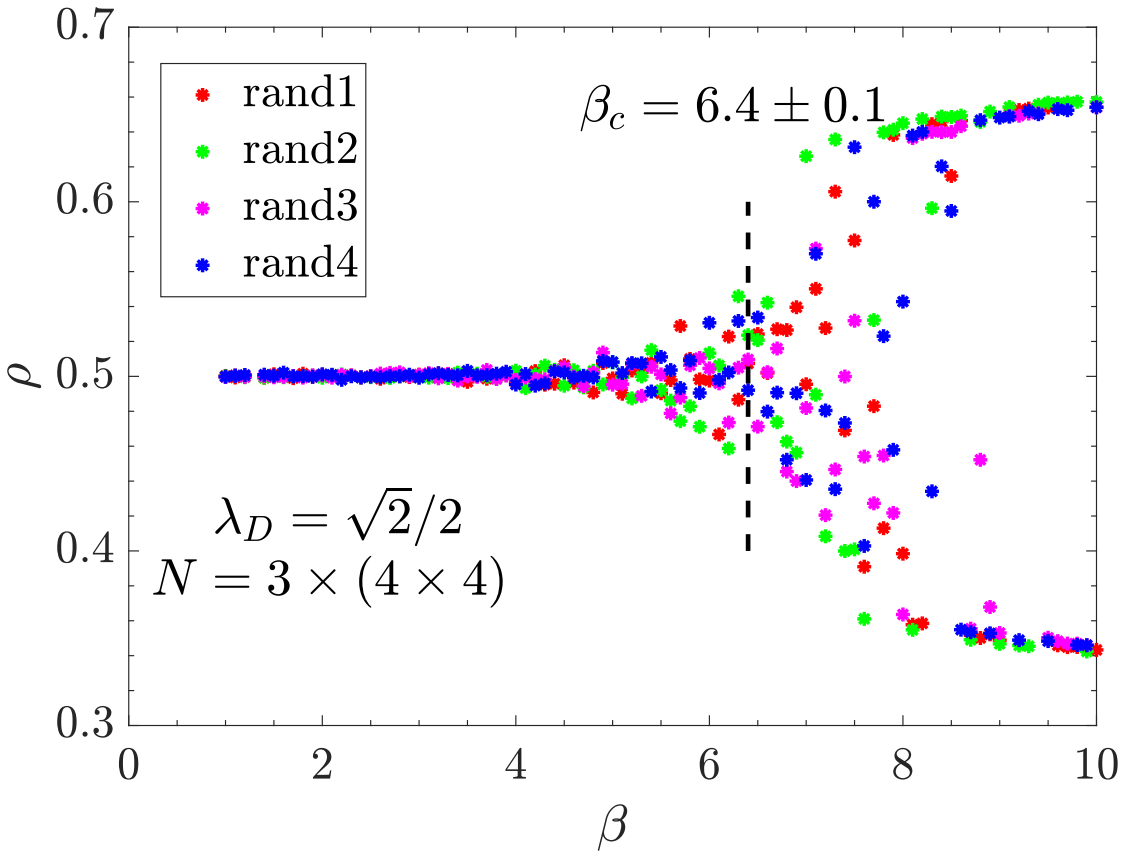

FIGURE 5.10. Density ρ as a function of β at the $\lambda_D = \sqrt{2}/2$. Data for four different random seeds are shown. A spontaneous symmetry breaking begins to occur at $\beta \sim 5$. See text for details. The vertical dashed line is the value of β_c detemined from FSS of $S_{\rm cdw}$.

Plots of the density ρ versus chemical potential μ (Fig. 5.11) also reveal the CDW phase. At high temperatures ρ evolves smoothly between the empty and a fully-packed limits, transiting half-filling at the particle-hole symmetry point $\mu = -\lambda^2/\omega_0^2$. At temperatures below the CDW transition, a plateau develops in which the compressibility $\kappa = d\rho/d\mu$ vanishes. However, unlike the situation on a bipartite lattice in which each sublattice has equal numbers of particles, the plateau is bifurcated by an abrupt jump as the system transitions from occupation of the minority to majority sublattice.

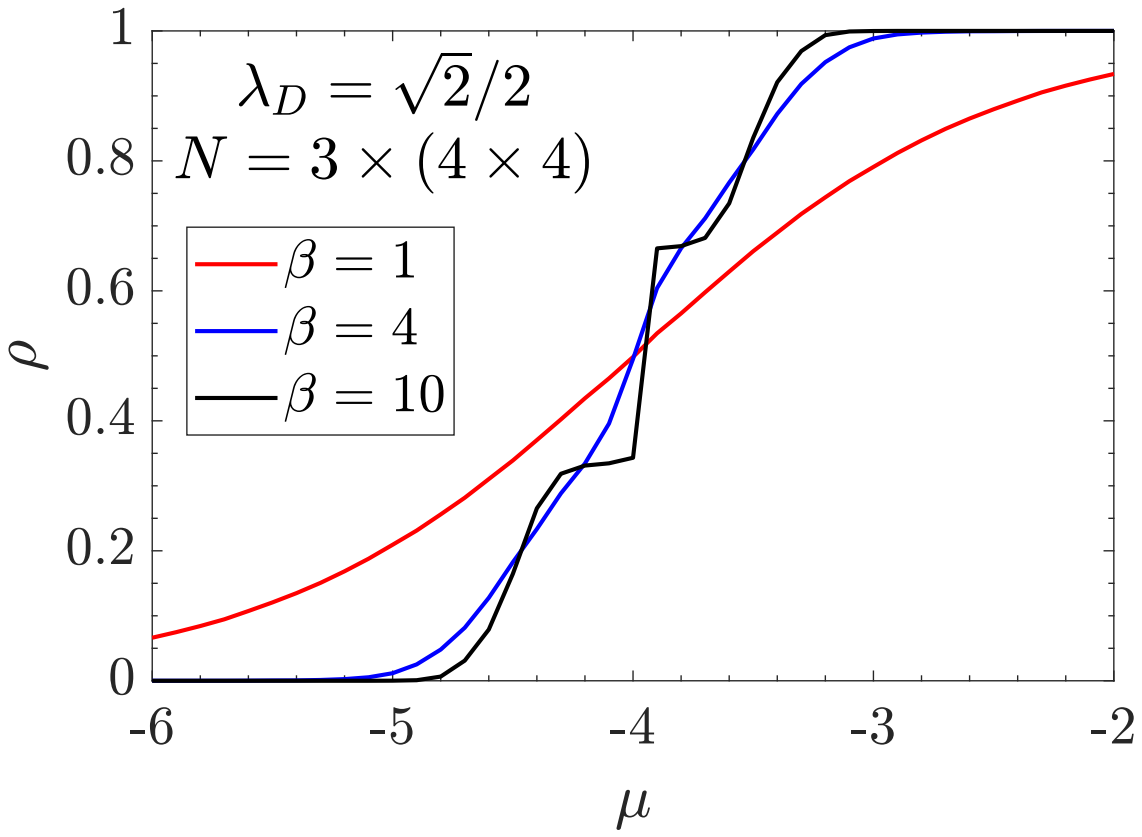

FIGURE 5.11. Density ρ vs. chemical potential μ for several different β obtained in DQMC simulations. Here $\lambda = 2, (\lambda_D = \sqrt{2}/2)$.

Figure 5.12 is similar to Fig. 5.10 except showing the double occupancy $\mathcal{D}$. At low β (high T), $\mathcal{D} = \langle n_{\mathbf{i}\uparrow} n_{\mathbf{i}\downarrow} \rangle \sim \langle n_{\mathbf{i}\uparrow} \rangle \langle n_{\mathbf{i}\downarrow} \rangle \sim 1/4$. As T decreases below the pair binding scale

$U_{\text{eff}} = \lambda^2/\omega_0^2 \sim 4$, pairs begin to form on half the sites ($\mathcal{D} \sim 0.5$). At larger β a CDW pattern emerges in which $\mathcal{D} = 0$ or $\mathcal{D} = 1$ depending on which sublattice is occupied.

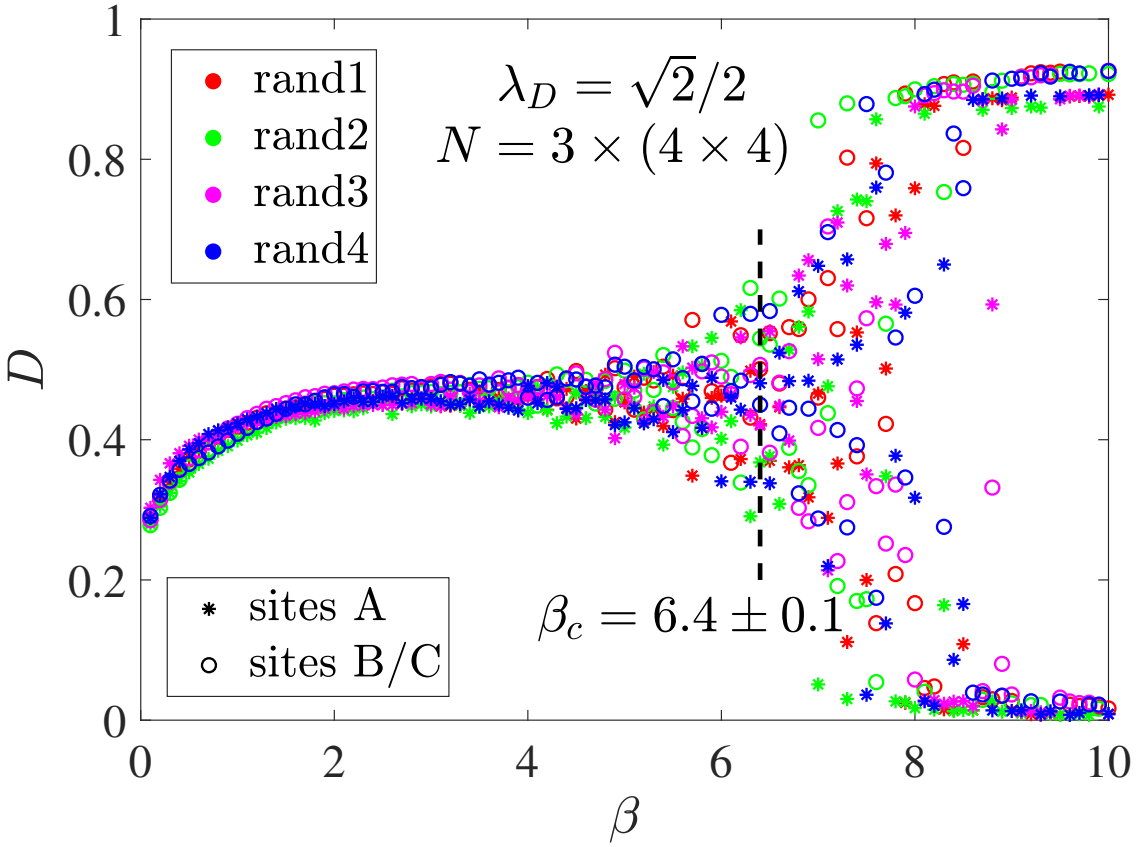

FIGURE 5.12. Double occupancy $\mathcal{D}$ vs β at $\lambda = 2(\lambda_D = \sqrt{2}/2)$ for a $3\times(4\times4)$ lattice and $\mu = -\lambda^2/\omega_0^2$. Data for four different random seeds are shown. The vertical dashed line is the value of β_c detemined from FSS of S_{cdw}.

Figure 5.13 is the phase diagram of the Holstein model on a Lieb lattice in the plane of temperature-dimensionless coupling constant. We also compare to several other geometries. A striking feature of the plot is that the honeycomb and Lieb lattice values are so close. Naively, one might have argued that the delta-function divergence of the Lieb lattice flat band density of states would lead to a large T_c, especially when compared to the semi-metallic case of the honeycomb lattice. However, the explanation is clear- The Lieb lattice CDW order really occurs for $\rho = 1/3$ and $\rho = 2/3$, where it has Dirac cones much like

the honeycomb lattice. Thus the only difference is that the honeycomb lattice coordination number $z = 3$, whereas for the Lieb geometry the average coordination number is slightly smaller $\bar{z} = 2/3(2) + 1/3(4) = 8/3$.

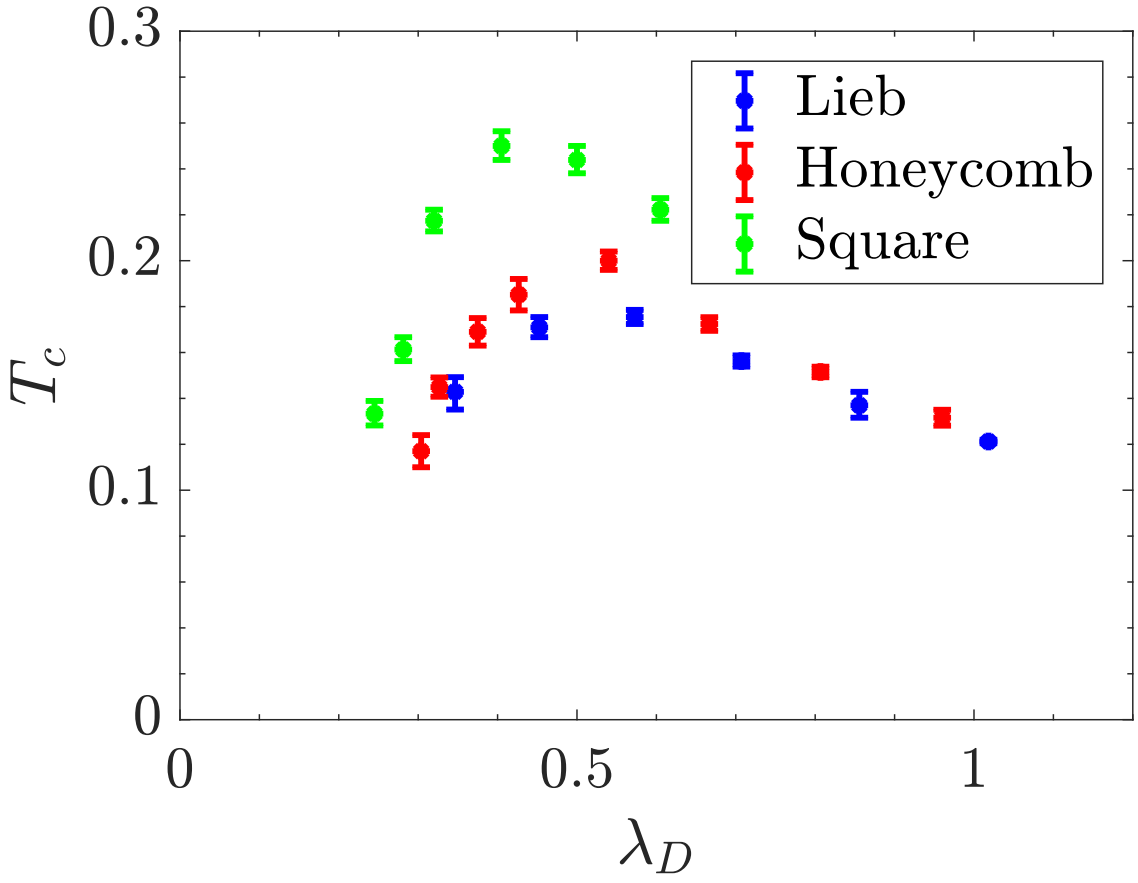

FIGURE 5.13. Critical temperatures for the Lieb lattice (this work) and the honeycomb [**1**] and square lattices.

CHAPTER 6

Phase Diagram of the Su-Schrieffer-Heeger-Hubbard model on a square lattice

6.1. Introduction

Electron-electron and electron-phonon interactions play important roles in determining the ground state properties of many-body systems. Over the past decades, much computational effort has been put into studying systems that feature one or the other of these interactions. One of the most widely used models to study the effect of electron-electron interaction with on-site repulsion U is the Hubbard model [**3**] which exhibits metallic, ferromagnetic, antiferromagnetic (AF) and superconducting (SC) orders, as well as intricate inhomogeneous spin and charge patterns, depending on U and the doping [**4**, **5**]. The physics of the square lattice Hubbard model bears remarkable resemblance to that of the cuprate superconductors. Two of the most commonly studied electron-phonon Hamiltonians are the Holstein [**75**] and the Su-Schrieffer-Heeger (SSH) [**76**] models. Their fundamental difference is that in the former, electrons and phonons interact on a single site, while in the latter, the electron-phonon interactions occur on the bonds, *i.e.* in the tunneling term. The Holstein interaction is widely used to explore polaron and charge-density wave (CDW) physics [**1**,**2**,**8**–**16**,**77**], and conventional s-wave SC transitions [**6**,**7**], while the SSH interaction occurs in systems like conjugate polymers [**17**], organic charge transfer salts [**18**], metal salts [**19**] and $CuGeO_3$ [**20**].

In the two-dimensional square lattice, the half-filled Holstein model predicts the emergence of a CDW phase at any value of the electron-phonon interaction λ [**39**]. In the presence of an additional on-site electron-electron repulsion U, the system can exhibit dominant AF

or CDW correlations depending on the relative magnitude of U and λ [**40**, **41**]. Interestingly, there are indications of an intermediate metallic phase between the AF and CDW phases [**42**–**45**], as well as other exotic regimes [**46**].

For the 2D square lattice SSH model at half-filling, it was shown [**47**] that a finite critical electron-phonon interaction, λ_c, is needed to establish the bond-order-wave (BOW) phase, and weak antiferromagnetism was detected [**48**, **49**] for $\lambda < \lambda_c$ despite the absence of U. In the dilute limit, where bipolarons are expected to condense into a superfluid at very high temperatures, AF is revealed as well in the effective Hamiltonian [**162**]. The cause of this antiferromagnetism is that, on a given bond, only electrons of different spin can tunnel simultaneously, resulting in a lowering of the energy via the electron-phonon coupling on the bonds and an *increase* in the magnitude of the kinetic energy. In contrast, in the Hubbard model at half-filling, AF order emerges in a two-step process in which U first suppresses doubly occupied sites, and then AF order occurs due to a small remnant exchange process $J \sim 4t^2/U$. The AF phase in the Hubbard limit is thereby accompanied by low kinetic energy. This distinction will play a role in a cross-over behavior we observe in the Su-Schrieffer-Heeger-Hubbard (SSHH) phase diagram.

We study here the rich interplay of BOW and AF regimes in the SSHH model. Crucially, since the phonons couple to the electrons via the kinetic term, particle-hole symmetry is preserved and there is no sign problem (SP) at half-filling. This allows us to use determinant quantum Monte Carlo (DQMC) to study systems up to 12×12 in size and at very low temperature. This contrasts with the Hubbard-Holstein model, where the SP precludes crossing the CDW-AF phase boundary [**45**]. Our resulting phase diagram (Fig. 6.1) exposes phases of long range AF and BOW order. Prior to our work, only the quantum critical point along the $U = 0$ axis (the SSH Hamiltonian) had been determined [**47**]. A central observation of this work is that there are, within the AF phase, distinct regimes at small and intermediate electron-phonon coupling λ. The AF structure factor, double occupancy and

kinetic energy remain almost constant for small λ. However, for larger λ these quantities show a marked dependence on λ. As a consequence, we will argue that the competition between λ and U results not only in the expected AF-BOW transition, but also in a novel crossover *within* the AF phase. This crossover is clearly signaled in the AF correlations themselves, and also in the double occupancy, kinetic energy and pairing structure factors. These changes result from competition of the localizing effect of the Hubbard term and the quantum fluctuations favored by the SSH term, although they both can lead to AF.

6.2. Model and Method

We study the square lattice optical SSHH model, where the electronic hopping is modulated by an electron-phonon interaction and an on-site Coulomb repulsion is present. The Hamiltonian is

$$\begin{aligned}\mathcal{H} = &- t \sum_{\langle i,j\rangle,\sigma} \left(1 - \lambda \hat{X}_{ij}\right) \left(\hat{c}^{\dagger}_{i\sigma} \hat{c}_{j\sigma} + \text{h.c.}\right) - \mu \sum_{i,\sigma} \hat{n}_{i\sigma} \\ &+ \sum_{\langle i,j\rangle} \left(\frac{1}{2M} \hat{P}^2_{ij} + \frac{M}{2} \omega_0^2 \hat{X}^2_{ij}\right) \\ &+ U \sum_i \left(\hat{n}_{i\uparrow} - \frac{1}{2}\right) \left(\hat{n}_{i\downarrow} - \frac{1}{2}\right), \end{aligned} \tag{6.1}$$

where $\hat{c}_{i\sigma}$ ($\hat{c}^{\dagger}_{i\sigma}$) destroys (creates) an electron of spin $\sigma =\uparrow,\downarrow$ on site i, μ is the electron chemical potential, M is the phonon mass and ω_0 the oscillation frequency. The bond phonon displacement operator $\hat{X}_{ij}$ connects nearest neighbor sites $\langle i,j\rangle$; its conjugate bond momentum is $\hat{P}_{ij}$. In the following, the magnitude of electron phonon coupling is given by the dimensionless parameter $g = \lambda/\sqrt{2M\omega_0/\hbar}$, so that the coupling term is $tg(\hat{b}_{ij} + \hat{b}^{\dagger}_{ij})(\hat{c}^{\dagger}_{i\sigma}\hat{c}_{j\sigma} +$ h.c.). The on-site Coulomb repulsion is U/t, and $\hat{n}_{i\sigma} = \hat{c}^{\dagger}_{i\sigma}\hat{c}_{i\sigma}$ is the number operator on site i. We work in units for which $\hbar = t = M = 1$ and fix $\omega_0 = 1$.

The Hubbard-Stratonovich (HS) transformation is used in DQMC [**8**, **39**, **101**, **156**], to express the quartic Coulomb interaction in quadratic form [**163**, **164**]. The fermions are

integrated out, yielding a determinant of a matrix that has dimension of the number of spatial sites N. The entries of the matrix depend on the HS and phonon fields. We focus on half-filling ($\mu = 0$), which does not present a SP, and work with $\beta = L_\tau \Delta\tau = 16$, where $L_\tau \sim 320$ is the number of imaginary slices, and $\Delta\tau$ is the imaginary time step. This β is sufficiently large to access the ground state of the SSH model on the lattice sizes under investigation here [**47**].

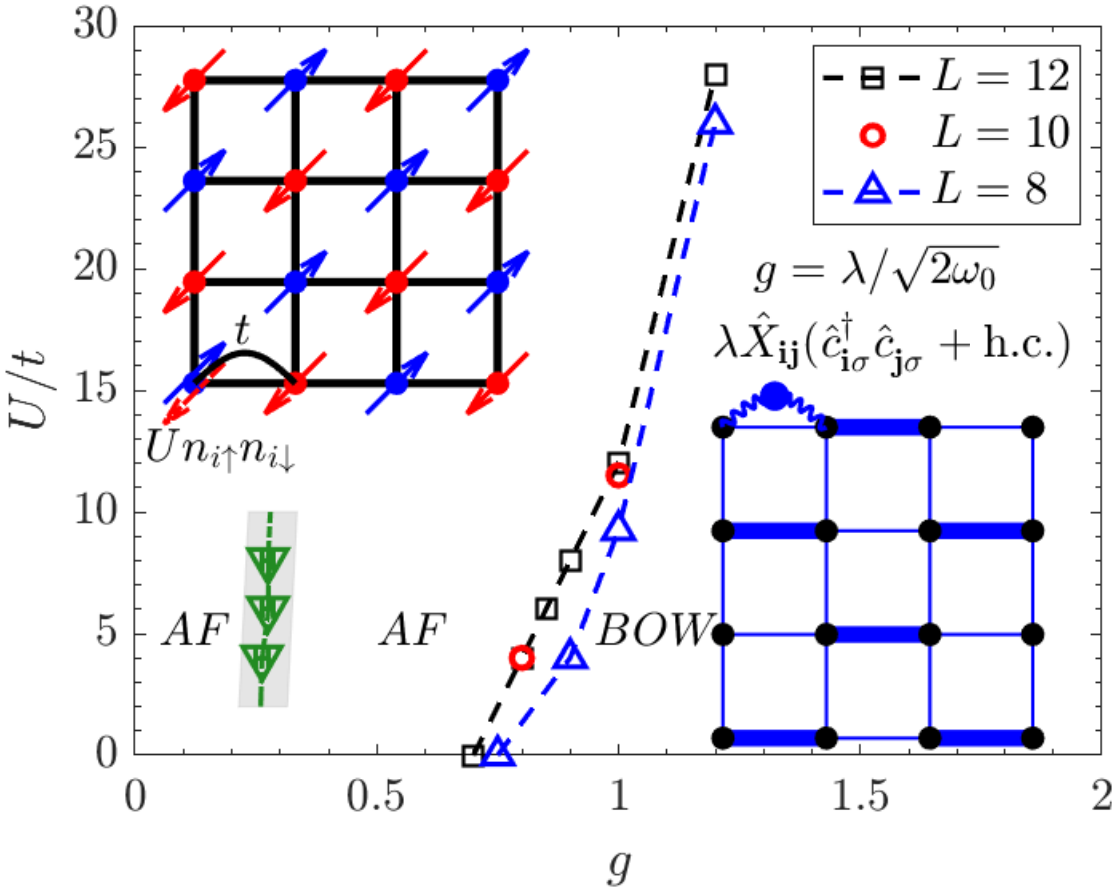

FIGURE 6.1. Phase diagram of the SSHH model at half-filling. g is the dimensionless electron-phonon coupling constant, and U/t is the Coulomb repulsion strength. A dotted (green) line shows the location of a crossover in the nature of the AF. $\beta = 16$ ensures the system is close to the ground state for all three lattice sizes. The AF-BOW transitions for $L = 10, 12$ coincide, indicating negligible finite size effects. The insets show schematically the AF and BOW phases.

To characterize the emerging phases, we calculate the average kinetic energy in the x and y directions, $\langle K_{x(y)} \rangle = \langle \hat{c}^{\dagger}_{i,\sigma} \hat{c}_{i+\hat{x}(\hat{y}),\sigma} + h.c. \rangle$, and the average phonon displacement in the x and y directions, $\langle X_{x(y)} \rangle$. These give insight into the broken x-y symmetry in the BOW phase. We also study the antiferromagnetic, $\langle S^x_i S^x_{i+r} \rangle$, and the bond order correlation functions, $\langle K_{x(y)}(i) K_{x(y)}(i+r) \rangle$. Their Fourier transforms, S_{AF} and $S_{K_{x(y)}}$, are respectively the AF and BOW structure factors. In addition, we examine the double occupancy, $D = \langle \hat{n}_{i\uparrow} \hat{n}_{i\downarrow} \rangle$ and the total kinetic energy $\langle K \rangle = \langle K_x \rangle + \langle K_y \rangle$ which provide additional important insight.

6.3. Results

6.3.1. Main Results

It is well known [**165**,**166**] that, at half filling, the square lattice Hubbard model, Eq.(6.1) with $\lambda = 0$, exhibits an AF phase for any $U > 0$. Similarly, it was recently established [**48**,**49**] that the two-dimensional SSH model, Eq.(6.1) with $U = 0$, exhibits, at low temperature, an AF phase for small λ and a BOW [**47**] when λ exceeds a critical value. Here we address the unknown structure of the phase diagram in the $(g, U/t)$ plane.

To this end, we determine the phase boundaries with vertical and horizontal cuts, *i.e.* by fixing g (U/t) and studying the behavior of the system as U/t (g) is changed. The AF and BOW phases are revealed by their respective structure factors, S_{AF} and $S_{K_x}(\pi, \pi)$. For low temperature and large systems, we start simulations with a phonon configuration that favors the BOW phase in the x direction (bottom right inset Fig. 6.1) because this structure is found to melt rapidly in the AF phase, but takes a long equilibration time to form. We measure $S_{K_{x(y)}}(k_x, k_y)$ for all momenta and observe a peak only at $S_{K_x}(\pi, \pi)$ when the system is in the BOW phase. Comparison of data for $L = 10, 12$ indicate negligible finite size effects.

Figure 6.2(a,c) shows the structure factors versus the dimensionless g for several fixed values of U/t. For $U/t = 4, 6, 8$ the system is a Hubbard AF for $g = 0$, and remains AF as g increases up to a critical value, $g_c(U/t)$. For $g < g_c$, S_{K_x} is small, indicating the absence of BOW. S_{K_x} then rises rapidly upon entry into the BOW phase at $g > g_c$.

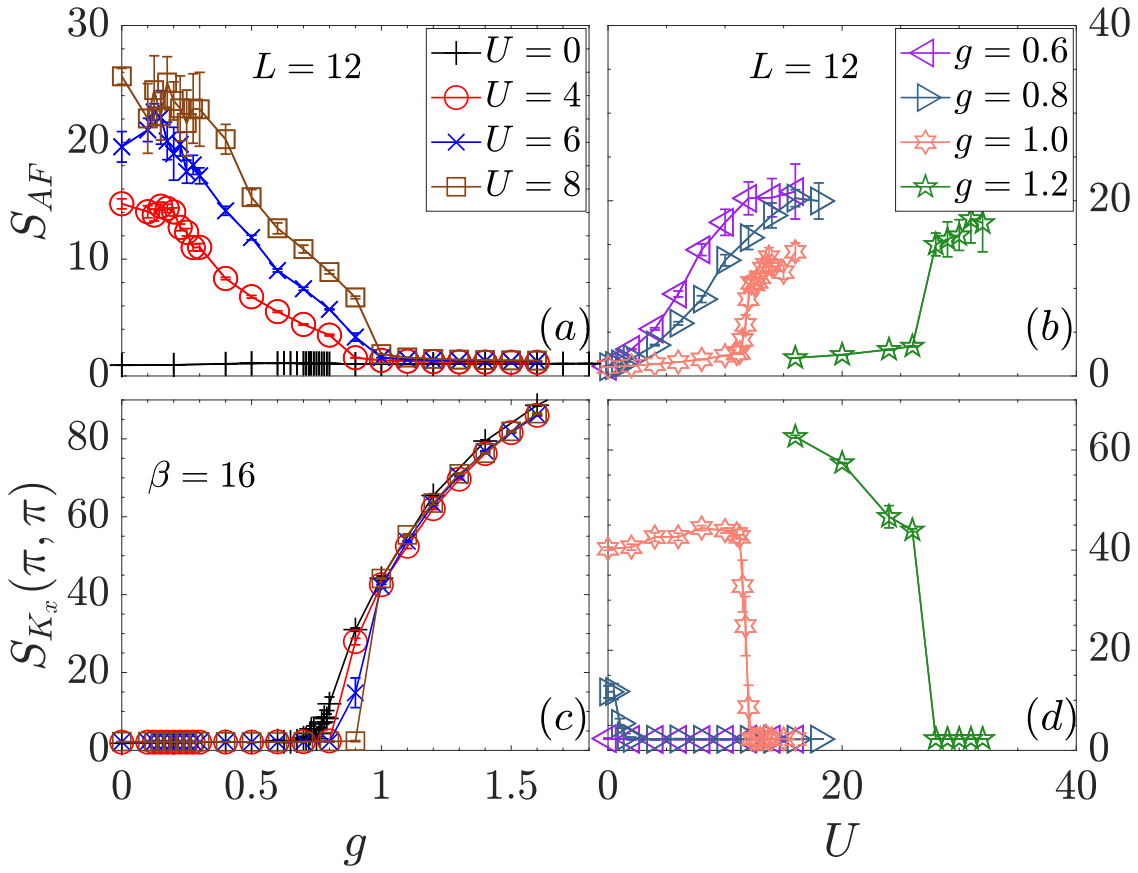

FIGURE 6.2. DQMC results of the AF (BOW) structure factor $S_{\rm AF}$ ($S_{K_x}(\pi,\pi)$) for horizontal (left) and vertical (right) cuts in the phase diagram. In the AF phase, $S_{\rm AF}$ is finite and $S_{K_x}(\pi,\pi)$ is negligible. In the BOW phase, $S_{\rm AF}$ is negligible and $S_{K_x}(\pi,\pi)$ is finite.

The behavior of the AF structure factor $S_{\rm AF}$ is more subtle. It is nonzero for $g < g_c$, but there is an appreciable change in behavior well *before* its value drops precipitously: $S_{\rm AF}$ is initially constant for small g, Fig. 6.2(a), but starts decreasing at $g_* \approx 0.2$. A finite size scaling analysis shows that AF regions exhibiting true long range order on both sides of g_*. The difference between these two AF regions, inferred from the kinetic energy and double occupancy will be discussed below. Indeed, since data for structure factors are more noisy than local correlation functions, these complementary observables will present additional compelling evidence for the crossover behavior at g_*.

Returning to the AF-BOW transition with increasing g, we see, Fig. 6.2(a), that when $S_{\rm AF}$ drops, S_{K_x} becomes nonzero. This occurs at $g_c \sim 1$ for $L = 12$. In Fig. 6.2(b,d) we show the same quantities as panels (a,c) but now g is fixed and U/t varies. For $g = 0.6$, S_{K_x} is small for all U/t while $S_{\rm AF}$ increases smoothly as U/t increases. For this value of g the system is always AF. For $g \geq 0.8$, $S_{\rm AF}$ is very small (essentially zero) while S_{K_x} is large up to a g-dependent critical value, $U_c(g)$, indicating that the system is in the BOW phase [**47**]. At $U_c(g)$, there is a first order transition from the BOW to the AF phase, with clear discontinuous jumps in the order parameters. This first order character is also observed for the larger U values in the horizontal cuts (sweeping g at fixed U) in Fig. 6.2(a,c).

As shown in Ref. [**47**], the BOW has (π, π) ordering vector either in x or in y with two sublattice possibilities in each direction, resulting in the Z_4 symmetry breaking (in the thermodynamic limit). We now focus on this symmetry breaking as the system leaves the AF phase and enters the BOW phase. In the AF phase, the average kinetic energy and phonon displacement in the x and y directions are equal. In the BOW phase, the average kinetic energy and phonon displacement which align with the BOW direction increase in magnitude. We show in Fig. 6.3 the behavior of these quantities for the same parameters as in Fig. 6.2. In panels (a,c), the x-y symmetry is preserved in the AF phase, $g < g_c(U)$, and broken immediately when the system enters the BOW phase. This is clearly seen in the bifurcation in $K_{x(y)}$ and $X_{x(y)}$ at g_c. As the on-site interaction becomes stronger, the electron-phonon coupling strength required to establish the BOW phase becomes larger.

In Fig. 6.3(b,d), for constant g, the x-y symmetry is broken for $U < U_c(g)$, $g \geq 0.8$ and restored immediately when the system exits the BOW and enters the AF phase at $U_c(g)$. For $g = 0.6$, the system is never in the BOW phase for all U and therefore the x-y symmetry is always preserved. The values of $g_c(U)$ and $U_c(g)$ obtained in Fig. 6.2 and Fig. 6.3 are in close agreement. We remark that, as observed in both figures, a small increase in g (i.e. from

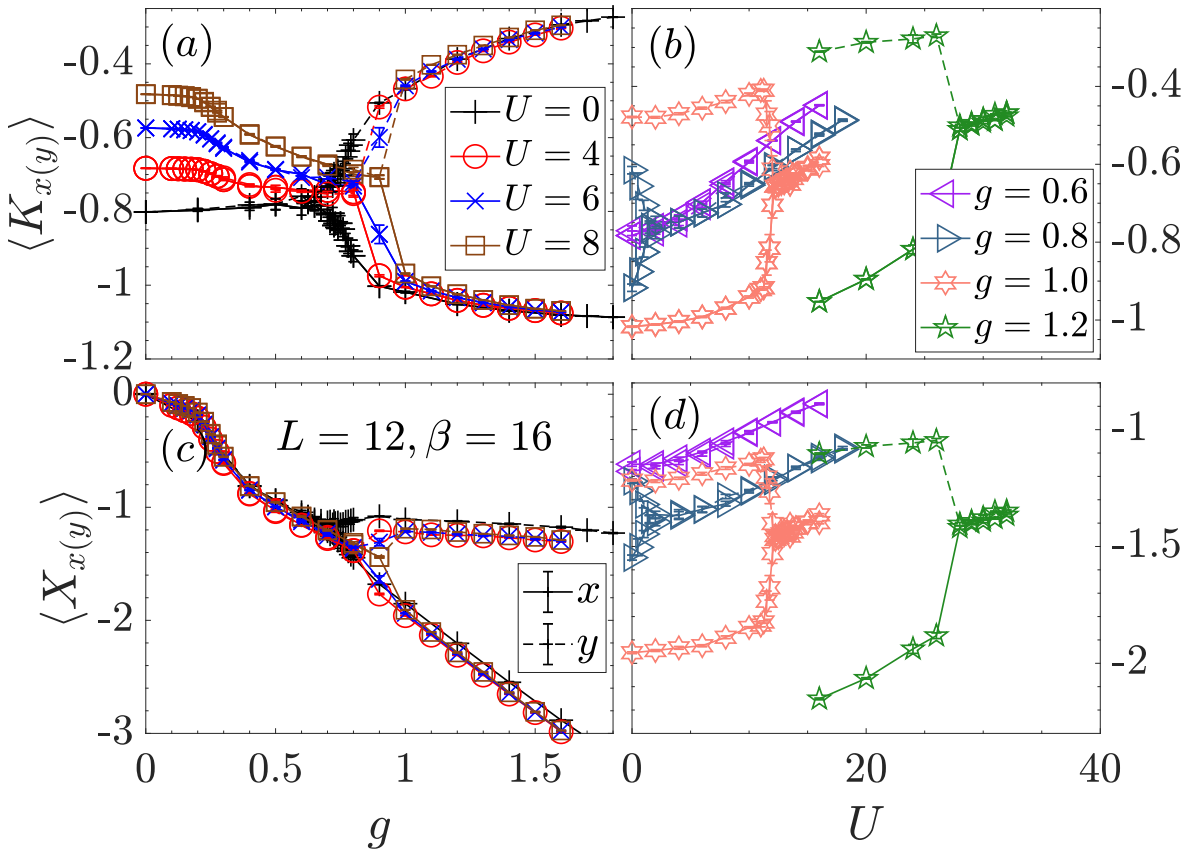

FIGURE 6.3. DQMC results of average kinetic energy, $\langle K_{x(y)} \rangle$, and average phonon displacement, $\langle X_{x(y)} \rangle$, in x and y directions for horizontal (left) and vertical (right) cuts in the phase diagram.

1.0 to 1.2) leads to significant changes of U_c (i.e. 12 to 26). Putting these cuts at constant g and U together yields the phase diagram shown in Fig. 6.1.

We now focus on the two AF regions (separated by the vertical dotted line in Fig. 6.1) for which S_{AF} provided initial evidence. We recall that for $g = 0$, the system is in the Hubbard AF phase for any $U > 0$, while for $U = 0$, the system is in the SSH AF phase [**48**, **49**] for small g. The SSH AF at $U = 0$ clearly has a different mechanism from the traditional two step Hubbard model process of moment formation at energy scale U followed by moment ordering at energy scale $J \sim 4t^2/U$. A close analysis of Fig. 6.3(a,c) shows that both $\langle K_{x(y)} \rangle$

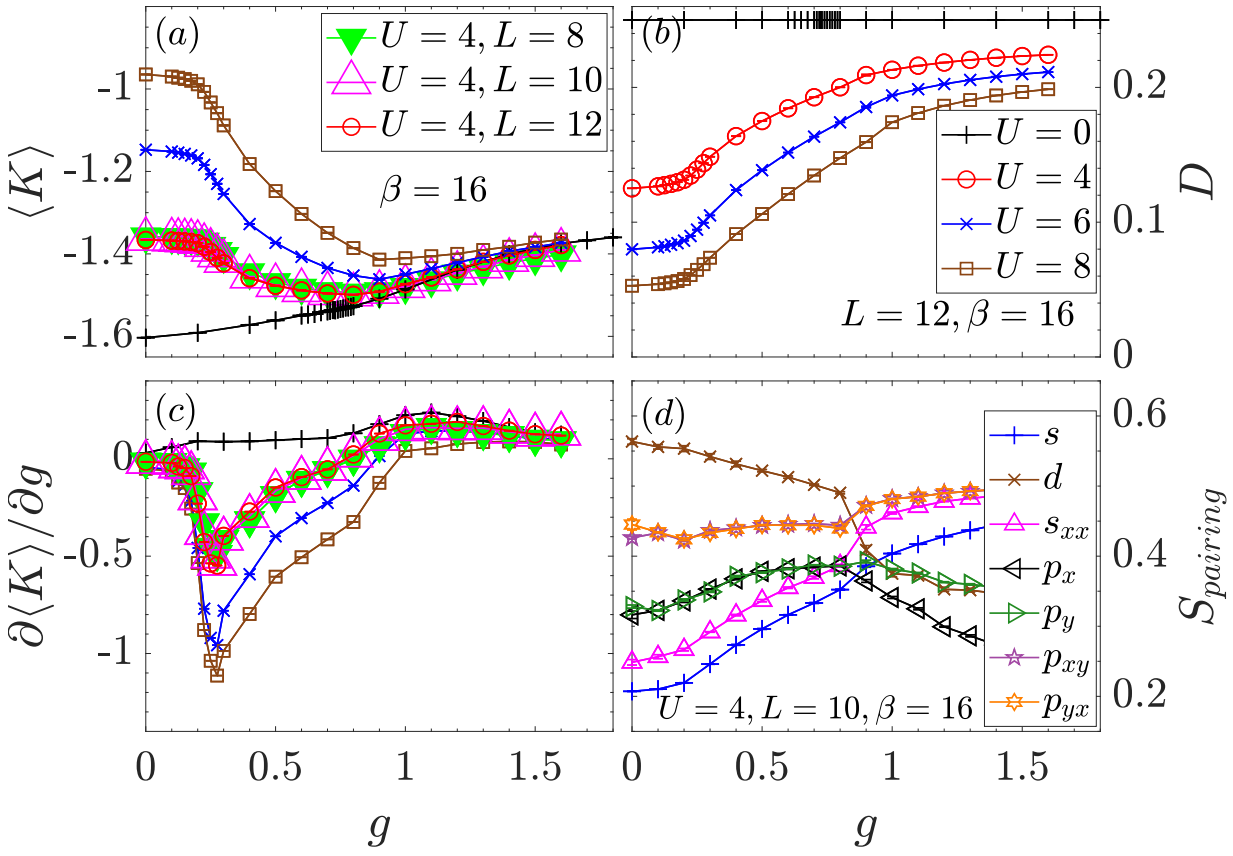

FIGURE 6.4. (a) Average kinetic energy. (b) double occupancy for different U and fixed lattice size $L = 12$; (c) derivative of the kinetic energy with respect to g. The legends in panels (a,b) explain the symbols in panels (a,b,c). (d) pairing structure factors at fixed $U = 4$ and $L = 10$.

and $\langle X_{x(y)} \rangle$ remain almost constant for $g \lesssim 0.2$ and then increase in magnitude for $g > 0.2$. Similarly, the AF structure factor in Fig. 6.2(a) is approximately constant for $g \lesssim 0,2$ and decreases for larger values of g.

In Fig. 6.4(a), we show the average kinetic energy as a function of g for several values of U. $\langle K \rangle$ clearly exhibits a change of behavior at $g_* \approx 0.2$, supporting what is seen in Fig. 6.2 for S_{AF}. This is captured even more effectively in Fig. 6.4(c), which shows a sharp peak at $g \sim 0.275$ in $\partial \langle K \rangle / \partial g$ vs g. A comparison between $\langle K \rangle$ given in this SSHH Hamiltonian and in an (approximate) 'effective' Hubbard model gives more insight on this crossover.

Figure 6.4(b) shows the double occupancy, D, which increases in value for $g \gtrsim 0.2$. This behavior (larger kinetic energy and double occupancy) indicate that the system has left the "large U" Hubbard AF, where both quantities are suppressed, and entered an AF region strongly influenced by the SSH electron-phonon coupling, where quantum fluctuations are large. Going from one of these AF regions to the other is a crossover, not a phase transition. Nevertheless, there is a clear signature in the increased quantum fluctuations.

Since the pure SSH Hamiltonian preserves $O(4)$ symmetry, and an AF/CDW/SC degenerate ground state is expected in the anti-adiabatic limit [**48**, **49**], it is useful to examine the superconducting structure factor S_{pairing}, the spatial sums of the real space correlations $\langle \Delta_\alpha(i+r)\Delta_\alpha^\dagger(i)\rangle$ with standard conventions $\Delta_s^\dagger(i) = c_{i\uparrow}^\dagger c_{i\downarrow}^\dagger$, $\Delta_d^\dagger(i) = c_{i\uparrow}^\dagger \frac{1}{2}(c_{i+x\downarrow}^\dagger - c_{i+y\downarrow}^\dagger + c_{i-x\downarrow}^\dagger - c_{i-y\downarrow}^\dagger)$, etc. [**167**]. These are shown in Fig. 6.4(d). Similar changes are observed at the crossover. A bifurcation in pairing with p_x and p_y symmetry, as well as the sharp change in d, and s_{xx} pair form factors, at $g_c \sim 0.9$ also signal the AF-BOW phase transition. An interesting, and intuitively reasonable, observation is that a BOW pattern formed along the x or y-direction of the square lattice, increases pairing along plaquette diagonals (p_{xy}, p_{yx}, and s_{xx}), but competes with pairing channels which are also aligned directly along the bonds (d, p_x, p_y).

6.3.2. An approximate treatment of the SSHH model in terms of a pure Hubbard Hamiltonian with a renormalized U_{eff}

In the Holstein model, where the phonons couple to the local charge density $H_{\text{el-ph}} = \lambda \sum_i \hat{X}_i n_i$, one can do Lang-Firsov transformations [**78**] and get an on-site attraction $U_{\text{eff}} = -\lambda^2/\omega_0^2$ in the anti-adiabatic limit. As a consequence, the physics of the Hubbard-Holstein model at weak λ can be qualitatively interpreted in terms of a reduced on-site repulsion $U - \lambda^2/\omega_0^2$.

If one integrates out the SSH (bond) phonons on a two site dimer, the resulting effective electron-only Hamiltonian has a renormalized U, but also additional inter-site terms. Nevertheless, one can still ask the extent to which the SSHH model considered here can be quantitatively modeled simply by a renormalized U. We analyze this issue as follows: We first take data for the double occupancy $D = \langle n_{i\uparrow} n_{i\downarrow} \rangle$ both for the SSHH model at fixed $U = 4$ and varying g and for the pure Hubbard model at varying U. For each g, We define $U_{\text{eff}}(g)$ to be the value of U in the pure Hubbard case which gives the same D for the SSHH model. The result is given in the inset of panel (a) in Fig. 6.5.

Next we compare the values of *other* observables between SSHH at $U = 4$ and varying g with pure Hubbard at U_{eff}. By construction, the values for D match perfectly. Fig. 6.5(a,b) gives the results for the antiferromagnetic structure factor S_{AF} and kinetic energy $\langle K \rangle$ respectively. For S_{AF} the agreement between the actual SSHH data and the effective model is remarkable- the results match to within a few error bars across the complete range of g. Perhaps not surprisingly, the SSHH model captures the more abrupt change in S_{AF} at the AF-BOW phase transition than the effective model, which has no such transition.

The kinetic energy agreement is less good quantitatively, but still quite accurate qualitatively for small g. The effective model of course cannot capture the reduction in the magnitude of the kinetic energy at large g which occurs upon entry into the BOW phase. It is also observed in Fig. 6.5(b) that the kinetic energy of the SSHH model remains more constant for small g than does the kinetic energy of the effective model, an effect reminiscent of the appearance of weak g AF regime discussed in the main text. The effective model gives a rough context in which to understand the suppression of magnetism by g. The resulting accuracy of panel (a) of Figure S1 is of additional interest: it is not obvious that adjusting U to get a match for a local observable like double occupancy would also give a good match for intersite magnetic correlations.

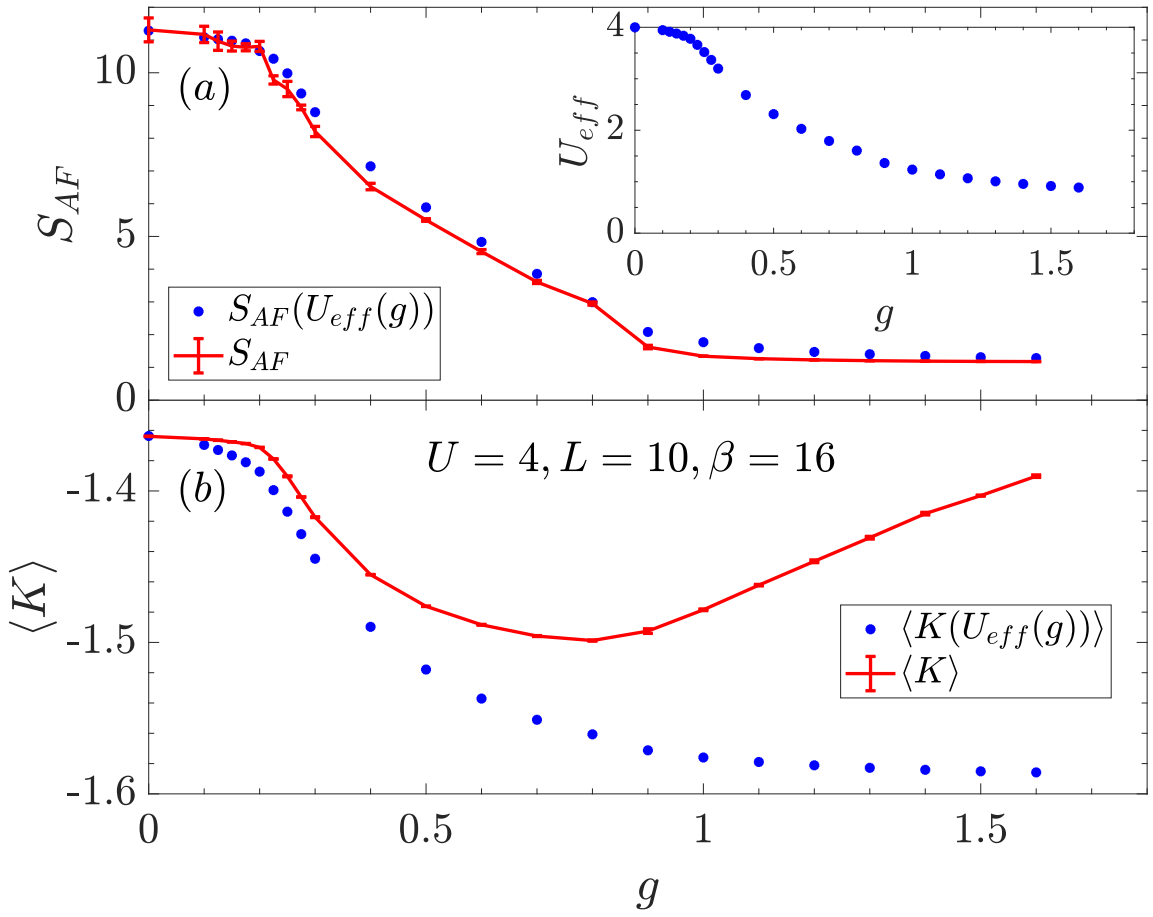

FIGURE 6.5. Inset in panel (a): In SSHH model, when $U = 4, \beta = 16$ on a $L \times L = 10 \times 10$ square lattice, for each g, we define U_{eff} as the onsite electron repulsion in the pure Hubbard model which gives the same double occupancy D. (a) AF structure factor (b) Electron Kinetic energy given in SSHH model (red curve), for $U = 4$, varying g, $\beta = 16$ on a $L \times L = 10 \times 10$ square lattice and in pure Hubbard model(blue dot) when $\beta = 16$ on a $L \times L = 10 \times 10$ with U_{eff} defined in Fig. 6.5 (a) inset. Two curves are in reasonable agreement at relatively small g, while the discrepancy at large g is because BOW phase can not be captured by the pure Hubbard model.

6.3.3. Bond ordered wave structure factor

For all simulations, we start with a phonon configuration that favors the development of XX bond ordered wave (BOW) pattern, i.e. (π, π) order of the x bonds. As noted in the main text, we have verified that for small lattices and high temperatures, correlation functions are

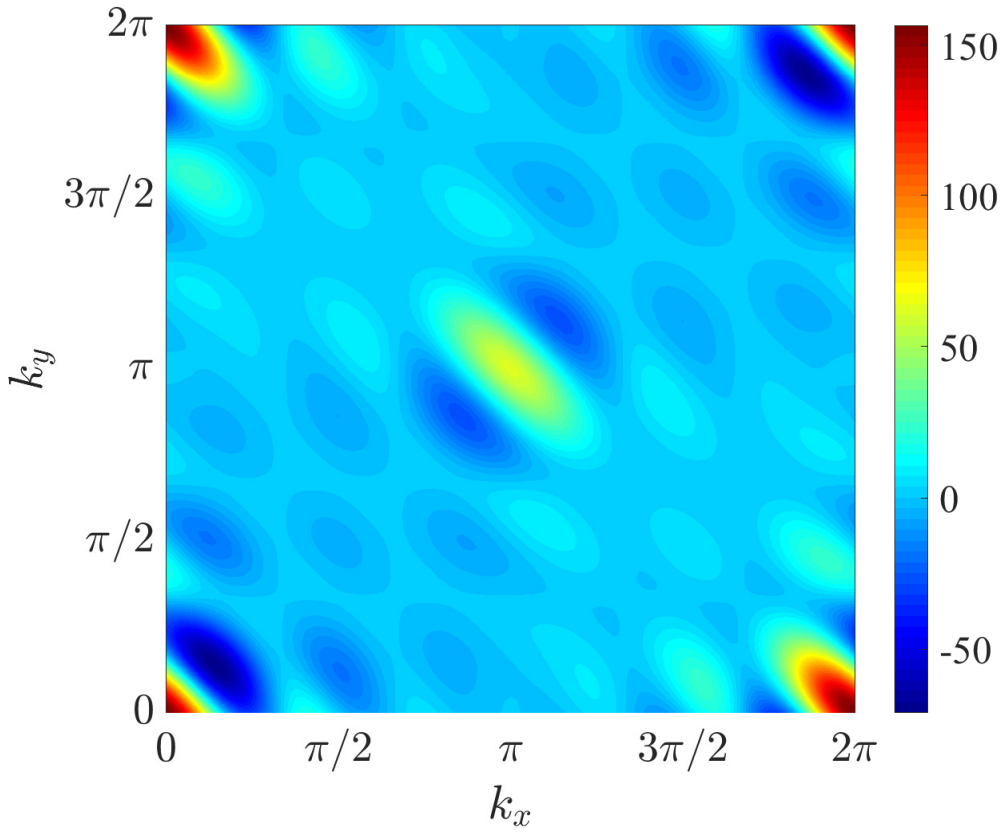

FIGURE 6.6. Bond ordered wave structure factor, $S_{K_x}(k_x, k_y)$ as a function of momentum k_x, k_y for $U = 4$, $g = 1.5$, $\beta = 16$, $L = 12$.

independent of initial configuration, and evolve to a consistent long time state. In addition, for all lattice sizes and temperatures, BOW melts rapidly when it is not supported by the parameters of the simulation. Thus our choice of starting configuration serves only to minimize long equilibration times in the BOW phase, and does not affect our determination of the phase diagram. Fig. 6.6 shows the BOW structure factor $S_{K_x}(k_x, k_y)$, the Fourier transform of bond-bond kinetic energy correlations in real space, as a function of momenta k_x and k_y. Besides a large value at $(k_x, k_y) = (0, 0)$, which is actually the sum of all spatial

correlations, a clear peak is observed at $(k_x, k_y) = (\pi, \pi)$ for $U = 4, g = 1.5, L = 12, \beta = 16$ system (in BOW phase).

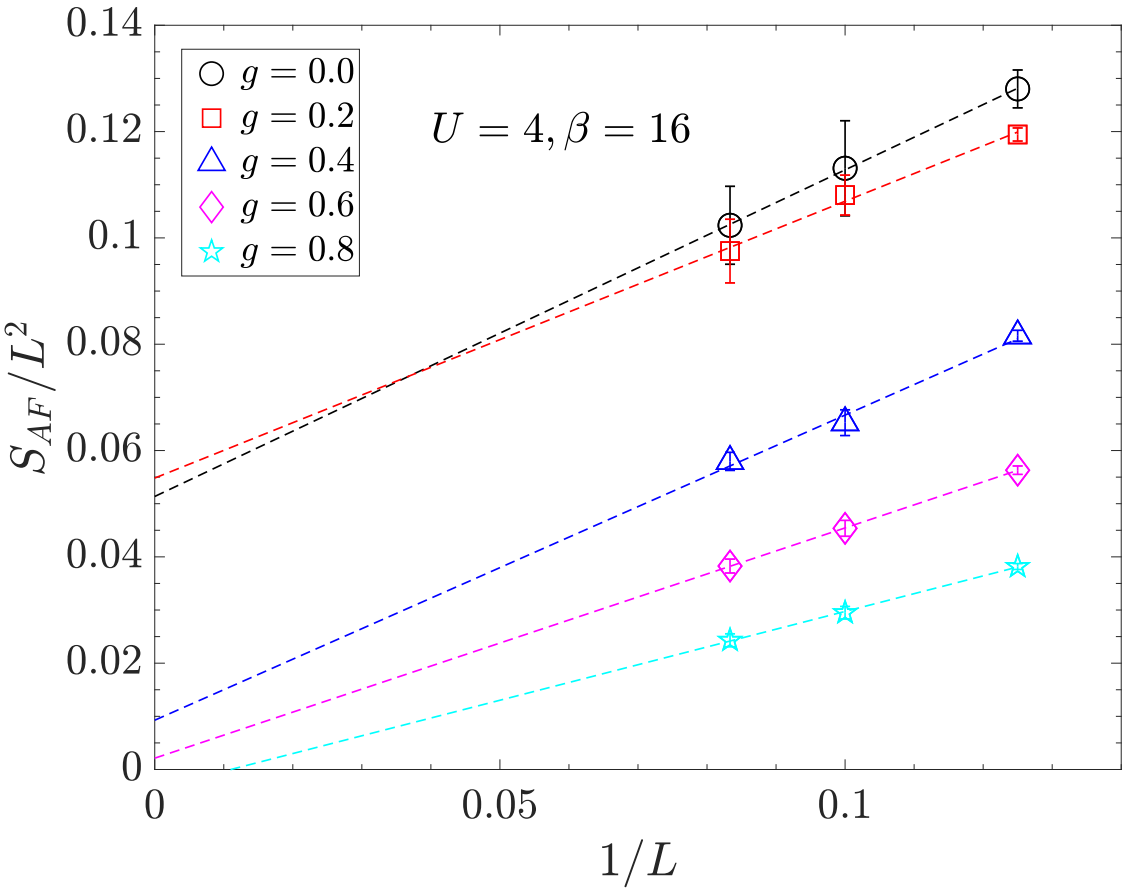

FIGURE 6.7. Finite size scaling of the antiferromagnetic structure factor, S_{AF}/L^2, for $g = 0,\ 0.2,\ 0.4,\ 0.6,\ 0.8$. The dotted lines are extrapolated from the simulations data. For all results shown in this panel, $U = 4,\ \beta = 16$.

6.3.4. Antiferromagnetic structure factor

In Fig 6.7, we perform finite size scaling (FSS) of the antiferromagnetic structure factor, S_{AF}/L^2 and show that the antiferromagnetic (AF) structure is present in the thermodynamic limit for both AF regions. At $U = 4,\ g = 0$, the system is in the AF phase. As g increases, S_{AF}/L^2 decreases in the thermodynamic limit. However, it is still finite and

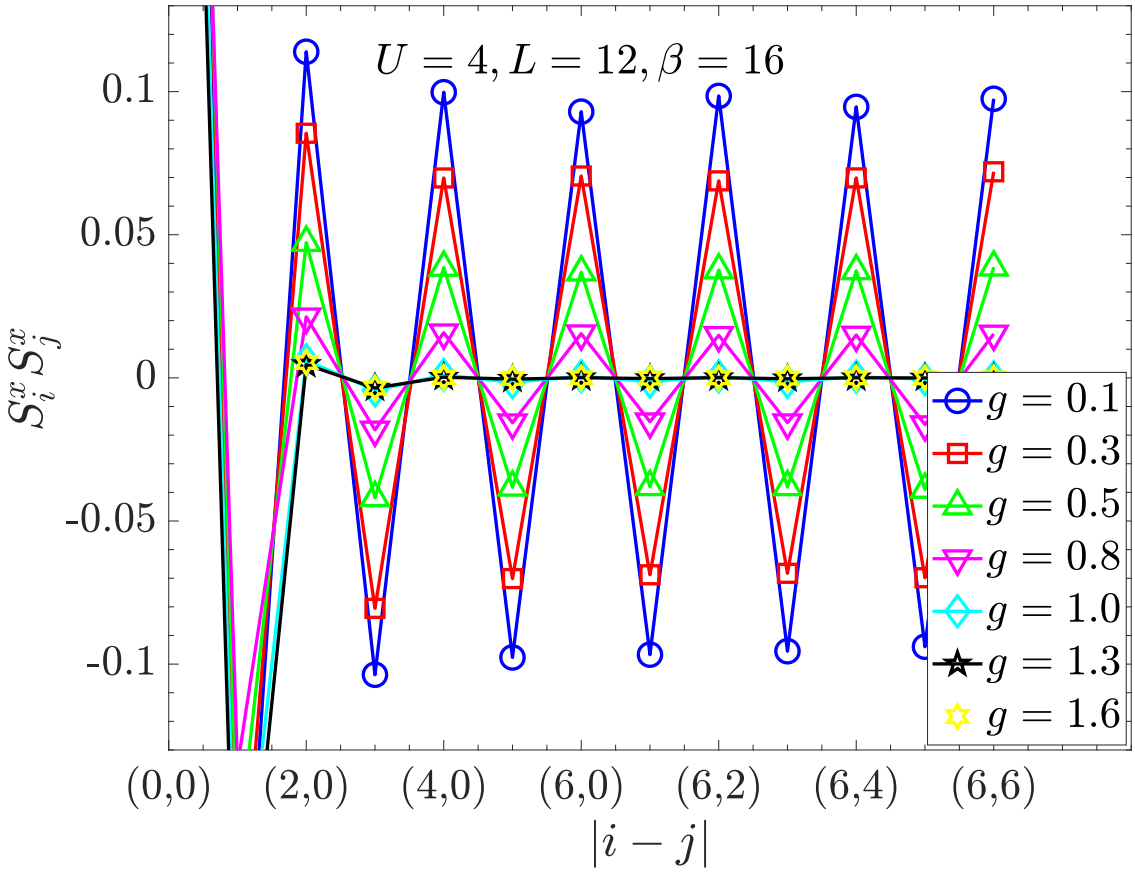

FIGURE 6.8. Spin-spin correlation, $\langle S_i^x S_j^x \rangle$ versus spatial distance $|i - j|$ for various g.

therefore indicative of the AF phase. At $g = 0.8$, we notice that FSS of S_{AF}/L^2 becomes less than zero. At the same time, the BOW structure factor, $S_{K_x}(\pi, \pi)$, rises sharply to a finite value, indicating the direct transition from the AF phase to the BOW phase.

In Fig. 6.8, the AF correlation function in real space gives similar conclusions. The oscillation of the AF correlation function, which does not decay with the spatial distance, gives evidence to the presence of the AF phase. As g increases, the magnitude of this oscillation decreases. The strong oscillation of the AF correlation function for $g < 0.8$, and the absence of BOW correlation, show that in this parameter region the system is AF.

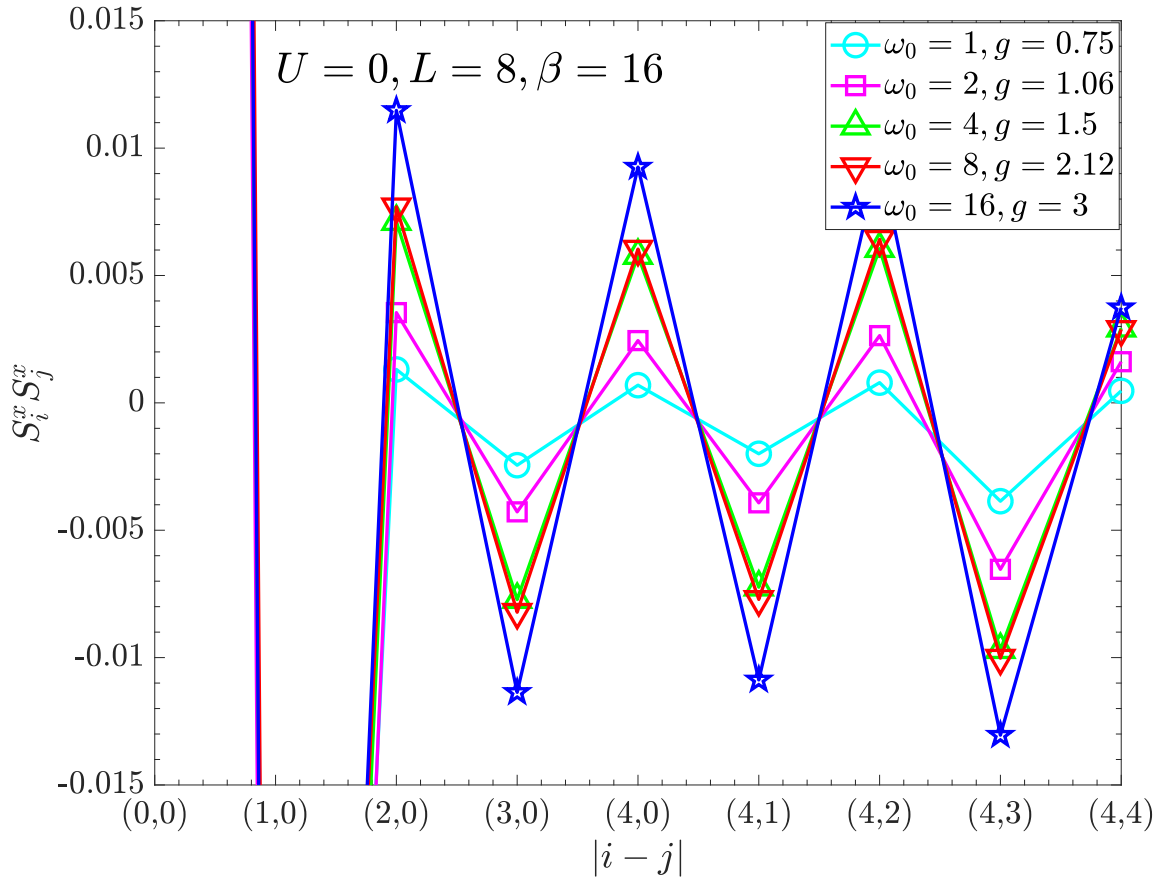

FIGURE 6.9. Spin-spin correlation, $\langle S_i^x S_j^x \rangle$ versus spatial distance $|i - j|$ for several phonon frequencies, ω_0, for the pure SSH model on an 8×8 square lattice. Increasing ω_0 at fixed g^2/ω_0 enhances AF order.

We also verify that for the pure SSH model($U = 0$), when $g \lesssim g_c$, long range AF order exists at low temperature ($\beta = 16$). The spin-spin correlation as a function of lattice site separation is shown in Fig. 6.9. As ω_0 increases with g^2/ω_0 (which is proportional to the spin exchange strength in the anti-adiabatic limit) fixed, the AF order is strengthened, which is consistent with the conclusion in [**48**, **49**]

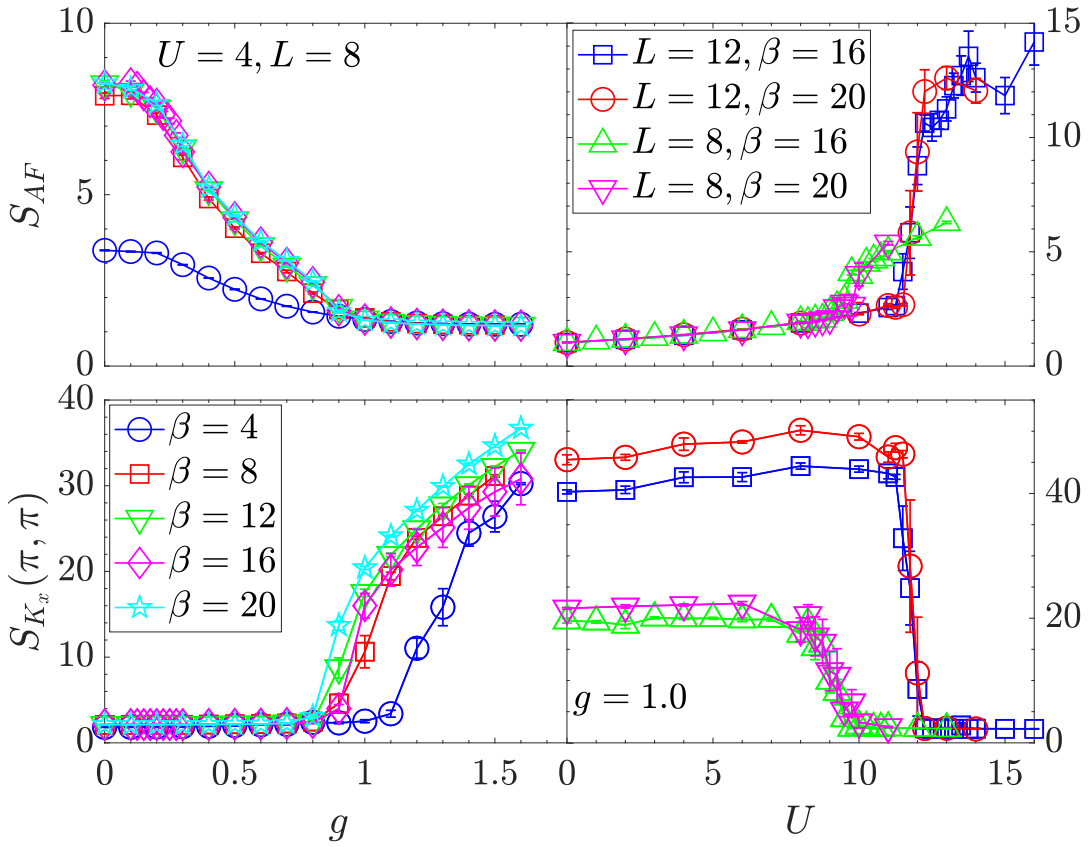

FIGURE 6.10. Left panels: AF and BOW structure factors vs. electron-phonon coupling g for a fixed $U = 4$, at several different temperatures $\beta = 4, 8, 12, 16, 20$. Right panels: AF and BOW structure factors vs. on-site Coulomb interaction U for a fixed $g = 1.0$, $\beta = 16, 20$ on 8×8 and 12×12 lattices. Both panels indicate $\beta = 16$ is low enough to capture the ground state physics for the SSHH model.

6.3.5. Structure factors at several different temperatures

In the left panels of Fig. 6.10, the AF and BOW structure factors are plotted as functions of electron-phonon coupling strength g for a fixed $U = 4$ on a 8×8 square lattice. The curves almost overlap when $\beta \gtrsim 8$, indicating the temperature we use ($\beta = 16$) in the main text is low enough to capture the ground state physics. Similarly, the right panels are structure

factors S_{AF} and $S_{K_x}(\pi,\pi)$ vs. U. Although their magnitudes at $\beta = 20$ in the ordered phase are slightly larger than those given by $\beta = 16$, the transition point given by them coincide for both $L = 8$ and $L = 12$ lattices respectively. There is some finite size effect going from $L = 8$ to $L = 12$ in both Fig. 6.10 and Fig. 6.1 but there is no such effect between $L = 10$ and $L = 12$.

CHAPTER 7

Charge Singlets and Orbital Selective Charge Density Wave Transitions

7.1. Introduction

Over the last several decades, much attention has been focused in the condensed matter community on layered materials. One prominent example is that of the cuprate superconductors (SC) [**50**–**54**]. Bilayer graphene [**55**–**60**] is another, more recent, realization. From a theoretical perspective, bilayer materials offer an opportunity to explore the competition between the formation of long range order at weak interlayer coupling and collections of independent local degrees of freedom in the limit of strong interlayer coupling. Computational studies have lent considerable insight into these phenomena, including quantitative values for the quantum critical points [**168**–**172**] separating antiferromagnetic and singlet phases at zero temperature.

This competition is central to that which occurs in multiorbital systems, notably the interplay of Ruderman-Kittel-Kasuya-Yosida order and singlet formation in the Kondo lattice and periodic Anderson models [**173**–**175**]. This close analogy originates in the observation that, in calculations on a model Hamiltonian, there is no difference between multi-layer and multi-orbital descriptions, apart from the interpretation of the additional label of the fermionic species. For this reason we will use the two terminologies interchangeably here. In multi-orbital language, one of the key conceptual interests is the possibility that the distinct values of the ratio of interaction strength to kinetic energy in the different bands might result in *separate* insulator transitions, i.e. the possibility of an 'orbital-selective' Mott transition (OSMT) [**61**–**72**].

Here we study analogous questions concerning bilayer (bi-orbital) systems in which the fermions interact with phonon degrees of freedom rather than via direct electron-electron correlations. A precise mathematical description of the mapping between the two situations is discussed. Quantum Monte Carlo (QMC) simulations have already been applied to the analysis of charge-density wave (CDW) and superconducting (SC) transitions in the single band Holstein model [**75**]. However, thus far, work has focused mostly on two-dimensional or three-dimensional models with a single kinetic energy scale [**1**, **2**, **11**–**13**, **15**, **16**, **39**, **77**, **152**, **176**–**179**].

Using QMC simulations of the two-band Holstein model at half-filling, we will address the following questions concerning the effects of interband hybridization t_3: (i) Is there a transition in which CDW order is destroyed as t_3 is increased? What is the value of the critical coupling associated with the quantum critical point (QCP) in the ground state and the critical temperature for the thermal transitions at finite T? (ii) In a situation where the electron-phonon energy scales in the two bands are very different, can CDW order in one band coexist with metallic behavior in the other? These issues are in direct analogy with those addressed in multiband Hubbard Hamiltonians; we will discuss similarities and differences between the resulting phenomena.

7.2. Layered Holstein Hamiltonian

We focus on the bilayer Holstein model

$$\begin{aligned}\hat{\mathcal{H}} = &- \sum_{\langle ij\rangle,l,\sigma} \left(t_l\, \hat{c}^{\dagger}_{il\sigma}\hat{c}_{jl\sigma} + \text{h.c.}\right) - \sum_{i,l,\sigma} \mu_l \hat{n}_{il\sigma} \\ &+ \frac{1}{2M}\sum_{il} \hat{P}^2_{il} + \frac{1}{2}\sum_{i,l} \omega_l^2 \hat{X}^2_{il} + \sum_{i,l,\sigma} \lambda_l\, \hat{n}_{il\sigma}\hat{X}_{il} \\ &- \sum_{i,\langle ll'\rangle,\sigma} \left(t_{ll'}\, \hat{c}^{\dagger}_{il\sigma}\hat{c}_{il'\sigma} + \text{h.c.}\right) . \end{aligned} \tag{7.1}$$

$\hat{c}_{il\sigma}(\hat{c}^{\dagger}_{il\sigma})$ are annihilation (creation) operators for an electron on layer $l(=\pm 1)$, site i with spin σ, and $\hat{n}_{il\sigma} = \hat{c}^{\dagger}_{il\sigma}\hat{c}_{il\sigma}$ is the number operator. t_l and $t_{ll'} = t_3$ denote the intra- and inter-layer hopping respectively. Phonons are represented by local (dispersionless) quantum harmonic oscillators with frequency ω_l, and on-site electron-phonon interaction on layer l is introduced via λ_l. We choose intralayer hopping $t_l = t = 1$ throughout this work to set the energy scale, and all simulations are done at half-filling $\langle \hat{n}_{il} \rangle = 1$, which can be achieved by setting the chemical potential $\mu_l = -\lambda_l^2/\omega_l^2$; phonon mass is set as $M = 1$. Each layer is an $L \times L$ site square lattice, as sketched in Fig. 7.1(a), with $N = 2 \times L \times L$ being the total number of sites. We focus on two cases in this work: a uniform bilayer Holstein model where $t_1 = t_{-1} = t$, $\mu_1 = \mu_{-1} = \mu$, $\omega_1 = \omega_{-1} = \omega$ and $\lambda_{+1} = \lambda_{-1} = \lambda$; and an interface between Holstein layer and "metal" layer, where only layer $l = +1$ has a non-zero electron-phonon coupling $\lambda_{+1} \neq 0$ and layer $l = -1$ has $\lambda_{-1} = 0$. We employ a recently developed Langevin quantum Monte Carlo (QMC) method [**180**] discussed in the next section.

We first define the local observables including the (layer-dependent) double occupancy,

$$\mathcal{D}_l \equiv \langle \hat{n}_{il\uparrow}\hat{n}_{il\downarrow} \rangle \tag{7.2}$$

the near-neighbor intra-layer Green's function,

$$\mathcal{G}_{\langle ij \rangle l} \equiv -\langle \hat{c}^{\dagger}_{il\sigma}\hat{c}_{jl\sigma} + \hat{c}^{\dagger}_{jl\sigma}\hat{c}_{il\sigma} \rangle \,, \tag{7.3}$$

and the near-neighbor inter-layer Green's function,

$$\mathcal{G}_{\langle ll' \rangle} \equiv -\langle \hat{c}^{\dagger}_{il\sigma}\hat{c}_{il'\sigma} + \hat{c}^{\dagger}_{il'\sigma}\hat{c}_{il\sigma} \rangle \,. \tag{7.4}$$

When multiplied by their associated hopping integrals, $t\,\mathcal{G}_{\langle ij \rangle l}$ and $t_3\,\mathcal{G}_{\langle ll' \rangle}$ give the intra- and inter-layer kinetic energies per site.

Two further observables, the density-density and pair-pair correlators, aid in characterizing the excitations between the planes.

$$
\begin{aligned}
d_{-1,1} &\equiv \frac{1}{4}\langle \hat{n}_{i,1}\hat{n}_{i,-1} - 1\rangle \\
p_{-1,1} &\equiv -\frac{1}{4}\langle \hat{\Delta}_{i,1}\hat{\Delta}^{\dagger}_{i,-1} + \hat{\Delta}^{\dagger}_{i,1}\hat{\Delta}_{i,-1}\rangle \\
\hat{\Delta}^{\dagger}_{il} &\equiv \hat{c}^{\dagger}_{il\uparrow}\hat{c}^{\dagger}_{il\downarrow}.
\end{aligned} \tag{7.5}
$$

$d_{-1,1}$ and $p_{-1,1}$ are the analogs of the zz and xy spin correlations which enter into the characterization of interlayer singlet formation in the Hubbard and Heisenberg bilayers, see Sec. 7.5.3. Because of rotational symmetry of those models, their magnetic analogs, obtained by the transformation $\hat{c}_{il\downarrow} \rightarrow \hat{c}^{\dagger}_{il\downarrow}$ are identical in value. $d_{-1,1} = p_{-1,1}$ would also hold in the attractive Hubbard Hamiltonian. Here, in the Holstein model, rotational symmetry is broken and we have $d_{-1,1} \neq p_{-1,1}$. We will discuss the implications further in the sections to follow.

Characterization of the CDW formation in the thermodynamic limit can be made by the analysis of the (layer-resolved) structure factor,

$$
S^{\mathrm{cdw}}_{l} = \frac{2}{N}\sum_{ij}(-1)^{i+j}\langle \hat{n}_{il}\hat{n}_{jl}\rangle, \tag{7.6}
$$

with $\hat{n}_{il} = \sum_{\sigma}\hat{n}_{il\sigma}$. S^{cdw}_{l} samples correlations across the entire lattice, and hence is a primary tool in the determination of long range order.

In the case of the uniform bilayer, the quantities defined in Eqs. 7.2-7.4 and 7.6 are independent of the layer index l, and in this case we suppress this index. But for the 'interface' geometry, which includes one layer with $\lambda_1 \neq 0$ and another with $\lambda_{-1} = 0$, measurements performed on the two layers are inequivalent.

The layer-resolved single-particle spectral function $A_l(\omega)$ is obtained by using the maximum entropy method to invert the integral equation relating the imaginary time dependent

Green's function $G_{i=0}(\tau)$ and $A(\omega)$:

$$G_{i=0}(\tau) = \int d\omega \frac{e^{-\tau\omega}}{1+e^{\beta\omega}} A(\omega)$$

$$G_i(\tau) = \langle c_i(\tau) c_0^\dagger(0) \rangle = \langle e^{\tau\mathcal{H}} c_i(0) e^{-\tau\mathcal{H}} c_0^\dagger(0) \rangle \,. \tag{7.7}$$

τ represents imaginary time; layer and spin indices are omitted here for simplicity. The appropriate local G is used to get $A_l(\omega)$ for the each layer l in the interface geometry.

We advance our key results in Figures 7.1(b) and 7.1(c): (i) At weak t_3 there is a phase transition at finite temperature T_c to a state with long range charge order. In the bilayer case, T_c initially increases with t_3 as the charge order is enhanced by increased coordination number. (ii) At $T = 0$, in both the Holstein bilayer and the Holstein-metal interface, CDW order is destroyed for t_3 exceeding a quantum critical value. (iii) The phase diagram of the interface geometry exhibits an 'orbitally selective CDW phase' (OSCDW) at low T and weak t_3. The specific description of how these phase diagrams are obtained is given in the corresponding section containing the main results of each model.

7.3. Langevin QMC Algorithm

We employ a recently developed Fourier accelerated Langevin quantum Monte Carlo (QMC) method [**180**]. The partition function of the Holstein Hamiltonian is written as a path integral $\mathcal{Z} = Tre^{-\beta\hat{\mathcal{H}}} = Tre^{-\Delta\tau\hat{\mathcal{H}}} e^{-\Delta\tau\hat{\mathcal{H}}} \cdots e^{-\Delta\tau\hat{\mathcal{H}}}$ where the inverse temperature $\beta = L_\tau \Delta\tau$ is discretized along the "imaginary time" axis. Complete sets of phonon eigenstates $|\{x_{i,\tau}\}\rangle$ are inserted at each time slice, allowing the action of the phonon operators to be evaluated. In so doing, we convert the quantum problem into a classical problem in one higher dimension. Since the fermion operators appear only as quadratic forms, we can trace over the associated

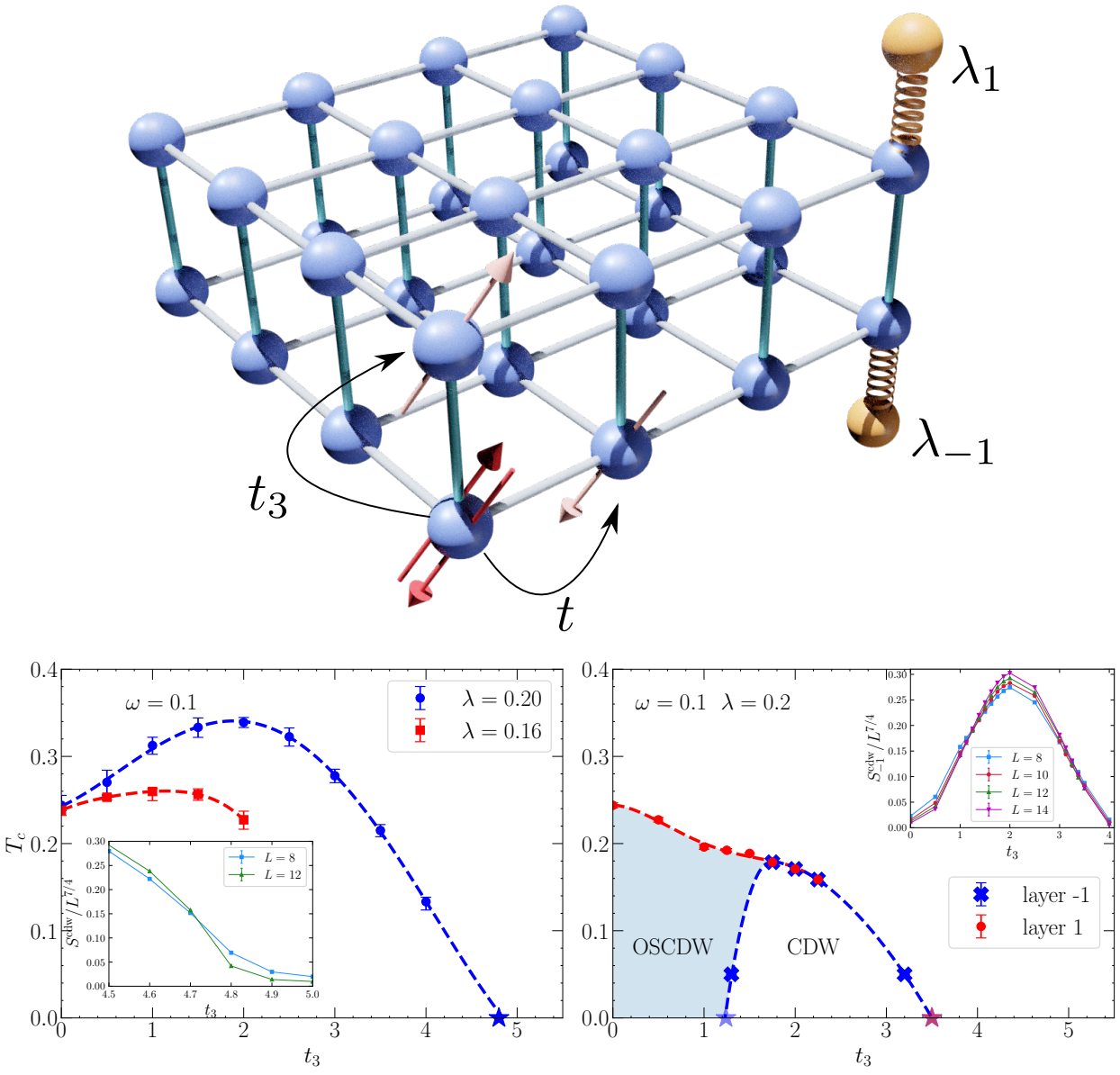

FIGURE 7.1. (a) Sketch of a bilayer with relevant terms in Eq. (7.1) marked. (b) Phase diagram of the Holstein bilayer giving the CDW transition temperature T_c as a function of inter-layer hopping t_3. Two values of electron-phonon coupling, $\lambda = 0.2$ and $\lambda = 0.16$, are shown. Dashed lines are guides to the eye. Inset shows crossing plot of $S^{cdw}/L^{7/4}$ versus t_3 at $\lambda = 0.2$ and low temperature $\beta = 20$. (c) Analog of (b), but for the Holstein-metal interface. Two crossings at $t_3 \sim 1.3$ and $t_3 \sim 3.2$ are revealed in the inset for layer $l = -1$. The CDW phase in this layer is present only in the region between the two crossings. QCPs are marked by stars on x-axis in both panel (b) and (c). Phonon frequency is set at $\omega = 0.1$ for all data.

degrees of freedom, leaving the partition function dependent only on the phonon field $\{x_{i,\tau}\}$,

$$\mathcal{Z} = \int \mathcal{D}x_{i,\tau} e^{-S_{\rm ph}} [\det M(\{x_{i,\tau}\})]^2 = \int \mathcal{D}x_{i,\tau} e^{-S} \,, \tag{7.8}$$

where the "phonon action"

$$S_{\rm ph} = \frac{\Delta\tau}{2} \left[\omega^2 \sum_i x_{i,\tau}^2 + \sum_i \left(\frac{x_{i,\tau+1} - x_{i,\tau}}{\Delta\tau} \right)^2 \right] \tag{7.9}$$

and

$$S = S_{\rm ph} - \ln(\det M)^2 \,. \tag{7.10}$$

Here M is a sparse matrix of dimension NL_τ whose detailed form is given in Ref. [**180**]. The square of the determinant appears because up and down fermionic species have the same coupling to the phonons. As a consequence, there is no sign problem. In order to sample the phonon coordinates, instead of using the usual Metropolis algorithm, we evolve $\{x_{i,\tau}\}$ using the discretized Langevin equation, whose simplest form is given by the first order Euler discretization,

$$x_{i,\tau,t+dt} = x_{i,\tau,t} - dt \frac{\partial S}{\partial x_{i,\tau,t}} + \sqrt{2\,dt}\,\eta_{i,\tau,t} \,, \tag{7.11}$$

where t is the Langevin time, and η is a Gaussian distributed stochastic variable. In practice, in our simulations we make use of a higher order Runge-Kutta discretization [**180**] which reduces the discretization error to $\mathcal{O}(dt^2)$. Throughout this work, the Langevin time step dt is chosen as 0.002, which has been shown to be sufficiently small so that the Langevin time discretization error is the same order, or smaller than, statistical errors in typical simulations [**180**]. It can be demonstrated that, in the stationary limit, this Markov process generates configurations which are drawn from the exponential of the action of Eq. 7.10.

The computational kernel is the calculation of the partial derivatives of the action via

$$\frac{\partial S}{\partial x_{i,\tau,t}} = \frac{\partial S_{\rm ph}}{\partial x_{i,\tau,t}} - 2Tr\frac{\partial M}{\partial x_{i,\tau,t}}M^{-1}, \tag{7.12}$$

where the trace is evaluated using a stochastic estimator [**180**]. Comparing to the conventional determinant quantum Monte Carlo (DQMC) method, which is an $O(N^3L_\tau)$ approach, the Langevin method scales as $O(NL_\tau)$ (although with a larger prefactor, so that there is a cross-over N at which the Langevin approach becomes the more efficient method). This enables simulations to reach considerably larger lattice sizes. In this work, we analyze systems up to $N = 800$ sites. The efficiency of the Langevin approach results from the sparsity of the matrix M and the fact that computing the action of M^{-1} on a vector can be done iteratively in a number of steps which does not grow with N [**180**], with appropriate pre-conditioning. The Langevin dynamics we employ is particularly effective in the adiabatic limit of small phonon-frequencies, where the density of zeros of individual fermion determinants is negligible [**181**]. In what follows we fix $\omega = 0.1$, thus simulations are stable, and statistical convergence is quickly obtained over the course of Markov generation.

7.4. Holstein bilayer

We initially consider two identical layers with $\lambda = 0.2$, $\omega = 0.1$ and the question of the destruction of CDW order via the formation of charge singlets at large interlayer hopping t_3 before tackling the more complex issue of selective CDW transitions.

Figure 7.2(a) gives the CDW structure factor $S^{\rm cdw}$ as a function of t_3 at low temperature for two lattice sizes. Below $t_{3,c} \approx 4.8$, $S^{\rm cdw}$ is large, and grows with lattice size, suggesting long range charge order. Figure 7.2(b) focuses on the interlayer density-density $d_{-1,1}$ and pair-pair $p_{-1,1}$ correlations. For small t_3, only $d_{-1,1}$ is large in magnitude, indicating coherence in the charge order between the two layers. As t_3 increases, intersheet pair correlations $p_{-1,1}$ develop. $d_{-1,1}$ and $p_{-1,1}$ then become nearly degenerate at $t_{3,c}$, signalling the loss of

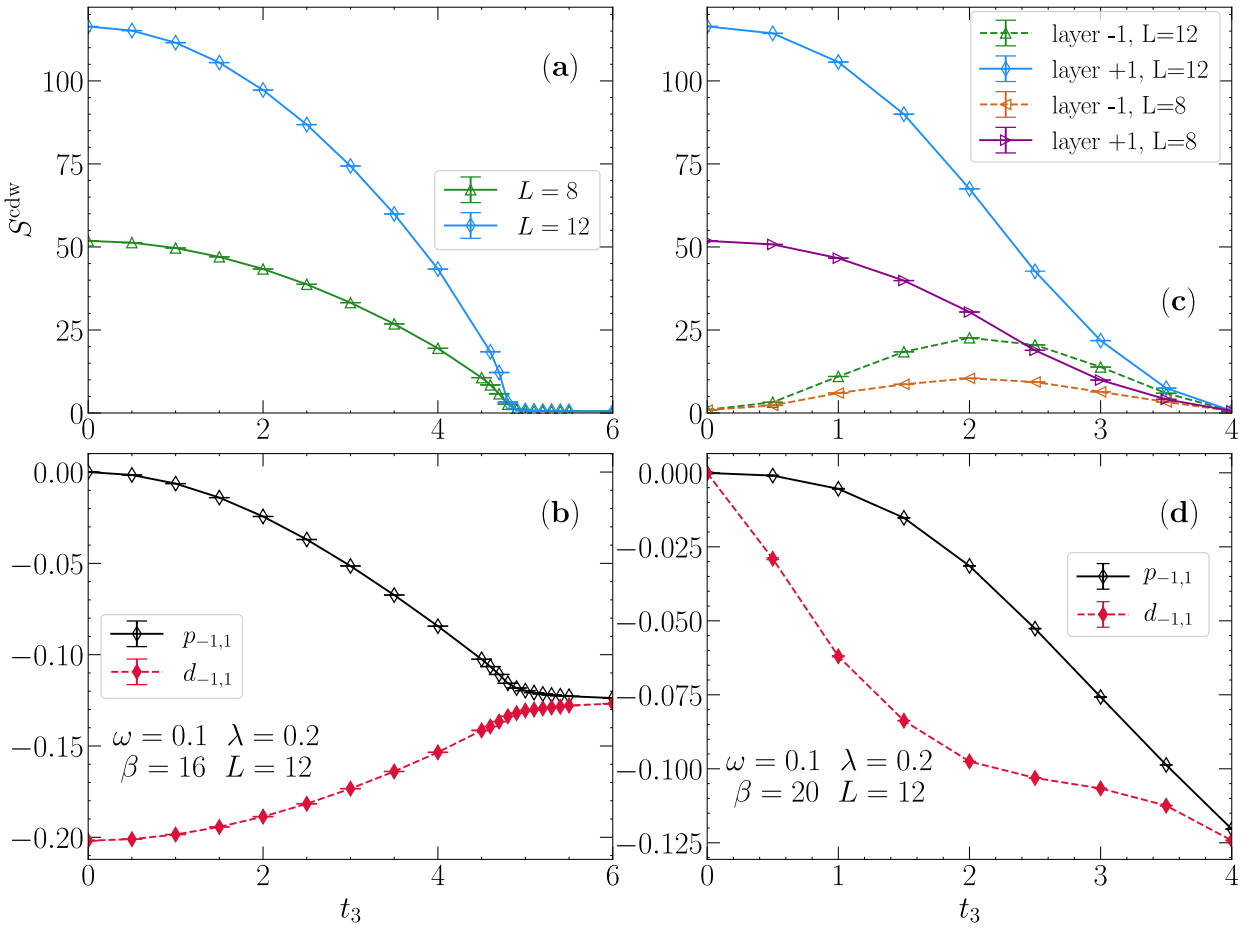

FIGURE 7.2. (a) Charge structure factor $S^{\rm cdw}$; and (b) $p_{-1,1}$ and $d_{-1,1}$ as a function of interlayer hopping t_3 for the Holstein bilayer at low temperature $\beta = 16$ and $\lambda_{+1} = \lambda_{-1} = 0.2$. $S^{\rm cdw}$ shows significant finite size effects in the ordered phase $t_3 \lesssim 4.8$. Note that $d_{-1,1}$ vanishes at $t_3 = 0$, but jumps discontinuously to a non-zero value for infinitesmal t_3. Panels (c,d) are analog of (a,b) for the Holstein-metal interface. The two curves in (c) correspond to layers $l = +1$ and $l = -1$, with $\lambda_{+1} = 0.2$ and $\lambda_{-1} = 0$ respectively and temperature $\beta = 20$. In all plots the phonon frequency is set at $\omega = 0.1$.

CDW order and entry into the 'charge singlet' phase. Together, Figs. 7.2(a) and 7.2(b) motivate the bilayer phase diagram of Fig. 7.1(b).

Although the QCP in this Holstein bilayer is closely analogous to that occurring in Hubbard and Heisenberg bilayers as well as the periodic Anderson model, in those cases the electron-electron interaction gives rise to magnetic phases which form due to the breaking

of a *continuous* spin symmetry. Thus in 2D and quasi-2D geometries, no long range order is possible at finite T. In contrast, here for the Holstein model, charge and pairing order are not degenerate, as emphasized by the data of Fig. 7.2(b). CDW correlations dominate at half-filling and a finite temperature phase transition can occur, terminating at a QCP as shown in Figs. 7.1(b) and 7.1(c). This distinction means that, in principle, our characterization of the unordered phase as a 'charge singlet' is somewhat loose: in the usual spin singlet the x, y, z components of the spin-spin correlations on the two layers (or in the two orbitals) are equal. With that said, the equivalence of $p_{-1,1}$ and $d_{-1,1}$ in the large t_3 regime points to an emergent restoration of the symmetry (see Sec. 7.5.3). It is worth noting that in the absence of t_3, e.g. in the 2D Holstein model, this restoration does not occur until the anti-adiabatic limit is reached, which requires very large values of ω [**10**].

Figure 7.3 provides details of the behavior of the CDW structure factor. The top panel (a) gives raw values for S^{cdw} as a function of β at $t_3 = 2$ for different lattice sizes. At low β (high temperature), the correlation length ξ is short and S^{cdw} is independent of L. As β increases, so does ξ and when $\xi \sim L$, S^{cdw} becomes sensitive to L. This separation of the curves provides a crude estimate for β_c, which may then be determined precisely by finite size scaling (FSS).

In particular, in the vicinity of the critical temperature T_c, the CDW structure factor measured on finite lattices of linear dimension L should obey,

$$S^{\mathrm{cdw}} \sim L^{\gamma/\nu} f\left(\frac{T - T_c}{T_c} L^{1/\nu}\right) . \tag{7.13}$$

As a consequence, when plotting $S^{\mathrm{cdw}}/L^{\gamma/\nu}$ as a function of the inverse temperature β, different sizes L cross at $\beta = \beta_c$ [Fig. 7.3 (b)]. Following the scaling form given in Eq.(7.13) we note that when plotted against $(\beta - \beta_c)L^{1/\nu}$ all data collapse on a single curve – see Figs. 7.3(c) (and later for the Holstein-metal interface in Fig. 7.5). In this analysis we have used the critical exponents of the 2D Ising universality class ($\gamma = 7/4$ and $\nu = 1$), since

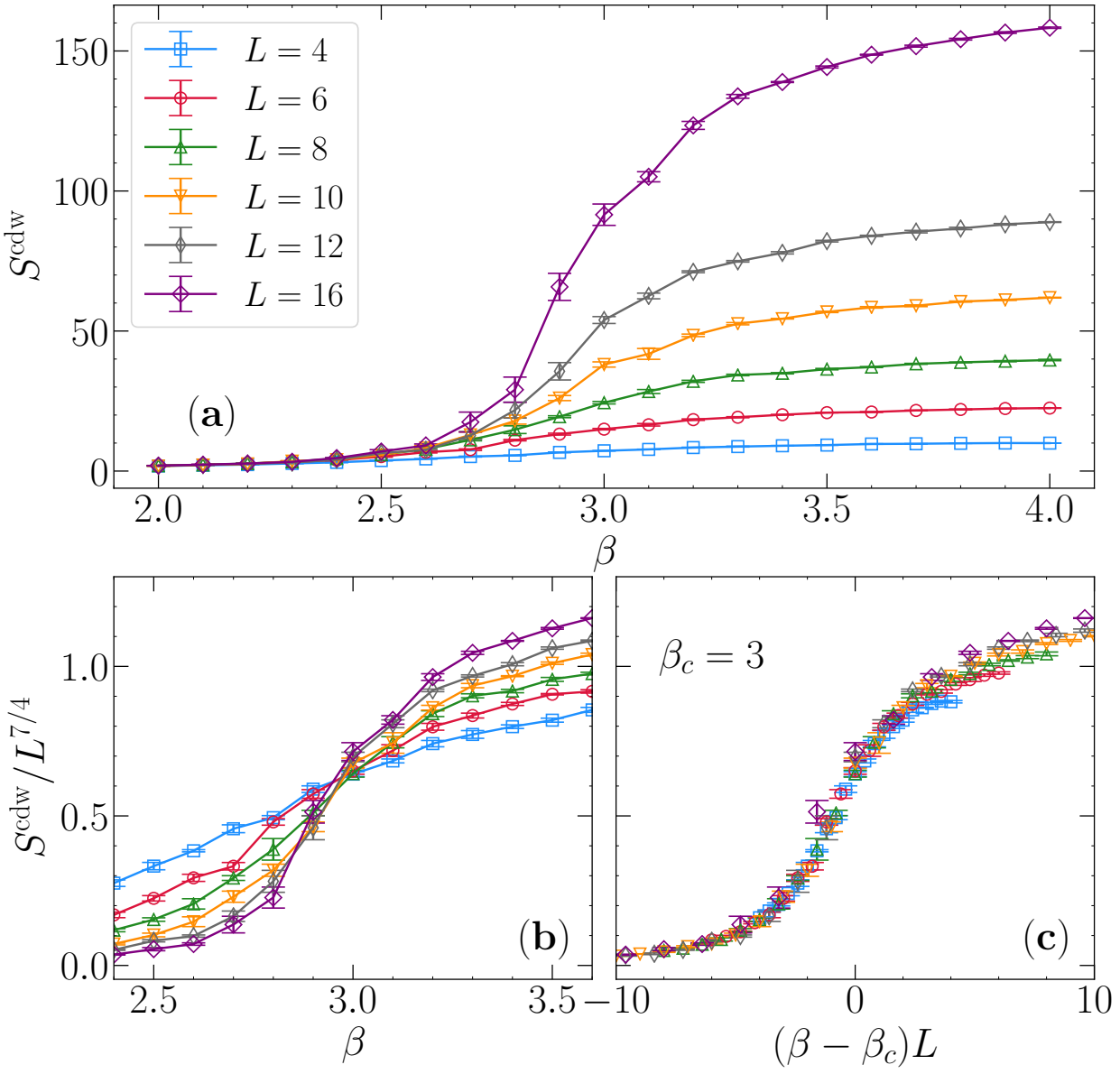

FIGURE 7.3. (a) CDW structure factor S^{cdw} dependence on the inverse temperature β and finite size scaling of the Holstein bilayer at $t_3 = 2$. Both the crossing plot (b), and the full data collapse (c) using 2D Ising critical exponents and $\beta_c \simeq 3.0$.

the CDW phase breaks a Z_2 symmetry. A discussion of the degree to which the collapse worsens, and hence the accuracy with which the exponents can be determined, is given in the Sec. 7.5.4.

Using such scaling procedure for various values of the interplane hybridization, allows us to extract the location of the thermal transition, as compiled in Fig. 7.1(b), using two values of the electron-phonon interaction. In this geometry, the critical temperature T_c initially increases as a consequence of the larger coordination number when the planes are coupled - the 2D to 3D crossover. However, at large t_3 the critical temperature decreases and ultimately vanishes at a quantum critical point.

7.5. Results

7.5.1. Holstein-Metal interface

We next consider the 'Holstein-metal interface' in which layer $l = +1$ has nonzero λ_{+1} but $\lambda_{-1} = 0$. The two layers are in contact via hybridization. Here, in addition to the question of charge singlet formation at large t_3, quenching CDW order, a different fundamental question arises: to what extent do CDW correlations in layer $l = +1$ 'penetrate' into layer $l = -1$, and, conversely, is the CDW in layer $l = +1$ disrupted by contact with the 'metallic' layer? We choose $\lambda = 0.2$ and $\omega = 0.1$ as in the previous section.

Figure 7.2(c) shows the CDW structure factor $S^{\rm cdw}$ in the two layers. $S^{\rm cdw}_{+1}$ decreases steadily with t_3: additional quantum fluctuations associated with contact with the metal reduce charge order. In contrast, $S^{\rm cdw}_{-1}$ is non-monotonic: charge order is initially induced in the metal via contact with the Holstein layer, but ultimately large t_3 is inimical to it. The behavior of $S^{\rm cdw}_{-1}$ provides a first clue that order in layer $l = -1$ might occur only for intermediate t_3. Figure 7.2(d) gives the interlayer density-density $d_{-1,1}$ and pair-pair $p_{-1,1}$ correlations for this interface geometry. The primary difference from the original bilayer case is the gradual development of $d_{-1,1}$ with t_3. This is a consequence of the absence of CDW in the metal layer when t_3 vanishes. The interlayer hopping thus must not only couple the charge correlations, but also induce them in layer $l = -1$. Similar to the bilayer case, $d_{-1,1}$ and $p_{-1,1}$ become degenerate for large t_3. This is again a signature of entering into the charge singlet phase.

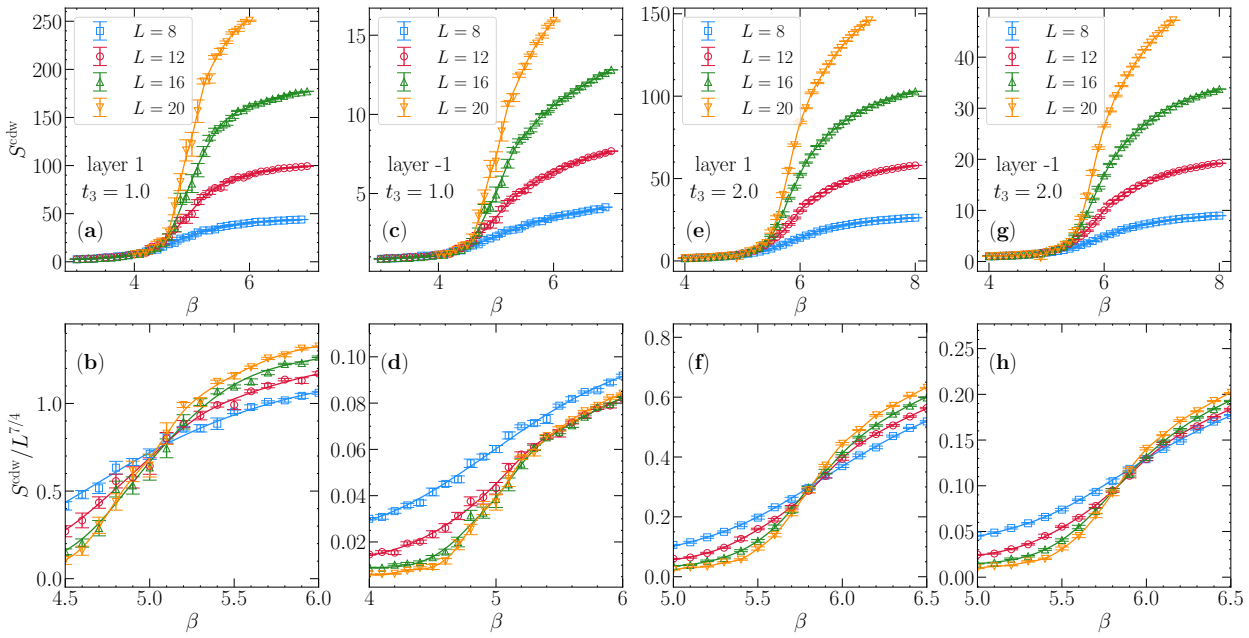

FIGURE 7.4. (a) CDW structure factor, $S^{\rm cdw}$, dependence on the inverse temperature, β, for layer $l = 1$ of the Holstein interface at $t_3 = 1$; (b) using 2D Ising critical exponents for finite size scaling (FSS). Panels (c) and (d) display the same but for the metallic layer $l = -1$. Panels (e–h) display the corresponding data for $t_3 = 2$. FSS in (f) and (h) show the same critical temperature for both layers at $t_3 = 2$, in contrast to $t_3 = 1$, where layer $l = +1$ (b) exhibits a clear CDW transition whereas data for layer $l = -1$ (d) does not exhibit crossing when using Ising critical exponents.

We now turn to a more careful FSS study of the layer-resolved $S^{\rm cdw}_l$. Our main interest is in determining how long range order in the two layers evolves with t_3. Figure 7.4 displays a detailed analysis of two representative values, $t_3 = 1$ and $t_3 = 2$. The former is a case when $S^{\rm cdw}_{-1}$ is just beginning to develop, and the latter is when $S^{\rm cdw}_{-1}$ has reached its maximal induced value [see Fig. 7.2(c)]. There is a superficial resemblance in the unscaled data for both values of t_3, which rise as the temperature is lowered (β increases) and also increase with system size. A proper scaling analysis, however, reveals a profound distinction. As seen in Figs. 7.4(b) and 7.4(f), for both values of t_3, the layer $l = +1$ with non-zero electron-phonon coupling $\lambda_{+1} = 0.2$, has a scaled structure factor $L^{-7/4} S^{\rm cdw}_{+1}$ which exhibits a sharp crossing, indicating a finite temperature transition to long range CDW order. When $t_3 = 2$,

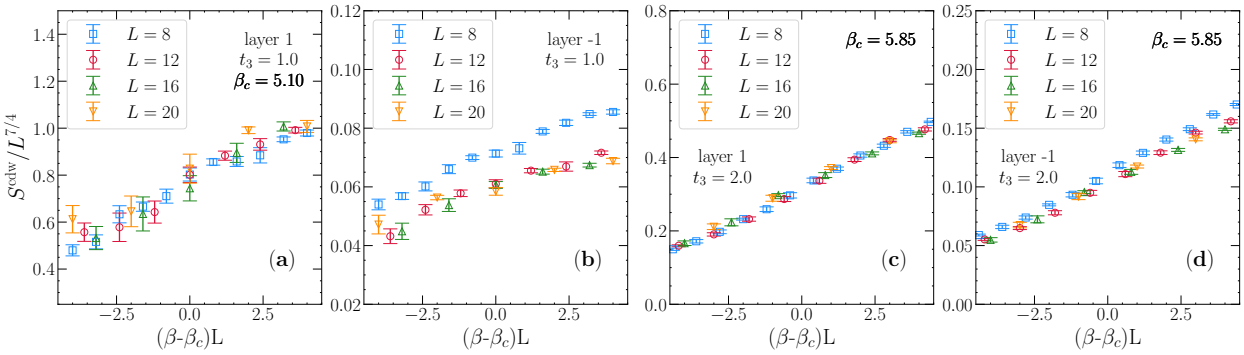

FIGURE 7.5. Full data collapse of the scaled CDW order parameter versus scaled reduced temperature in the 'Holstein interface' system. Only the Holstein layer (layer 1) shows a single universal curve for $t_3 = 1$ (a), while both collapse for $t_3 = 2t$ (panels b,d).

this crossing occurs for the metallic layer with $\lambda_{-1} = 0$ as well [Fig. 7.4(h)]. However, when $t_3 = 1$ the data for the metallic layer do not cross for the studied system sizes [Fig. 7.4(d)], namely $L = 8$-20 for both t_3 values: The $L = 12$,16 and 20 curves converge at $\beta > 5.4$ instead of crossing. The $L = 8$ data do not scale with the other lattice sizes at all. This distinction becomes even more apparent in Fig. 7.5, where a simultaneous data collapse for the scaled structure factor can be made possible at the same temperature for $t_3 = 2$, while it is unattainable for $t_3 = 1$.

We conclude that for $t_3 = 2$, the interface geometry has CDW order in both layers, with long range correlations in the metallic layer induced by proximity to the Holstein layer. For $t_3 = t$, the interface geometry exhibits *orbital selective* CDW order- the metal remains with only short range correlation despite its hybridization to the long range CDW layer. We emphasize that this conclusion is reinforced by the data in the inset to Fig. 7.1(b), where a low temperature ($\beta = 20$) sweep of the scaled S^{cdw} with t_3 has a pair of crossings $t_3 \sim 1.3$ and $t_3 \sim 3.2$. Long range CDW order exists in layer $l = -1$ only between these values.

7.5.2. Spectral Functions and Double Occupancies

Having examined structure factors and inter-layer correlators, we now turn to the spectral functions and the double occupancies, both of which provide additional insight into the

ground state properties. The layer-resolved spectral functions $A_l(\omega)$, shown in Fig. 7.6, the many-body analog of the single particle density of states, provide confirming evidence for the Holstein interface phase diagram of Fig. 7.1(c). In the top row, for small t_3, the Holstein layer $l = +1$ exhibits a CDW gap. The gap at $t_3 = 0$ is large; Hybridization with the metal produces peaks closer to $\omega = 0$, but a smaller gap remains. On the other hand the metal layer $l = -1$ has finite Fermi surface spectral weight $A_{-1}(\omega = 0) \neq 0$, thus showing the OSCDW. In the middle row, for intermediate t_3, both layers have a gap, consistent with the measurement of simultaneous long range CDW order. Finally, in the bottom row, for large t_3, both layers have finite Fermi surface spectral weight $A_l(\omega = 0) \neq 0$ for $l = +1, -1$. The system is in the charge singlet (charge liquid) phase.

We note that although the bilayer and interface geometries have many properties in common at large t_3, their spectral functions are different. There is a gap in the bilayer case, but not for the interface. We have verified, with separate exact diagonalization calculations, that for dimers (i.e. $t_3 \gg t$) with $\lambda_{+1} = \lambda_{-1}$ one finds $A(\omega)$ is gapped, while when λ_{+1} is nonzero $\lambda_{-1} = 0$ one reproduces the behavior shown in Fig. 7.6(c,f).

In a perfect CDW phase, half of the sites are doubly occupied and half are empty, and $\mathcal{D} = 0.5$. In the absence of interactions, $\lambda = 0$, all four site occupation possibilities $|0\rangle$, $|\uparrow\rangle$, $|\downarrow\rangle$, and $|\uparrow\downarrow\rangle$, are equally likely and $\mathcal{D} = 0.25$. This is also the case in the charge singlet phase. Figure 7.7 shows $\mathcal{D}$ as a function of t_3. Panel (a) is for the bilayer, where $\mathcal{D}_{+1} = \mathcal{D}_{-1}$, and panel (b) for the interface geometry where the two are inequivalent. In both cases, $\mathcal{D}_{+1}$ is seen to evolve between the CDW and singlet limits, although it never attains the value $\mathcal{D} = 0.5$ owing to the presence of quantum fluctuations. For the interface, $\mathcal{D}_{-1}$ begins at the uncorrelated value, $\mathcal{D}_{-1} = 0.25$ at $t_3 = 0$ since $\lambda_{-1} = 0$. The double occupancy evolution is quite similar to that of the structure factor, Fig. 7.2(a,c). However, since $\mathcal{D}$ is a local observable, it exhibits less sharp features than S^{cdw} in the vicinity of the QCP and thus only provides qualitative evidence for a cross-over between those two phases.

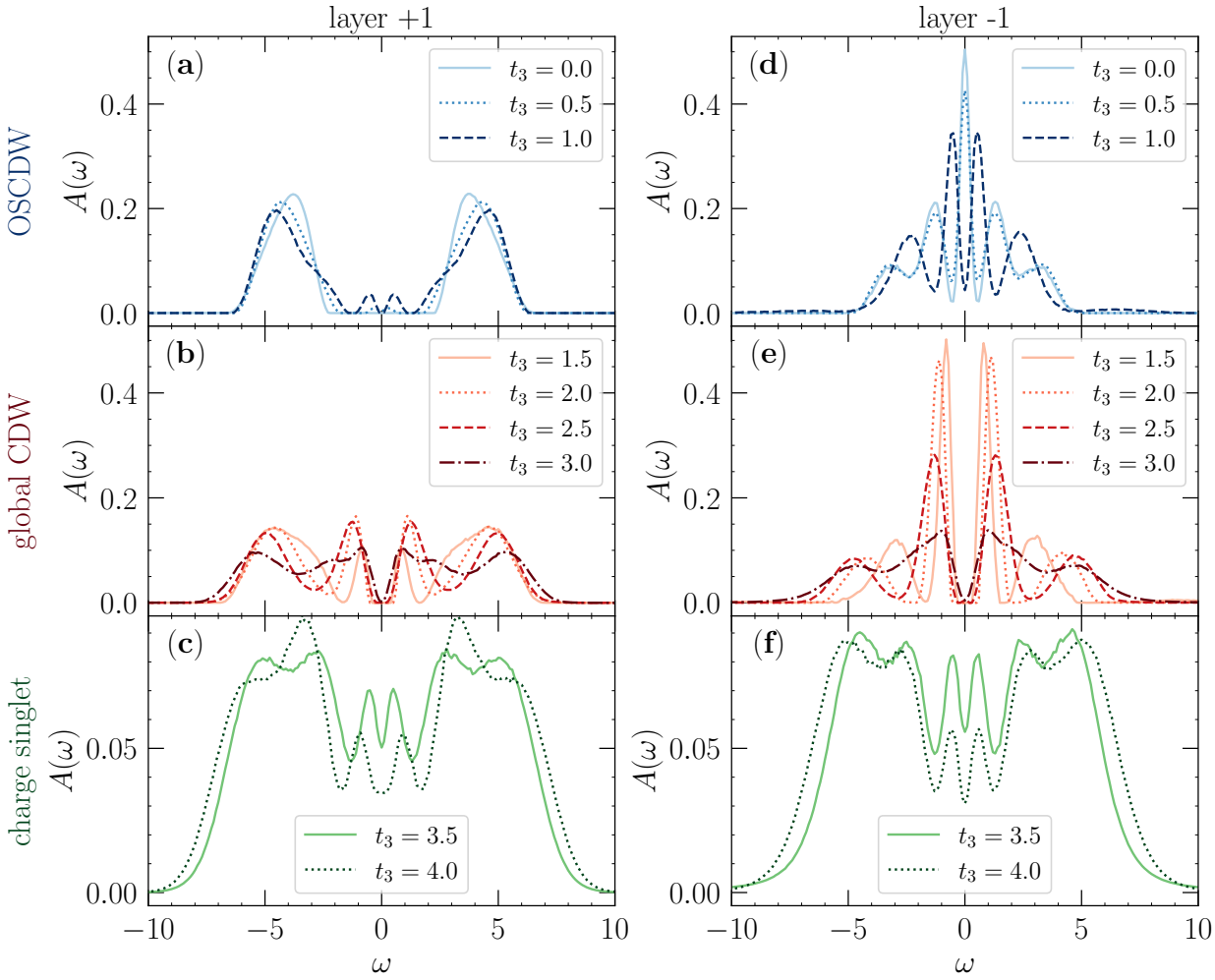

FIGURE 7.6. Spectral function $A(\omega)$ at $\beta = 12$ for several t_3 values cutting across the Holstein-metal interface phase diagram of Fig. 7.1. Top: Small t_3. Middle: Intermediate t_3. Bottom: Large t_3. Left and right columns correspond to Holstein and metallic layers $l = +1$ and $l = -1$ respectively.

Besides that, a simple model which exhibits a layer-dependent trivial CDW formation with only electronic degrees of freedom, a bilayer ionic model, already displays this characteristic non-monotonicity with growing hybridization (see Sec. 7.5.5).

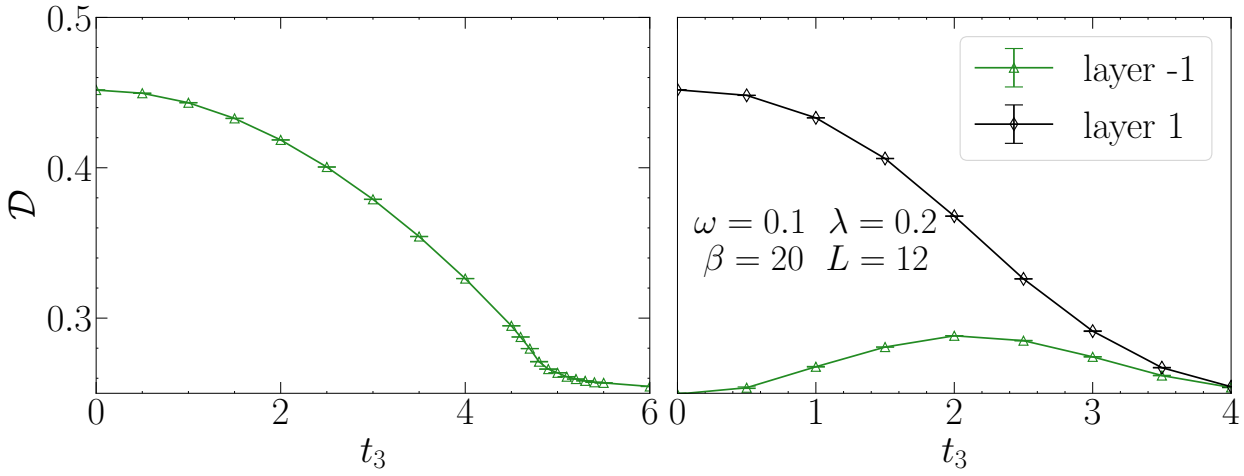

FIGURE 7.7. Double occupancy D shown as a function of interlayer hopping t_3 at low temperature $\beta = 20$. D is a local observable, and its value is the same for $L = 8$ and $L = 12$ to within the symbol size; we show the latter. (a) Holstein bilayer; (b) Holstein-metal interface. In (a) the two layers are equivalent and a single curve is shown. In (b) the green curve shows data on layer $l = -1$, whereas the grey curve represents layer $l = +1$.

7.5.3. Connection to Magnetic Language

In the repulsive 2D Hubbard model the dominant physics at half-filling on a bipartite lattice is anti-ferromagnetic order, characterized by the operators,

$$\begin{aligned}
\hat{S}^j_x &= \frac{1}{2}\left(\hat{S}^j_+ + \hat{S}^j_-\right) = \frac{1}{2}\left(\hat{c}^\dagger_{j\uparrow}\hat{c}_{j\downarrow} + \hat{c}^\dagger_{j\downarrow}\hat{c}_{j\uparrow}\right) \\
\hat{S}^j_y &= \frac{1}{2i}\left(\hat{S}^j_+ - \hat{S}^j_-\right) = \frac{1}{2i}\left(\hat{c}^\dagger_{j\uparrow}\hat{c}_{j\downarrow} - \hat{c}^\dagger_{j\downarrow}\hat{c}_{j\uparrow}\right) \\
\hat{S}^j_z &= \frac{1}{2}\left(\hat{n}_{j\uparrow} - \hat{n}_{j\downarrow}\right) = \frac{1}{2}\left(\hat{c}^\dagger_{j\uparrow}\hat{c}_{j\uparrow} - \hat{c}^\dagger_{j\downarrow}\hat{c}_{j\downarrow}\right)
\end{aligned} \tag{7.14}$$

From these relations, and as a consequence of the spin SU(2) symmetry of the Hubbard model,

$$\begin{aligned}
\langle \hat{S}^j_+ \hat{S}^i_- + \hat{S}^j_- \hat{S}^i_+ \rangle &= 4 \langle \hat{S}^j_z \hat{S}^i_z \rangle \\
\langle\, \hat{c}^\dagger_{j\uparrow} \hat{c}_{j\downarrow} \hat{c}^\dagger_{i\downarrow} \hat{c}_{i\uparrow} + \hat{c}^\dagger_{j\downarrow} \hat{c}_{j\uparrow} \hat{c}^\dagger_{i\uparrow} \hat{c}_{i\downarrow} \,\rangle &= \\
&\langle \,\big(\, \hat{c}^\dagger_{j\uparrow} \hat{c}_{j\uparrow} - \hat{c}^\dagger_{j\downarrow} \hat{c}_{j\downarrow} \,\big)\big(\, \hat{c}^\dagger_{i\uparrow} \hat{c}_{i\uparrow} - \hat{c}^\dagger_{i\downarrow} \hat{c}_{i\downarrow} \,\big) \,\rangle
\end{aligned} \tag{7.15}$$

If we perform a particle-hole transformation to the down spin fermions,

$$\begin{aligned}
\hat{c}^\dagger_{j\downarrow} &\;\rightarrow\; (-1)^j \hat{c}_{j\downarrow} \\
\hat{n}_{j\downarrow} &\;\rightarrow\; \big(1 - \hat{n}_{j\downarrow}\big) \\
\hat{S}^j_+ = \hat{c}^\dagger_{j\uparrow} \hat{c}_{j\downarrow} &\;\rightarrow\; (-1)^j \hat{c}^\dagger_{j\uparrow} \hat{c}^\dagger_{j\downarrow} \equiv (-1)^j \hat{\Delta}^\dagger_j \\
\hat{S}^j_z = \frac{1}{2}\big(\, \hat{n}_{j\uparrow} - \hat{n}_{j\downarrow} \,\big) &\;\rightarrow\; \frac{1}{2}\big(\, \hat{n}_{j\uparrow} + \hat{n}_{j\downarrow} \,\big) \equiv \hat{n}_j
\end{aligned} \tag{7.16}$$

we conclude that,

$$-\langle \hat{\Delta}^\dagger_j \hat{\Delta}_i + \hat{\Delta}_i \hat{\Delta}^\dagger_j \rangle = \langle \big(\, \hat{n}_j - 1) \,\big)\big(\, \hat{n}_i - 1) \,\big) \rangle \tag{7.17}$$

assuming that sites i and j are on opposite sublattices.

If, finally, assuming we are at half-filling, so that $\langle \hat{n}_j \rangle = 1$,

$$-\langle \hat{\Delta}^\dagger_j \hat{\Delta}_i + \hat{\Delta}_i \hat{\Delta}^\dagger_j \rangle = \langle \hat{n}_j \hat{n}_i - 1 \rangle \tag{7.18}$$

This shows that the two correlation functions of Eq. 7.5 are equal: $p_{1,-1} = d_{1,-1}$. The merging of the two curves of Fig. 7.2(c,d) at a common value reflects a restoration of an SU(2) symmetry of the Hubbard model. It is interesting that this occurs even though the correlators are not in the singlet limit of $-1/4$ (due to the fact that we are not in Holstein analog of the large U limit).

7.5.4. Extracting the critical exponents

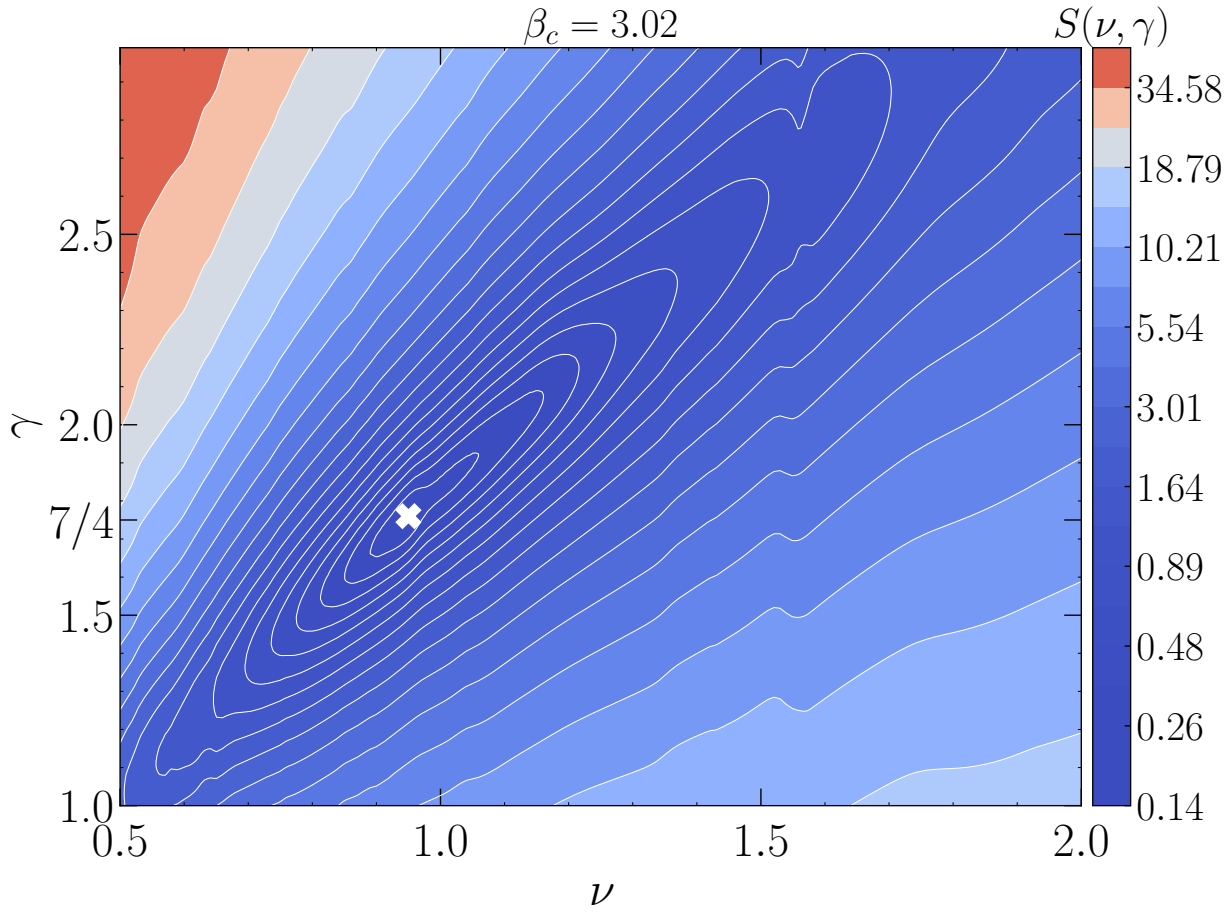

FIGURE 7.8. Contour plot of the sum of squared residuals of the least-squares fit $S(\nu, \gamma)$ of the scaled data for the CDW structure factor S^{cdw} of the Holstein bilayer at $t_3 = 2$ (see Fig. 7.3 for the original data). A 16-th order polynomial is used to fit the dataset, and the critical inverse temperature used is $\beta_c = 3.02$. The white marker denotes the minimum $S(\nu, \gamma)$ in the displayed range of ν and γ.

We argue that owing to the symmetry of the order parameter of the CDW phase, we make use of the critical exponents pertaining to the 2D Ising universality class in order to simplify the FSS of the CDW structure factor S^{cdw}. Here, we justify this choice by quantitatively extracting the best set of exponents ν and γ that scales the curves according to the functional form in Eq. 7.13. We start by using the scaled data in a large range of critical exponents;

subsequently, for each pair of (ν, γ), we proceed with a high-order polynomial fitting of the scaled data, storing the residual $S(\nu, \gamma)$ of the fitting procedure. The set of exponents that minimizes $S(\nu, \gamma)$ is taken as those that characterize the transition. The rationale is that if the dataset is well collapsed for a given (ν, γ), a high-order polynomial fit (with the number of degrees of freedom much smaller than the number of data points) will turn out to have a fairly small error.

Using this procedure, we show in Fig. 7.8 the contour plot $S(\nu, \gamma)$ for the data corresponding to the Holstein bilayer at $t_3 = 2$ See Fig. 7.4(f,h) and Fig. 7.5(c,d). The minimum residual is annotated by the white marker. By observing its variation with slightly different critical inverse temperature β_c, and different polynomial orders used in the fits, we estimate $\nu = 0.95 \pm 0.07$ and $\gamma = 1.7 \pm 0.1$, remarkably close to the 2D Ising exponents $\nu_{\text{2D Ising}} = 1$ and $\gamma_{\text{2D Ising}} = 7/4$.

7.5.5. Induced CDW in Ionic Hubbard Model

We can get additional insight into the Holstein interface by considering the following noninteracting, spinless, tight binding Hamiltonian,

$$\begin{aligned}\hat{\mathcal{H}}_{\text{BI-M}} = &- t \sum_{\langle ij \rangle, l} \left(\hat{c}^\dagger_{i,l} \hat{c}_{j,l} + \text{h.c.} \right) + \delta \sum_i (-1)^i \hat{n}_{i,1} \\ &- t_3 \sum_j \left(\hat{c}^\dagger_{j,1} \hat{c}_{j,-1} + \text{h.c.} \right). \end{aligned} \tag{7.19}$$

Equation 7.19 describes two bands, labeled by $l = \pm 1$, each with hopping t on a 2D square lattice, which are hybridized with each other by t_3. Band $l = -1$ is metallic. At $t_3 = 0$ it has the usual 2D dispersion relation $\epsilon(k) = -2t \left(\cos k_x + \cos k_y \right)$. Band $l = +1$ is made insulating by the staggered potential δ, so that at $t_3 = 0$ its dispersion relation has two branches, $E_\pm(k) = \pm\sqrt{\epsilon(k)^2 + \delta^2}$. Both bands of Eq. 7.19 are half-filled (the chemical potential $\mu = 0$).

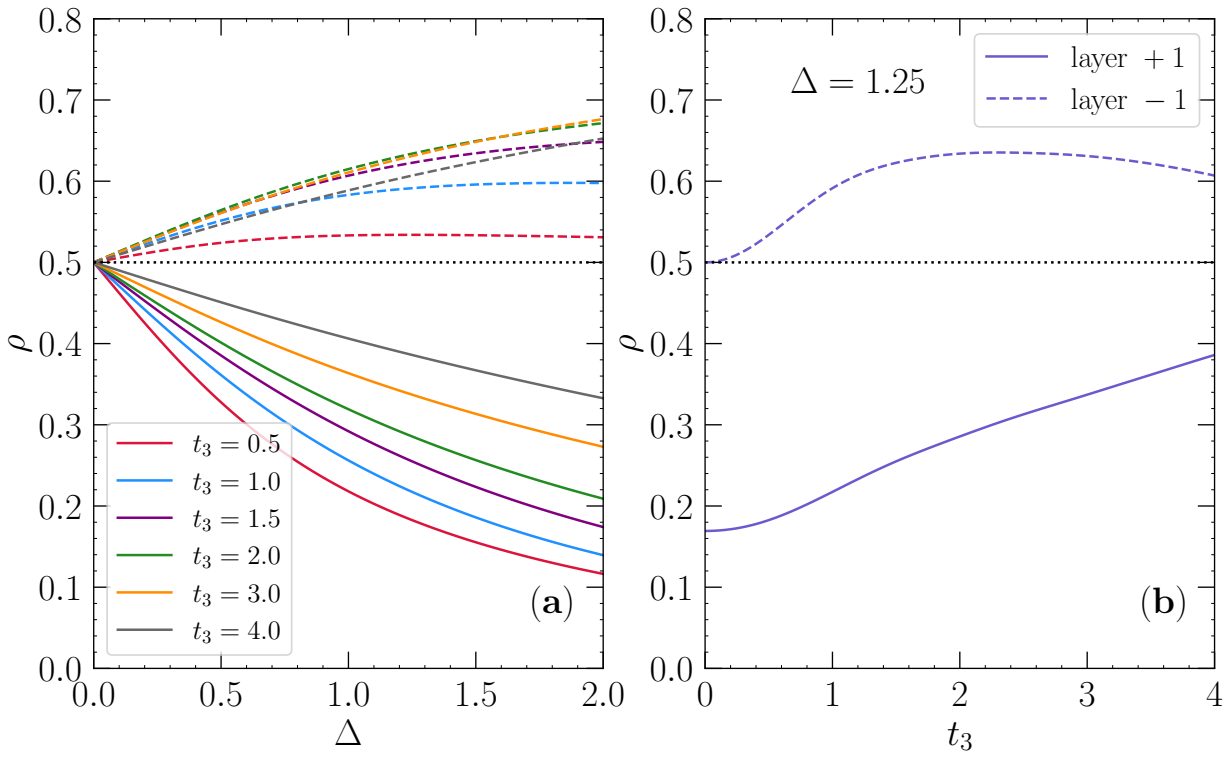

FIGURE 7.9. Solution of the tight binding Hamiltonian, Eq. 7.19. (a) Solid curves Occupations ρ on the $+\delta$ sites of the insulating band as functions of the magnitude of the staggered potential δ; dashed curves: Occupations on the partner sites in the metallic band to which those $+\delta$ sites are hybridized by t_3. (b) Solid Curve: Occupations on the $+\delta$ sites of the insulating band as a function of interlayer hybridization t_3. Dashed curves: Occupations on the partner sites in the metallic band to which those $+\delta$ sites are hybridized by t_3. The staggered potential in this case is $\delta = 1.25$. In both panels the linear lattice size and the inverse temperature are $L = 12$ and $\beta = 4$, respectively.

In addition to inducing a band gap 2δ in layer $l = +1$, the staggered potential also creates a CDW phase, with low occupancy $+\delta$ and high occupancy $-\delta$ sites. Here, the CDW order is trivial, in the sense of being induced by an external field, as opposed to arising spontaneously in a symmetric Hamiltonian like the Holstein model. Nevertheless we can still examine how this 'artificial' CDW in layer $l = +1$ affects the site occupations in the metallic band $l = -1$.

Figure 7.9(a) gives the occupations on the $+\delta$ sites of band $l = +1$ as functions of δ for different t_3. As δ grows, the occupation of the high energy sites in layer $l = +1$, which are

directly coupled to the staggered field, get increasingly small (solid curves). In turn, the occupations of the partner sites on layer $l = -1$ which are *not* coupled to δ are also shifted from $\rho = \frac{1}{2}$. These occupations increase in order to take advantage of the decrease in the Pauli blocking. What is interesting in the context of the simulations of the Holstein bilayers in the main part of this chapter is that, while the layer $l = +1$ occupations steadily return to half-filling with increasing t_3, the evolution of the layer $l = -1$ occupations is instead *non-monotonic*. The deviations of the occupations from half-filling first grow with t_3, but then shrink.

This non-monotonicity is seen more clearly in Fig. 7.9(b) which plots similar occupations as a function of t_3 for a fixed δ. The maximum at intermediate $t_3 \sim 2.28$ is reminiscent of the behavior of Fig. 7.2(c), which similarly shows a maximum in the induced CDW order at intermediate t_3 in the metallic layer of the Holstein interface model. Indeed, the agreement between the values of t_3 at which the induced order is maximal is remarkably *quantitative*. To within error bars, the positions of the maxima are the same, although the fall-off at large t_3 is more gradual in the BI-Metal interface case.

CHAPTER 8

Conclusions

In this thesis, we presented our Mean Field Theory (MFT) and Quantum Monte Carlo (QMC) results on several different geometries which explore the effect of non-uniform hopping, and flat electronic band on Holstein phonons and the competition between electron-electron and electron-phonon interactions on a square lattice. Chapter 1 gives an introduction to the physics of electron-electron and electron-phonon interactions. Next, we discussed the iconic models, the Hubbard, Holstein and SSH, people widely use to explore these two interactions. The methods we used, MFT, Determinant and Langevin QMC are discussed in Chapter 3. A basic unifying theme of this thesis is the extension of studies of electron-electron interactions in various contexts to the less studied realm of electron-phonon interactions.

In Chapter 4 we have presented Determinant Quantum Monte Carlo results for the Holstein model with modulated hopping on a 'decorated honeycomb lattice' which consists of a collection of weakly coupled hexagons, or, in the opposite limit of the relative hybridizations, weakly coupled dimers. Our key result was the determination of the evolution of the charge density wave order as one moves away from uniform hopping towards either of these extremes. This work represents an extension of investigations of the competition between magnetically ordered and spin liquid phases in decorated Hubbard Hamiltonians, to CDW to charge singlet transitions in electron-phonon models. The effect of $t_{x,y} = (1 \pm \Delta)$ on S_{cdw} has also been recently studied in the anisotropic square lattice Holstein Hamiltonian [**11**]. However, in this case the modulation endpoints $\Delta = -1, +1$ are decoupled, but still infinite, linear chains. In the present work the endpoints $\Delta = -1, +0.5$ result in small independent

clusters. As a result of infinite clusters still being present, long range order is somewhat more robust to modulation in the square lattice case.

The geometry we investigated has been proposed as a possible realization of a $\mathcal{Z}_2$ topological state associated with the 'artificial orbitals' of the independent hexagons. As discussed in [**80**], it might be possible to implement this geometry via the placement of a triangular lattice of CO molecules on a Cu(111) surface. Our work has shown that in addition to topological properties, electron-phonon interactions can show a diverse set of charge ordering behavior on such lattices.

The strong breaking of the pairing-charge degeneracy distinguishes the present work from previous magnetic analogs. Specifically, what we demonstrate here is that despite the lack of 'rotational' symmetry, local objects which have (imperfect) singlet character nevertheless still form on the strong bonds, and these ultimately lead to a loss of CDW order. This non-trivial result could not be anticipated by magnetic analogs where rotational symmetry is always exact.

In Chapter 5, We have studied the charge density wave transition for the Holstein model on a Lieb lattice. Our interest was in establishing results for the effect of compact localized states (flat bands) on ordered phases driven by the electron-phonon interaction, in analogy with the body of work which exists for electron-electron interactions (primarily the Hubbard model). The behavior of the occupation, double occupation, spectral function, and charge structure factor have been obtained quantitatively, and used to infer a phase diagram of critical temperature versus coupling constant.

In Chapter 6, we used DQMC simulations to map out the phase diagram of the single orbital square lattice optical SSHH model. Our work fills in the full two dimensional phase diagram in the plane of positive U and g, hitherto only investigated along the $U = 0$ and $g = 0$ axes. The phase diagram is characterized by BOW and AF phases. At larger electron-phonon

coupling strength, the x-y symmetry is spontaneously broken and the system develops a BOW with a (π, π) order. Given the different broken symmetries in the BOW and AF phases, and the sharp increase of BOW structure factor, the results indicate a first-order transition between these two phases. The most salient feature is that the ground state phase transition is much more sensitive to changes in electron-phonon coupling compared to variations in the Coulomb repulsion. We interpret this as the result of the lack of a direct competition between the two ordered phases. In the Hubbard-Holstein model, U suppresses double occupancy while the Holstein g enhances it. Thus the two interactions always conflict: they want the most fundamental structure, the site occupations, to behave completely differently yielding $U_c \sim g^2$ (at $\omega_0 = 1$). No such competition appears in the SSHH model. Indeed, both interactions individually give rise to AF order leading to somewhat cooperative tendencies. We thus argue that this is why adding U does not significantly inhibit the formation of the BOW phase by the SSH phonons, leading to a near vertical phase boundary.

In the AF region, for small electron-phonon coupling g, all the quantities that we analyzed, e.g. the AF structure factor, kinetic energy, phonon displacement and double occupancy, remain approximately constant. For $g \gtrsim 0.2$, the double occupancy and the magnitude of the kinetic energy start increasing, while the AF structure factor decreases. This occurs even though the system still possesses true long range AF order as demonstrated by a finite size scaling analysis [**182**]. This is due to the fact that the Hubbard AF and the SSH AF mechanisms are different [**48**, **49**]. This new insight into the physics of the SSH-Hubbard Hamiltonian can be thought of as analogous to the well-established crossover from Slater insulator to Mott-Hubbard insulator and from itinerant AF to Heisenberg AF with increasing U in the Hubbard model ($g = 0$) [**166**, **183**, **184**]. We focused here on intermediate to strong coupling,, i.e. U exceeding half the bandwidth $W = 8t$ and $\omega_0 = t$. Further investigation of the effect of ω_0 on the cross-over is of interest.

In Chapter 7, we have generalized our existing understanding of the effect of interlayer/interorbital hybridization t_3 on *magnetic* order driven by an on-site *electron-electron repulsion* in the Hubbard model to *charge* order originating in *electron-phonon interactions* in the Holstein model. The two scenarios, although qualitatively related, are quite distinct in detail owing to the lower symmetry of the CDW order parameter relative to the magnetic case. Despite this difference, and its consequences such as the appearance of charge order at finite temperature, the basic feature of the destruction of long range order in the limit of large hybridization is shown still to occur. Indeed, one remarkable conclusion of our work is that t_3 seems to restore the degeneracy of pairing and charge correlations at the QCP.

Our most interesting observation is that the coexistence of CDW order on a layer with non-zero electron-phonon coupling λ with a metallic phase on the $\lambda = 0$ layer, which is trivially true at $t_3 = 0$, likely extends out to finite t_3. This conclusion is based on the inability to scale the charge correlations in the $\lambda = 0$ layer unless $t_3 \gtrsim 1.4$ (for $\lambda_{+1} = 0.2$).

The possibility that charge order takes place selectively parallels the known occurrence of distinct Mott transitions in multi-orbital Hubbard models and the coexistence of metallic and insulating behavior. The connection is, however, not exact, since in principle a Mott transition might occur in the absence of spontaneous symmetry breaking, whereas the insulating CDW phase here breaks Z_2 symmetry. With that said, the Mott transition in its most common incarnation, the square lattice Hubbard model, *is* always accompanied by long range antiferromagnetic order. Thus our work does provide a close analog of the case of orbital selective transitions in bands with differing electron-electron interaction strengths.

Finally, we emphasize that our results for electron-phonon interactions on different geometries differ from those for electron-electron interactions (attractive Hubbard) [**123**] in a fundamental way. The degeneracy of the superconducting and CDW orders at half-filling in the half-filled attractive Hubbard model implies the absence of long range order except in

the ground state (Mermin-Wagner). This symmetry is broken in the Holstein model. As a consequence there is a finite CDW T_c even on two dimensional geometries.

Indeed, we have provided, for the first time to our knowledge, a precise quantification of the Holstein to Hubbard mapping in the anti-adiabatic limit. The data of Fig. 2.1 emphasize that the spin symmetry characterizing the Hubbard model is violated by more than a factor of five for the Holstein model at $\omega_0/t = 1$, by almost a factor of two at $\omega_0/t = 10$, and even at $\omega_0/t = 10^2$ a difference of 5 percent remains.

Individually, the Hubbard, Holstein and SSH Hamiltonians exhibit a rich panoply of phenomena when doped away from half-filling. The interaction U leads to a complex mixture of pseudogap physics, strange metal behavior, stripe order and d-wave pairing when doped. The Holstein and SSH model host polarons in the dilute limit which can bind to bipolarons and condense into superconducting phases. New phases of matter are thus likely to emerge from the study of regimes of these electron-electron and electron-phonon interactions away from half-filling. Work in this direction has already begun as shown in [**185**]. This thesis lays the groundwork for the study of the cooperation and competition of different ordered phases arising from electron-phonon interactions and the role of special features of the non-interacting dispersion relation.

Bibliography

[1] Y.-X. Zhang, W.-T. Chiu, N. C. Costa, G. G. Batrouni, and R. T. Scalettar. Charge Order in the Holstein Model on a Honeycomb Lattice. *Phys. Rev. Lett.*, 122:077602, 2019.

[2] C. Chen, X. Y. Xu, Z. Y. Meng, and M. Hohenadler. Charge-density-wave transitions of dirac fermions coupled to phonons. *Phys. Rev. Lett.*, 122:077601, 2019.

[3] J. Hubbard. Electron Correlations in Narrow Energy Bands. *Proceedings of the Royal Society of London. Series A, Mathematical and Physical Sciences*, 276(1365):238–257, 1963.

[4] A. Georges, G. Kotliar, W. Krauth, and M.J Rozenberg. Dynamical mean-field theory of strongly correlated fermion systems and the limit of infinite dimensions. *Rev. Mod. Phys.*, 68:13, 1996.

[5] Patrick A. Lee, Naoto Nagaosa, and Xiao-Gang Wen. Doping a Mott insulator: Physics of high-temperature superconductivity. *Rev. Mod. Phys.*, 78:17–85, 2006.

[6] Philip M Dee, Jennifer Coulter, Kevin G Kleiner, and Steven Johnston. Relative importance of nonlinear electron-phonon coupling and vertex corrections in the Holstein model. *Communications Physics*, 3(1):1–7, 2020.

[7] B. Nosarzewski, E. W. Huang, Philip M. Dee, I. Esterlis, B. Moritz, S. A. Kivelson, S. Johnston, and T. P. Devereaux. Superconductivity, charge density waves, and bipolarons in the Holstein model. *Phys. Rev. B*, 103:235156, 2021.

[8] R. M. Noack, D. J. Scalapino, and R. T. Scalettar. CDW and Pairing Susceptibilities in a Two Dimensional Electron-Phonon Model. *Phys. Rev. Lett.*, 66:778–781, 1991.

[9] M. Vekić, R. M. Noack, and S. R. White. Charge-density waves versus superconductivity in the Holstein model with next-nearest-neighbor hopping. *Phys. Rev. B*, 46:271–278, 1992.

[10] Chunhan Feng, Huaiming Guo, and Richard T. Scalettar. Charge density waves on a half-filled decorated honeycomb lattice. *Phys. Rev. B*, 101:205103, 2020.

[11] B. Cohen-Stead, N. C. Costa, E. Khatami, and R. T. Scalettar. Effect of strain on charge density wave order in the Holstein model. *Phys. Rev. B*, 100:045125, 2019.

[12] Z.-X. Li, M. L. Cohen, and D.-H. Lee. Enhancement of superconductivity by frustrating the charge order. *Phys. Rev. B*, 100(24):245105, 2019.

[13] C. Feng and R. T. Scalettar. Interplay of flat electronic bands with Holstein phonons. *Phys. Rev. B*, 102(23):235152, 2020.

[14] B. Nosarzewski, E. W. Huang, Philip M. Dee, I. Esterlis, B. Moritz, S. A. Kivelson, S. Johnston, and T. P. Devereaux. Superconductivity, charge density waves, and bipolarons in the Holstein model. *Phys. Rev. B*, 103:235156, 2021.

[15] B. Xiao, N. C. Costa, E. Khatami, G. G. Batrouni, and R. T. Scalettar. Charge density wave and superconductivity in the disordered Holstein model. *Phys. Rev. B*, 103:L060501, 2021.

[16] Owen Bradley, George G. Batrouni, and Richard T. Scalettar. Superconductivity and charge density wave order in the two-dimensional Holstein model. *Phys. Rev. B*, 103:235104, 2021.

[17] H.G. Keiss. Conjugated Conducting Polymers. *Springer-Verlag Berlin*, 1992.

[18] T. Ishiguro and K. Yamaji. Organic Superconductors. *Springer-Verlag Berlin*, 1990.

[19] H. Toftlund and O. Simonsen. Preparation and Structure of a New Kind of an Extended Partially Oxidized Linear Chain Compound- Catena-(Mu-Bromo)Bis((1R,2R)-Cyclohexanediamine)Nickel(2.77) Bromide. *Inorg. Chem.*, 23:4261, 1984.

[20] Masashi Hase, Ichiro Terasaki, and Kunimitsu Uchinokura. Observation of the spin-Peierls transition in linear Cu^{2+} (spin-1/2) chains in an inorganic compound $CuGeO_3$. *Phys. Rev. Lett.*, 70:3651–3654, 1993.

[21] Chunhan Feng, Bo Xing, Dario Poletti, Richard Scalettar, and George Batrouni. Phase Diagram of the Su-Schrieffer-Heeger-Hubbard model on a square lattice, 2021. arXiv:2109.09206.

[22] Yuxi Zhang, Chunhan Feng, Rubem Mondaini, George G. Batrouni, and Richard T. Scalettar. Charge Singlets and Orbital Selective Charge Density Wave Transitions, 2021. arXiv:2109.13482.

[23] F. D. M. Haldane. Model for a Quantum Hall Effect without Landau Levels: Condensed-Matter Realization of the "Parity Anomaly". *Phys. Rev. Lett.*, 61:2015–2018, 1988.

[24] C. L. Kane and E. J. Mele. Quantum Spin Hall Effect in Graphene. *Phys. Rev. Lett.*, 95:226801, 2005.

[25] K. S. Novoselov, A. K. Geim, S. V. Morozov, D. Jiang, M. I. Katsnelson, I. V. Grigorieva, S. V. Dubonos, and A. A. Firsov. Two-dimensional gas of massless Dirac fermions in graphene. *Nature*, 438(7065):197–200, 2005.

[26] Guohong Li and Eva Y. Andrei. Observation of Landau levels of Dirac fermions in graphite. *Nature Physics*, 3(9):623–627, 2007.

[27] B Wunsch, F Guinea, and F Sols. Dirac-point engineering and topological phase transitions in honeycomb optical lattices. *New Journal of Physics*, 10(10):103027, 2008.

[28] T.O. Wehling, A.M. Black-Schaffer, and A.V. Balatsky. Dirac materials. *Advances in Physics*, 63(1):1–76, 2014.

[29] Thereza Paiva, R. T. Scalettar, W. Zheng, R. R. P. Singh, and J. Oitmaa. Ground-state and finite-temperature signatures of quantum phase transitions in the half-filled Hubbard model on a honeycomb lattice. *Phys. Rev. B*, 72:085123, 2005.

[30] Sandro Sorella, Yuichi Otsuka, and Seiji Yunoki. Absence of a Spin Liquid Phase in the Hubbard Model on the Honeycomb Lattice. *Scientific Reports*, 2(1):992, 2012.

[31] O. Derzhko, J. Richter, and M. Maksymenko. Strongly correlated flat-band systems: The route from Heisenberg spins to Hubbard electrons. *Int. J. of Mod. Phys. B*, 29:1530007, 2015.

[32] Daniel Leykam and Alexei Andreanov and Sergej Flach. Artificial flat band systems: from lattice models to experiments. *Advances in Physics: X*, 3(1):1473052, 2018.

[33] Elliott H. Lieb. Two theorems on the Hubbard model. *Phys. Rev. Lett.*, 62:1201–1204, 1989.

[34] A Mielke. Ferromagnetic ground states for the Hubbard model on line graphs. *J. Phys. A: Math. Gen.*, 24(2):L73, 1991.

[35] A Mielke. Ferromagnetism in the Hubbard model on line graphs and further considerations. *Journal of Physics A: Mathematical and General*, 24(14):3311, 1991.

[36] Hal Tasaki. Ferromagnetism in the Hubbard models with degenerate single-electron ground states. *Phys. Rev. Lett.*, 69:1608–1611, 1992.

[37] Hal Tasaki. From Nagaoka's Ferromagnetism to Flat-Band Ferromagnetism and Beyond. *Prog. Theor. Phys.*, 99:489–548, 1998.

[38] S. Li and S. Johnston. Quantum Monte Carlo study of lattice polarons in the two-dimensional three-orbital Su–Schrieffer–Heeger model. *NPJ Quantum Mater.*, 5:40, 2020.

[39] R. T. Scalettar, N. E. Bickers, and D. J. Scalapino. Competition of Pairing and Peierls–CDW Correlations in a 2-D Electron-Phonon Model. *Phys. Rev. B*, 40:197–200, 1989.

[40] W Koller, D Meyer, Y Ōno, and AC Hewson. First-and second-order phase transitions in the Holstein-Hubbard model. *EPL (Europhysics Letters)*, 66(4):559, 2004.

[41] Philipp Werner and Andrew J Millis. Efficient dynamical mean field simulation of the Holstein-Hubbard model. *Phys. Rev. Lett.*, 99(14):146404, 2007.

[42] H. Fehske, G. Hager, and E. Jeckelmann. Metallicity in the half-filled Holstein-Hubbard model. *EPL (Europhysics Letters)*, 84(5):57001, 2008.

[43] S. Johnston, E. A. Nowadnick, Y. F. Kung, B. Moritz, R. T. Scalettar, and T. P. Devereaux. Determinant quantum Monte Carlo study of the two-dimensional single-band Hubbard-Holstein model. *Phys. Rev. B*, 87:235133, 2013.

[44] Yao Wang, Ilya Esterlis, Tao Shi, J. Ignacio Cirac, and Eugene Demler. Zero-temperature phases of the two-dimensional Hubbard-Holstein model: A non-Gaussian exact diagonalization study. *Phys. Rev. Research*, 2:043258, 2020.

[45] Natanael C. Costa, Kazuhiro Seki, Seiji Yunoki, and Sandro Sorella. Phase diagram of the two-dimensional Hubbard-Holstein model. *Communications Physics*, 3(1):1–6, 2020.

[46] Zhaoyu Han, Steven A Kivelson, and Hong Yao. Strong coupling limit of the Holstein-Hubbard model. *Phys. Rev. Lett.*, 125(16):167001, 2020.

[47] Bo Xing, Wei-Ting Chiu, Dario Poletti, R. T. Scalettar, and George Batrouni. Quantum Monte Carlo Simulations of the 2D Su-Schrieffer-Heeger Model. *Phys. Rev. Lett.*, 126:017601, 2021.

[48] Xun Cai, Zi-Xiang Li, and Hong Yao. Antiferromagnetism induced by electron-phonon-coupling, 2021.

[49] Anika Goetz, Stefan Beyl, Martin Hohenadler, and Fakher F. Assaad. Langevin dynamics simulations of the two-dimensional Su-Schrieffer-Heeger model, 2021.

[50] J. Georg Bednorz and K. Alex Müller. Perovskite-type oxides—the new approach to high-T_c superconductivity. *Rev. Mod. Phys.*, 60(3):585, 1988.

[51] MA Kastner, RJ Birgeneau, G Shirane, and Y Endoh. Magnetic, transport, and optical properties of monolayer copper oxides. *Rev. Mod. Phys.*, 70(3):897, 1998.

[52] T. Timusk and B. Statt. The pseudogap in high-temperature superconductors: an experimental survey. *Rep. Prog. Phys.*, 62(1):61, 1999.

[53] P. A. Lee, N. Nagaosa, and X.-G. Wen. Doping a Mott insulator: Physics of high-temperature superconductivity. *Rev. Mod. Phys.*, 78:17, 2006.

[54] Matthias Vojta. Lattice symmetry breaking in cuprate superconductors: stripes, nematics, and superconductivity. *Advances in Physics*, 58(6):699–820, 2009.

[55] J. M. B. Lopes dos Santos, N. M. R. Peres, and A. H. Castro Neto. Graphene bilayer with a twist: Electronic structure. *Phys. Rev. Lett.*, 99:256802, 2007.

[56] R. Bistritzer and A. H. MacDonald. Transport between twisted graphene layers. *Phys. Rev. B*, 81(24):245412, 2010.

[57] G. Trambly de Laissardiére, D. Mayou, and L. Magaud. Localization of Dirac electrons in rotated graphene bilayers. *Nano Lett.*, 10(3):804–808, 2010.

[58] J. Xue, J. Sanchez-Yamagishi, D. Bulmash, P. Jacquod, A. Deshpande, K. Watanabe, T. Taniguchi, P. Jarillo-Herrero, and B. J. LeRoy. Scanning tunnelling microscopy and spectroscopy of ultra-flat graphene on hexagonal boron nitride. *Nat. Mater.*, 10(4):282, 2011.

[59] T. C. Lang, Z. Y. Meng, M. M. Scherer, S. Uebelacker, F. F. Assaad, A. Muramatsu, C. Honerkamp, and S. Wessel. Antiferromagnetism in the Hubbard Model on the Bernal-Stacked Honeycomb Bilayer. *Phys. Rev. Lett.*, 109:126402, 2012.

[60] E. McCann and M. Koshino. The electronic properties of bilayer graphene. *Rep. Prog. Phys*, 76(5):056503, 2013.

[61] A Liebsch. Single Mott transition in the multiorbital Hubbard model. *Phys. Rev. B*, 70(16):165103, 2004.

[62] C. Knecht, N. Blümer, and P.G.J. Van Dongen. Orbital-selective Mott transitions in the anisotropic two-band Hubbard model at finite temperatures. *Phys. Rev. B*, 72(8):081103, 2005.

[63] K. Bouadim, G. G. Batrouni, and R. T. Scalettar. Determinant quantum Monte Carlo study of the orbitally selective Mott transition. *Phys. Rev. Lett.*, 102(22):226402, 2009.

[64] A. Koga, N. Kawakami, T. M. Rice, and M. Sigrist. Orbital-selective Mott transitions in the degenerate Hubbard model. *Phys. Rev. Lett.*, 92:216402, 2004.

[65] L. De Leo, M. Civelli, and G. Kotliar. $T = 0$ heavy-fermion quantum critical point as an orbital-selective Mott transition. *Phys. Rev. Lett.*, 101(25):256404, 2008.

[66] Luca de' Medici, S. R. Hassan, Massimo Capone, and Xi Dai. Orbital-selective Mott transition out of band degeneracy lifting. *Phys. Rev. Lett.*, 102:126401, 2009.

[67] Z.-Y. Song, H. Lee, and Y.-Z. Zhang. Possible origin of orbital selective Mott transitions in iron-based superconductors and $Ca_{2-x}Sr_xRuO_4$. *New J. Phys.*, 17(3):033034, 2015.

[68] Z.-Y. Song, X.-C. Jiang, H.-Q. Lin, and Y.-Z. Zhang. Distinct nature of orbital-selective Mott phases dominated by low-energy local spin fluctuations. *Phys. Rev. B*, 96(23):235119, 2017.

[69] J Herbrych, J Heverhagen, ND Patel, Gonzalo Alvarez, Maria Daghofer, Adriana Moreo, and E Dagotto. Novel magnetic block states in low-dimensional iron-based superconductors. *Phys. Rev. Lett.*, 123(2):027203, 2019.

[70] Jacek Herbrych, Gonzalo Alvarez, Adriana Moreo, and E Dagotto. Block orbital-selective Mott insulators: a spin excitation analysis. *Phys. Rev. B*, 102(11):115134, 2020.

[71] Bradraj Pandey, Ling-Fang Lin, Rahul Soni, Nitin Kaushal, Jacek Herbrych, Gonzalo Alvarez, and Elbio Dagotto. Prediction of exotic magnetic states in the alkali-metal quasi-one-dimensional iron selenide compound Na_2FeSe_2. *Phys. Rev. B*, 102(3):035149, 2020.

[72] Maksymilian Środa, Elbio Dagotto, and Jacek Herbrych. Quantum magnetism of iron-based ladders: Blocks, spirals, and spin flux. *Phys. Rev. B*, 104(4):045128, 2021.

[73] Martin C. Gutzwiller. Effect of correlation on the ferromagnetism of transition metals. *Phys. Rev. Lett.*, 10:159–162, 1963.

[74] Junjiro Kanamori. Electron Correlation and Ferromagnetism of Transition Metals. *Progress of Theoretical Physics*, 30(3):275–289, 1963.

[75] T Holstein. Studies of polaron motion: Part I. The molecular-crystal model. *Annals of Physics*, 8(3):325, 1959.

[76] W. P. Su, J. R. Schrieffer, and A. J. Heeger. Solitons in Polyacetylene. *Phys. Rev. Lett.*, 42:1698–1701, 1979.

[77] M. Weber and M. Hohenadler. Two-dimensional Holstein-Hubbard model: Critical temperature, Ising universality, and bipolaron liquid. *Phys. Rev. B*, 98(8):085405, 2018.

[78] I. G. Lang and Yu. A. Firsov. Kinetic theory of semiconductors with low mobility. *Sov. Phys. JETP*, 16:1301, 1963.

[79] J. E. Hirsch and S. Tang. Antiferromagnetism in the Two-Dimensional Hubbard Model. *Phys. Rev. Lett.*, 62:591–594, 1989.

[80] Long-Hua Wu and Xiao Hu. Topological Properties of Electrons in Honeycomb Lattice with Detuned Hopping Energy. *Scientific Reports*, 6(1):24347, 2016.

[81] Matthias Troyer, Hiroshi Kontani, and Kazuo Ueda. Phase Diagram of Depleted Heisenberg Model for CaV_4O_9. *Phys. Rev. Lett.*, 76:3822–3825, 1996.

[82] Ehsan Khatami, Rajiv R. P. Singh, Warren E. Pickett, and Richard T. Scalettar. Magnetic Correlations and Pairing in the 1/5-Depleted Square Lattice Hubbard Model. *Phys. Rev. Lett.*, 113:106402, 2014.

[83] Satoshi Taniguchi, Takashi Nishikawa, Yukio Yasui, Yoshiaki Kobayashi, Masatoshi Sato, Takashi Nishioka, Masaaki Kontani, and Kazuhiro Sano. Spin Gap Behavior of S=1/2 Quasi-Two-Dimensional System CaV_4O_9. *Journal of the Physical Society of Japan*, 64(8):2758–2761, 1995.

[84] Nobuyuki Katoh and Masatoshi Imada. Spin Gap in Two-Dimensional Heisenberg Model for CaV_4O_9. *Journal of the Physical Society of Japan*, 64(11):4105–4108, 1995.

[85] Kazuo Ueda, Hiroshi Kontani, Manfred Sigrist, and Patrick A. Lee. Plaquette Resonating-Valence-Bond Ground State of CaV_4O_9. *Phys. Rev. Lett.*, 76:1932–1935, 1996.

[86] M. P. Gelfand, Zheng Weihong, Rajiv R. P. Singh, J. Oitmaa, and C. J. Hamer. Convergent Expansions for Properties of the Heisenberg Model for CaV_4O_9. *Phys. Rev. Lett.*, 77:2794–2797, 1996.

[87] W. E. Pickett. Impact of Structure on Magnetic Coupling in CaV_4O_9. *Phys. Rev. Lett.*, 79:1746–1749, 1997.

[88] A. Liebsch. Novel Mott Transitions in a Nonisotropic Two-Band Hubbard Model. *Phys. Rev. Lett.*, 95:116402, 2005.

[89] R. Arita and K. Held. Orbital-selective Mott-Hubbard transition in the two-band Hubbard model. *Phys. Rev. B*, 72:201102, 2005.

[90] Kensuke Inaba and Akihisa Koga. Phase diagrams of the two-orbital Hubbard model with different bandwidths. *Phys. Rev. B*, 73:155106, 2006.

[91] Akihisa Koga, Norio Kawakami, T. M. Rice, and Manfred Sigrist. Orbital-Selective Mott Transitions in the Degenerate Hubbard Model. *Phys. Rev. Lett.*, 92:216402, 2004.

[92] Michel Ferrero, Federico Becca, Michele Fabrizio, and Massimo Capone. Dynamical behavior across the Mott transition of two bands with different bandwidths. *Phys. Rev. B*, 72:205126, 2005.

[93] L. de'Medici, A. Georges, and S. Biermann. Orbital-selective Mott transition in multiband systems: Slave-spin representation and dynamical mean-field theory. *Phys. Rev. B*, 72:205124, 2005.

[94] S. Biermann, L. de' Medici, and A. Georges. Non-Fermi-Liquid Behavior and Double-Exchange Physics in Orbital-Selective Mott Systems. *Phys. Rev. Lett.*, 95:206401, 2005.

[95] P. A. Lee, T. M. Rice, J. W. Serene, L. J. Sham, and J. W. Wilkins. Theories of heavy-electron systems. *Comments on Condensed Matter Physics*, 12(3):99–161, 1986.

[96] T. Nishino and Kazuo Ueda. Spin- and charge-excitation gaps in the one-dimensional periodic Anderson model. *Phys. Rev. B*, 47:12451–12458, 1993.

[97] R. M. Fye. Quantum Monte Carlo study of the one-dimensional symmetric Anderson lattice. *Phys. Rev. B*, 41:2490–2509, 1990.

[98] M. Jarrell, Hossein Akhlaghpour, and Th. Pruschke. Periodic Anderson model in infinite dimensions. *Phys. Rev. Lett.*, 70:1670–1673, 1993.

[99] M. Vekić, J. W. Cannon, D. J. Scalapino, R. T. Scalettar, and R. L. Sugar. Competition between Antiferromagnetic Order and Spin-Liquid Behavior in the Two-Dimensional Periodic Anderson Model at Half Filling. *Phys. Rev. Lett.*, 74:2367–2370, 1995.

[100] Carey Huscroft, A.K. McMahan, and R.T. Scalettar. Magnetic and Thermodynamic Properties of the Three-Dimensional Periodic Anderson Hamiltonian. *Phys. Rev. Lett.*, 82:2342, 1999.

[101] R. Blankenbecler, D. J. Scalapino, and R. L. Sugar. Monte Carlo calculations of coupled boson-fermion systems. I. *Phys. Rev. D*, 24:2278–2286, 1981.

[102] S. R. White, D. J. Scalapino, R. L. Sugar, E. Y. Loh, J. E. Gubernatis, and R. T. Scalettar. Numerical study of the two-dimensional Hubbard model. *Phys. Rev. B*, 40:506–516, 1989.

[103] H.F. Trotter. On the product of semi-groups of operators. *Proc. Am. Math. Soc.*, 10:545, 1959.

[104] M. Suzuki. Generalized Trotter's formula and systematic approximants of exponential operators and inner derivations with applications to many-body problems. *Commun. Math. Phys.*, 51:183, 1976.

[105] R.M. Fye. New results on Trotter-like approximations. *Phys. Rev. B*, 33:6271, 1986.

[106] R.M. Fye and R.T. Scalettar. Calculating specific heats and susceptibilities using the Trotter approximation. *Phys. Rev. B*, 36:3833, 1987.

[107] Andreas Rüegg, Jun Wen, and Gregory A. Fiete. Topological insulators on the decorated honeycomb lattice. *Phys. Rev. B*, 81:205115, 2010.

[108] V. Hermann, S. Biswas, J. Ebad-Allah, F. Freund, A. Jesche, A. A. Tsirlin, M. Hanfland, D. Khomskii, P. Gegenwart, R. Valentí, and C. A. Kuntscher. Pressure-induced formation of rhodium zigzag chains in the honeycomb rhodate Li_2RhO_3. *Phys. Rev. B*, 100:064105, 2019.

[109] Anand Sharma, Valeri N. Kotov, and Antonio H. Castro Neto. Interacting Anisotropic Dirac Fermions in Strained Graphene and Related Systems.

[110] Sandro Sorella, Kazuhiro Seki, Oleg O. Brovko, Tomonori Shirakawa, Shohei Miyakoshi, Seiji Yunoki, and Erio Tosatti. Correlation-Driven Dimerization and Topological Gap Opening in Isotropically Strained Graphene. *Phys. Rev. Lett.*, 121:066402, 2018.

[111] O. V. Gamayun, V. P. Ostroukh, N. V. Gnezdilov, İ. Adagideli, and C. W. J. Beenakker. Valley-momentum locking in a graphene superlattice with Y-shaped Kekulé bond texture. *New Journal of Physics*, 20(2):023016, 2018.

[112] Elias Andrade, Ramon Carrillo-Bastos, and Gerardo G. Naumis. Valley engineering by strain in Kekulé-distorted graphene. *Phys. Rev. B*, 99:035411, 2019.

[113] J. E. Hirsch. Two-dimensional Hubbard model: Numerical simulation study. *Phys. Rev. B*, 31:4403–4419, 1985.

[114] J.E. Gubernatis, Mark Jarrell, R.N. Silver, and D. S. Sivia. Quantum Monte Carlo simulations and maximum entropy: Dynamics from imaginary-time data. *Phys. Rev. B*, 44:6011, 1991.

[115] A. Euverte, S. Chiesa, R. T. Scalettar, and G. G. Batrouni. Magnetic transition in a correlated band insulator. *Phys. Rev. B*, 87:125141, 2013.

[116] Bill Sutherland. Localization of electronic wave functions due to local topology. *Phys. Rev. B*, 34:5208–5211, 1986.

[117] Aleksi Julku, Sebastiano Peotta, Tuomas I. Vanhala, Dong-Hee Kim, and Päivi Törmä. Geometric Origin of Superfluidity in the Lieb-Lattice Flat Band. *Phys. Rev. Lett.*, 117:045303, 2016.

[118] Pramod Kumar, Tuomas I. Vanhala, and Päivi Törmä. Magnetization, d-wave superconductivity, and non-Fermi-liquid behavior in a crossover from dispersive to flat bands. *Phys. Rev. B*, 100:125141, 2019.

[119] Kukka-Emilia Huhtinen and Päivi Törmä. Insulator-pseudogap crossover in the Lieb lattice. *arXiv:2007.05118*.

[120] Nyayabanta Swain and Madhuparna Karmakar. Strain-induced superconductor-insulator transition on a Lieb lattice. *Phys. Rev. Research*, 2:023136, 2020.

[121] S. D. Huber and E. Altman. Bose condensation in flat bands. *Phys. Rev. B*, 82:184502, 2010.

[122] M. Tovmasyan, E. Van Nieuwenburg, and S. D. Huber. Geometry induced pair condensation. *Phys. Rev. B*, 88:220510R, 2013.

[123] V. I. Iglovikov, F. Hébert, B. Grémaud, G. G. Batrouni, and R. T. Scalettar. Superconducting transitions in flat-band systems. *Phys. Rev. B*, 90:094506, 2014.

[124] S.A. Parameswaran, R. Roy, and S. Sondhi. Fractional quantum Hall physics in topological flat bands. *Comptes Rendus Physique*, 14:816, 2013.

[125] E. Bergholtz and Z. Liu. Topological Flat Band Models and Fractional Chern Insulators. *Int. J. of Mod. Phys. B*, 27:1330017, 2013.

[126] S. Takayoshi, H. Katsura, N. Watanabe, and H. Aoki. Phase diagram and pair Tomonaga-Luttinger liquid in a Bose-Hubbard model with flat bands. *Phys. Rev. A*, 88:063613, 2013.

[127] Benoît Grémaud and G. George Batrouni. Haldane phase on the sawtooth lattice: Edge states, entanglement spectrum, and the flat band. *Phys. Rev. B*, 95:165131, 2017.

[128] Y. Cao, V. Fatemi, A. Demir, S. Fang, S. Tomarken, J. Luo, J. Sanchez-Yamagishi, K. Watanabe, T. Taniguchi, E. Kaxiras, R. Ashoori, and P. Jarillo-Herrero. Correlated insulator behaviour at half-filling in magic-angle graphene superlattices. *Nature*, 556:80, 2018.

[129] Y. Cao, V. Fatemi, S. Fang, K. Watanabe, T. Taniguchi, E. Kaxiras, and P. Jarillo-Herrero. Un-conventional superconductivity in magic-angle graphene super-lattices. *Nature*, 556:43, 2018.

[130] H. Guo, X. Zhu, S. Feng, and R. Scalettar. Pairing symmetry of interacting fermions on twisted bilayer graphene superlattice. *Phys. Rev. B*, 97:235453, 2018.

[131] A. Pinto, N. Frazao, D. Azevedo, and F. Moraes. Evidence for flat zero-energy bands in bilayer graphene with a periodic defect lattice. *Physica E*, 119:113987, 2020.

[132] J. M. Lee, C. Geng, J.W. Park, M. Oshikawa, S. Lee, H. Yeom, and G. Cho. Stable Flatbands, Topology, and Superconductivity of Magic Honeycomb Networks. *Phys. Rev. Lett.*, 124:137002, 2020.

[133] C. Shen, Y. Chu, Q-S. Wu, N. Li, S. Wang, Y. Zhao, J. Tang, J. Liu, J. Tian, K. Watanabe, T. Taniguchi, R. Yang, Z. Meng, D. Shi, O. Yazyev, and G. Zhan. Correlated states in twisted double bilayer graphene. *Nature Physics*, 16:520, 2020.

[134] D Guzmán-Silva, C Mejía-Cortés, M A Bandres, M C Rechtsman, S Weimann, S Nolte, M Segev, A Szameit, and R A Vicencio. Experimental observation of bulk and edge transport in photonic Lieb lattices. *New Journal of Physics*, 16(6):063061, 2014.

[135] Sebabrata Mukherjee, Alexander Spracklen, Debaditya Choudhury, Nathan Goldman, Patrik Öhberg, Erika Andersson, and Robert R. Thomson. Observation of a Localized Flat-Band State in a Photonic Lieb Lattice. *Phys. Rev. Lett.*, 114:245504, 2015.

[136] Kazuto Noda, Kensuke Inaba, and Makoto Yamashita. Flat-band ferromagnetism in the multilayer Lieb optical lattice. *Phys. Rev. A*, 90:043624, 2014.

[137] Shiqiang Xia, Yi Hu, Daohong Song, Yuanyuan Zong, Liqin Tang, and Zhigang Chen. Demonstration of flat-band image transmission in optically induced Lieb photonic lattices. *Opt. Lett.*, 41(7):1435–1438, 2016.

[138] L. Santos, J.I. Cirac M.A. Baranov, H.-U. Everts, H. Fehrmann, and M. Lewenstein. Atomic Quantum Gases in Kagome Lattices. *Phys. Rev. Lett.*, 93:030601, 2004.

[139] C. Wu, D. Bergman, L. Balents, and S. Das Sarma. Flat Bands and Wigner Crystallization in the Honeycomb Optical Lattice. *Phys. Rev. Lett.*, 99:070401, 2007.

[140] J. K. Freericks, M. Jarrell, and D. J. Scalapino. Holstein model in infinite dimensions. *Phys. Rev. B*, 48:6302–6314, 1993.

[141] A.H. Romero, D.W. Brown, and K. Lindenberg. Effects of dimensionality and anisotropy on the Holstein polaron. *Phys. Rev. B*, 60:14080, 1999.

[142] L.C. Ku, S.A. Trugman, and J. Bonca. Dimensionality effects on the Holstein polaron. *Phys. Rev. B*, 65:174306, 2002.

[143] M. Hohenadler, H. G. Evertz, and W. von der Linden. Quantum Monte Carlo and variational approaches to the Holstein model. *Phys. Rev. B*, 69:024301, 2004.

[144] Dominic J. J. Marchand and Mona Berciu. Effect of dispersive optical phonons on the behavior of a Holstein polaron. *Phys. Rev. B*, 88:060301, 2013.

[145] R. T. Scalettar, N. E. Bickers, and D. J. Scalapino. Competition of pairing and Peierls–charge-density-wave correlations in a two-dimensional electron-phonon model. *Phys. Rev. B*, 40:197–200, 1989.

[146] F. Marsiglio. Eliashberg theory of the critical temperature and isotope effect. Dependence on bandwidth, band-filling, and direct Coulomb repulsion. *J. Low. Temp. Phys.*, 87:659, 1992.

[147] W. von der Linden, E. Berger, and P. Valásek. The Hubbard-Holstein model. *J. Low Temp. Phys.*, 99:517, 1995.

[148] A. S. Alexandrov. Breakdown of the Migdal-Eliashberg theory in the strong-coupling adiabatic regime. *Europhys. Lett.*, 56(1):92–98, 2001.

[149] Andrey V. Chubukov, Artem Abanov, Ilya Esterlis, and Steven A. Kivelson. Eliashberg theory of phonon-mediated superconductivity – when it is valid and how it breaks down. *arXiv:2004.01281*.

[150] M. Vekic, R. M. Noack, and S. R. White. Charge-density waves versus superconductivity in the Holstein model with next-nearest-neighbor hopping. *Phys. Rev. B*, 46:271–278, 1992.

[151] M. Vekić and S. R. White. Gap formation in the density of states for the Holstein model. *Phys. Rev. B*, 48:7643–7650, 1993.

[152] N. C. Costa, T. Blommel, W.-T. Chiu, G. G. Batrouni, and R. T. Scalettar. Phonon dispersion and the competition between pairing and charge order. *Phys. Rev. Lett.*, 120:187003, 2018.

[153] B. Xiao, N. C. Costa, E. Khatami, G. G. Batrouni, and R. T. Scalettar. Charge density wave and superconductivity in the disordered Holstein model. *arXiv:1910.08703*.

[154] Chuang Chen, Xiao Yan Xu, Junwei Liu, George Batrouni, Richard T. Scalettar, and Zi Yang Meng. Symmetry enforced self-learning monte carlo method applied to the Holstein model. *Phys. Rev. B*, 2018.

[155] Stefan Beyl, Florian Goth, and Fakher F. Assaad. Revisiting the hybrid quantum Monte Carlo method for Hubbard and electron-phonon models. *Phys. Rev. B*, 97:085144, 2018.

[156] G. G. Batrouni and Richard T. Scalettar. Langevin Simulations of a Long Range Electron Phonon Model. *Phys. Rev. B*, 99:035114, 2019.

[157] G. G. Batrouni and Richard T. Scalettar. Quantum Monte Carlo with the Langevin Equation: Coupled Bose-Fermi Systems. *Journal of Physics: Conference Series*, 1290:012004, 2019.

[158] S. Sorella, S. Baroni, R. Car, and M. Parinello. A novel technique for the simulation of interacting fermion systems. *Europhys. Lett.*, 8:663, 1989.

[159] Natanael C. Costa, Tiago Mendes-Santos, Thereza Paiva, Raimundo R. dos Santos, and Richard T. Scalettar. Ferromagnetism beyond Lieb's theorem. *Phys. Rev. B*, 94:155107, 2016.

[160] W. S. Oliveira, N. C. Costa, J. Pimentel de Lima, and Raimundo R. dos Santos. Classical and quantum percolation on the Lieb lattice. unpublished, 2019.

[161] Martin Bercx, Johannes S. Hofmann, Fakher F. Assaad, and Thomas C. Lang. Spontaneous particle-hole symmetry breaking of correlated fermions on the Lieb lattice. *Phys. Rev. B*, 95:035108, 2017.

[162] John Sous, Monodeep Chakraborty, Roman V. Krems, and Mona Berciu. Light Bipolarons Stabilized by Peierls Electron-Phonon Coupling. *Phys. Rev. Lett.*, 121:247001, 2018.

[163] R. L. Stratonovich. On a Method of Calculating Quantum Distribution Functions. *Soviet Physics Doklady*, 2:416, 1957.

[164] J. Hubbard. Calculation of Partition Functions. *Phys. Rev. Lett.*, 3:77–78, 1959.

[165] JE Hirsch and S Tang. Antiferromagnetism in the two-dimensional Hubbard model. *Phys. Rev. Lett.*, 62(5):591, 1989.

[166] S. R. White, D. J. Scalapino, R. L. Sugar, E. Y. Loh, J. E. Gubernatis, and R. T. Scalettar. Numerical study of the two-dimensional Hubbard model. *Phys. Rev. B*, 40:506–516, 1989.

[167] SR White, DJ Scalapino, RL Sugar, NE Bickers, and RT Scalettar. Attractive and repulsive pairing interaction vertices for the two-dimensional Hubbard model. *Phys. Rev. B*, 39(1):839, 1989.

[168] A. W. Sandvik and D. J. Scalapino. Order-disorder transition in a two-layer quantum antiferromagnet. *Phys. Rev. Lett.*, 72:2777, 1994.

[169] R. T. Scalettar, J. W. Cannon, D. J. Scalapino, and R. L. Sugar. Magnetic and pairing correlations in coupled Hubbard planes. *Phys. Rev. B*, 50:13419, 1994.

[170] M. Vekic, J.W. Cannon, D.J. Scalapino, R.T. Scalettar, and R.L. Sugar. Competition between antiferromagnetic order and spin liquid behavior in the two-dimensional periodic Anderson model at half-filling. *Phys. Rev. Lett.*, 74(12):2367, 1995.

[171] L. Wang, K. S. D. Beach, and A. W. Sandvik. High-precision finite-size scaling analysis of the quantum-critical point of $S = 1/2$ Heisenberg antiferromagnetic bilayers. *Phys. Rev. B*, 73:014431, 2006.

[172] Michael Golor, Timo Reckling, Laura Classen, Michael M. Scherer, and Stefan Wessel. Ground-state phase diagram of the half-filled bilayer Hubbard model. *Phys. Rev. B*, 90:195131, 2014.

[173] S. Doniach. The Kondo lattice and weak antiferromagnetism. *Physica B+C*, 91:231, 1977.

[174] D.W. Hess, P.S. Riseborough, and J.L. Smith. In G.L. Trigg, editor, *Encyclopedia of Applied Physics*, volume 7, page 435. VCH, New York, 1993.

[175] N. Grewe and F. Steglich. In Jr. K. A. Gschneidner and L. L. Eyring, editors, *Handbook of Physics and Chemistry of Rare Earths*, volume 14, page 343. Elsevier, Amsterdam, 1991.

[176] F. Marsiglio. Pairing and charge-density-wave correlations in the Holstein model at half-filling. *Phys. Rev. B*, 42:2416, 1990.

[177] M. Hohenadler and G.G. Batrouni. Dominant charge density wave correlations in the Holstein model on the half-filled square lattice. *Phys. Rev. B*, 100(16):165114, 2019.

[178] Y.-X. Zhang, H.-M. Guo, and R. T. Scalettar. Charge density wave order on a π-flux square lattice. *Phys. Rev. B*, 101(20):205139, 2020.

[179] Studies of attractive Hubbard models, the anti-adiabatic limit of the Holstein model considered here, within the Dynamical Cluster Approximation are in progress. Philip Dee, Steven Johnston and Thomas Maier, private communication, work in progress.

[180] G. G. Batrouni and Richard T. Scalettar. Langevin simulations of a long-range electron-phonon model. *Phys. Rev. B*, 99:035114, 2019.

[181] A Götz, S Beyl, M Hohenadler, and FF Assaad. Valence-bond solid to antiferromagnet transition in the two-dimensional Su-Schrieffer-Heeger model by Langevin dynamics. *Physical Review B*, 105(8):085151, 2022.

[182] See Supplementary Material.

[183] Th Pruschke and Robert Zitzler. From Slater to Mott–Heisenberg physics: the antiferromagnetic phase of the Hubbard model. *Journal of Physics: Condensed Matter*, 15(46):7867, 2003.

[184] Marcin Raczkowski, Fakher F Assaad, and Masatoshi Imada. Local moments versus itinerant antiferromagnetism: Magnetic phase diagram and spectral properties of the anisotropic square lattice Hubbard model. *Phys. Rev. B*, 103(12):125137, 2021.

[185] Chao Zhang, Nikolay V. Prokof'ev, and Boris V. Svistunov. Bond Bipolarons: Sign-free Monte Carlo Approach, 2021.